ETH Institute for Particle Physics

ETHZ-IPP Internal Report 2009-03
February 2009

Diploma Thesis

Threshold Calibration of the CMS Pixel Detector

Michael Stückelberger

stumicha@student.ethz.ch
michael.stuckelberger@gmx.ch

under the supervision of

Prof. Dr. Urs Langenegger, ETH Zürich

PSI Villigen and CERN Geneva

Abstract

We have determined absolute (θ_{abs}) and in-time thresholds (θ_{int}) of the CMS pixel detector from two-dimensional scans of the number of readouts as a function of the DAC parameters `CalDel` and `Vcal`. These measurements have been taken for different values of `Vcthr` and I_{ana} at temperatures 17 °C and −10 °C, which provided the data for a parameterization of $\Delta\theta \doteq \theta_{int} - \theta_{abs}$ as a function of the comparator threshold θ and I_{ana}.

As the measured threshold dependency of $\Delta\theta$ did not match the previous expectations, a toy simulation that introduces comparator effects has been done. While it can explain the measured behavior, it will have to be investigated further, if it is indeed the comparator that causes the measured effects.

Contents

List of Figures

List of Tables

1 LHC and CMS

After a short general introduction to the Large Hadron Collider (LHC) and its experiments in section 1.1, the detector of the Compact Muon Solenoid (CMS) experiment is described in more detail in section 1.2.

1.1 Large Hadron Collider

The LHC is the world wide largest particle accelerator placed at CERN[1] at the border between France and Switzerland near Geneva in the tunnel of the previous LEP[2] collider. It is shown with the main preaccelerators and experiments in figure 1.1.

The protons (extracted from hydrogen atoms) get first accelerated in the linear accelerator LINAC 2 and in the synchrotrons PS[3] Booster, PS and SPS[4]. Only then they reach in bunches the LHC, a synchrotron, which consists of two concentric rings of 26.659 km circumstance up to 100 m underground. In opposite direction to each other, the protons are accelerated there from 450 GeV up to 7 TeV within 20 minutes and deflected by superconducting magnets [1]. This leads to the peak center of mass energy of 14 TeV.

The design luminosity is $10^{34}\,\mathrm{cm}^{-2}\mathrm{s}^{-1}$ or $10\,\mathrm{nb}^{-1}\mathrm{s}^{-1}$, which results in up to 20 expected interactions or 1 000 charged particles per bunch crossing (BC). At this luminosity 2 808 bunches of maximum $1.15 \cdot 10^{11}$ protons each will circulate in each beam tube. The collision frequency will be 40 MHz with a BC every 25 ns. The LHC will run at lower center of mass energy and luminosity in the beginning.

It is possible to run the LHC with heavy ions (mainly lead) instead of protons. In this case the design center of mass energy is 5.5 TeV, the luminosity — depending on the experiment — is around $10^{27}\,\mathrm{cm}^{-2}\mathrm{s}^{-1}$.

Different experiments are placed along LHC. The largest among them are:

1.1.1 CMS and ATLAS Experiments

The CMS and ATLAS[5] experiments are placed at the beam crossing points 1 and 5, respectively. Both CMS and ATLAS are general purpose experiments and will search for new particles and check different models of particle physics. The detectors are built symmetrically in $\pm z$ and cover approximately 4π sr. More information can be found e.g. in [3] (CMS) and in [4] (ATLAS). As

[1] Conseil Européenne pour la Rechèrche Nucleaire
[2] Large Electron Positron
[3] Proton Synchrotron
[4] Super Proton Synchrotron
[5] A Toroidal LHC ApparatuS

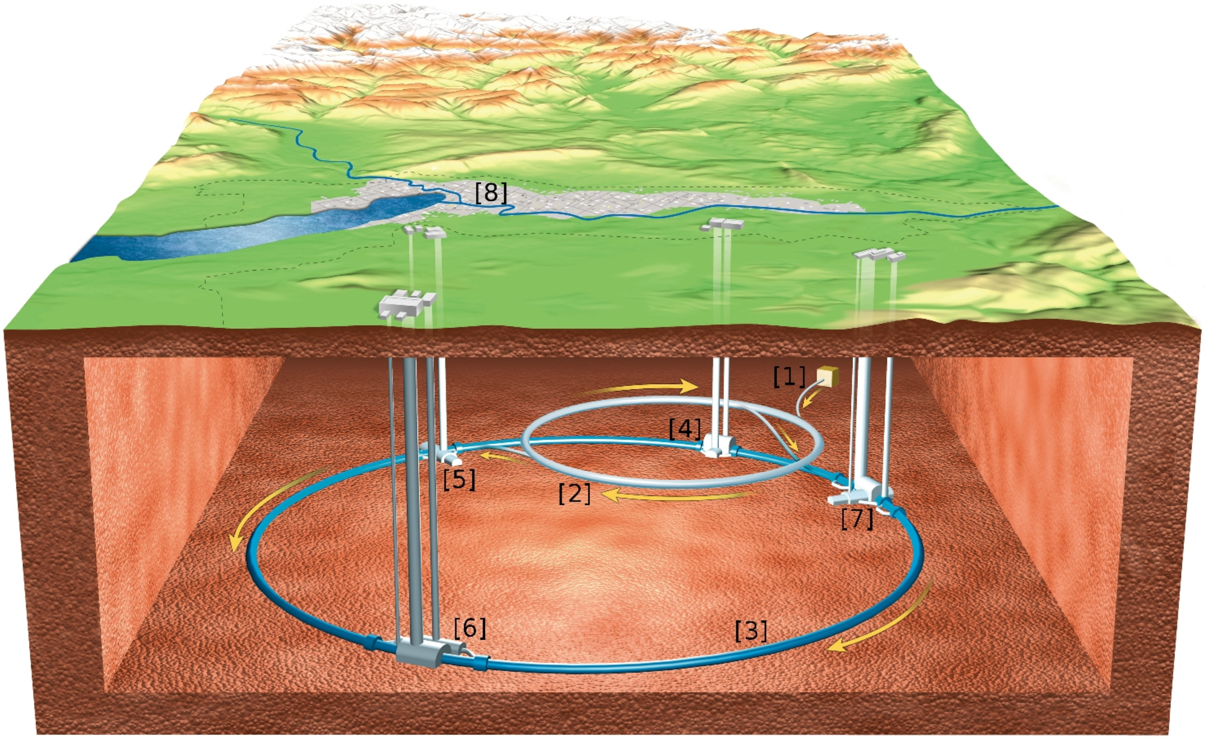

Figure 1.1: Location and experiments of LHC [2].
[1]: Preaccelerators, [2]: SPS accelerator, [3]: LHC accelerator, [4]: ATLAS experiment, [5]: LHCb experiment, [6]: CMS experiment, [7]: ALICE experiment, [8]: Geneva.

the report at hand is about the calibration of the pixel detector of CMS, only this experiment will be explained in more detail.

1.1.2 LHCb Experiment

The LHCb[6] experiment is placed at the beam crossing point 8 and designed to study mainly the physics of B hadrons and of the CP-violation. As B hadrons are expected to be observed under a relatively small angle with respect to the beam axis, the detector is built asymmetrically and covers mainly small angles ($10 \ldots 300\,\mathrm{mrad}$). The design luminosity is with $2 \cdot 10^{32}\,\mathrm{cm}^{-2}\mathrm{s}^{-1}$ significantly lower than in CMS and ATLAS experiments [5].

1.1.3 ALICE Experiment

The ALICE[7] experiment is placed at the beam crossing point 2. It is the only experiment dedicated to study heavy-ion collisions. Therefore it has to deal with a very high particle multiplicity, while the interaction rates with nuclear beams (about $10\,\mathrm{kHz}$) and the radiation doses (below $3000\,\mathrm{Gy}$) are rather low [6].

[6] Large Hadron Collider beauty
[7] A Large Ion Collider Experiment

1.1.4 TOTEM Experiment

The TOTEM[8] experiment is placed on both sides of the CMS experiment. In a first step, TOTEM is thought to run independently from the CMS experiment, later it will be included in CMS. It is dedicated to measure the total cross section of proton-proton interaction via elastic and inelastic scattering to better understand the protons structure. Therefore it covers small angles ϑ corresponding to a pseudorapidity $3.1 \leq |\eta| \leq 6.5$. The pseudorapidity is defined as

$$\eta \doteq -\log\left[\tan\left(\frac{\vartheta}{2}\right)\right], \tag{1.1}$$

where ϑ is the polar angle relative to the beam axis. The design luminosity is $10^{29}\,\mathrm{cm}^{-2}\mathrm{s}^{-1}$ with 156 bunches [7].

1.2 CMS Detector

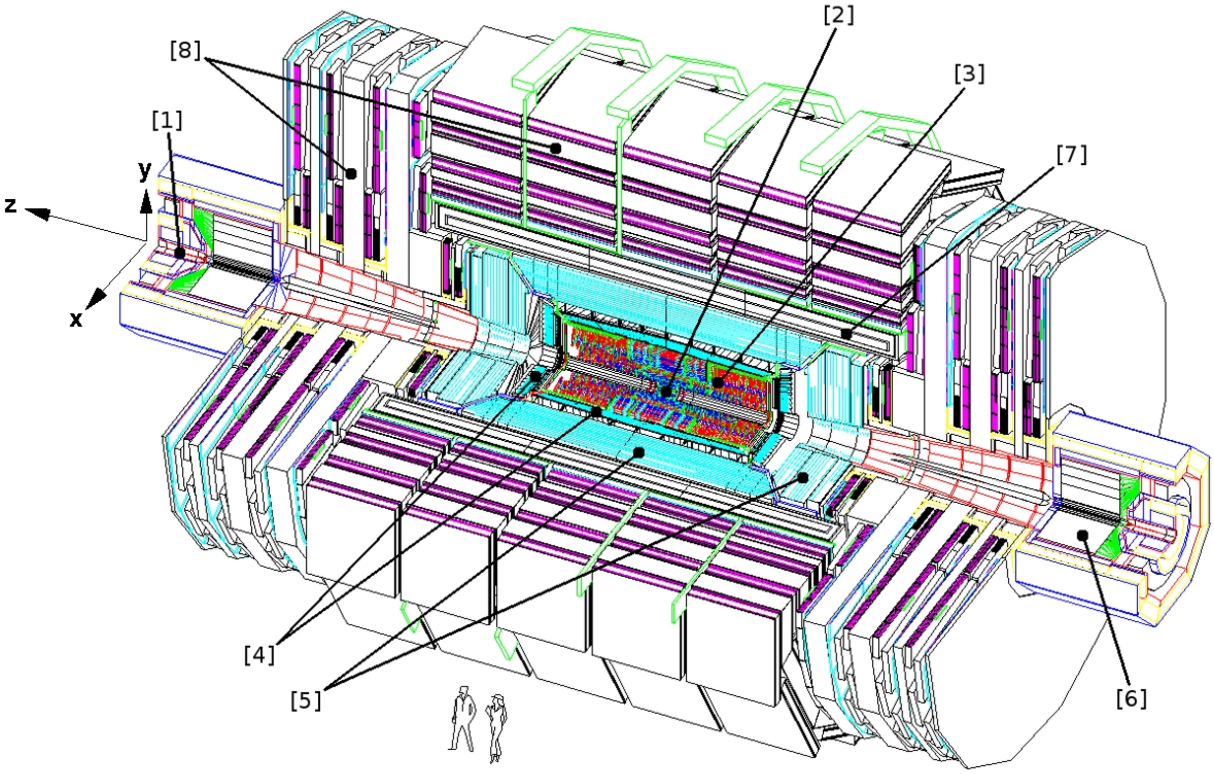

Figure 1.2: CMS and its subdetectors [8].
[1]: Beam pipe, [2]: Pixel detector, [3]: Strip detector, [4]: Electromagnetic calorimeter, [5]: Hadron calorimeter, [6]: Forward calorimeter, [7]: Superconducting magnet, [8]: Muon detector. The very forward detectors CASTOR and ZDC are not shown.

8 Total Cross Section, Elastic Scattering and Diffraction Dissociation at the LHC

The CMS detector has an overall length of 21.6 m, a diameter of 14.6 m and weights 12 500 tons. The coordinate system (see figure 1.2) of the CMS experiment is by convention chosen as described in table 1.1.

Table 1.1: CMS coordinate system.

Origin:	Interaction point in the center of the CMS detector
x-axis:	Towards the center of the LHC
y-axis:	Upwards
z-axis:	Following the beam pipe counter-clock wise
ϑ:	Polar angle relative to the positive z-axis
φ:	Azimuthal angle relative to the positive z-axis, $\varphi = 0\,^{\circ}\mathrm{C}$ at the x-axis
r:	Radial distance from the interaction point

The detector consists of several subdetectors that are built together in a onion-like structure as it can be seen in figure 1.2. The innermost subdetector just around the beam tube is the tracking system for the measurement of particle tracks and vertices with high resolution. The next outer shells are the calorimeters which determine the energy of particles interacting electromagnetically (electromagnetic calorimeter) and of hadrons (hadronic calorimeter). The superconducting solenoid that generates the magnetic field along the z-axis is placed around the calorimeters. The most outer and largest subdetector is the muon detector. The very forward detectors are spatially separated from the main detector and cover very low and very large angles ϑ. These subdetectors will be explained briefly in the following subsections.

1.2.1 Tracking System

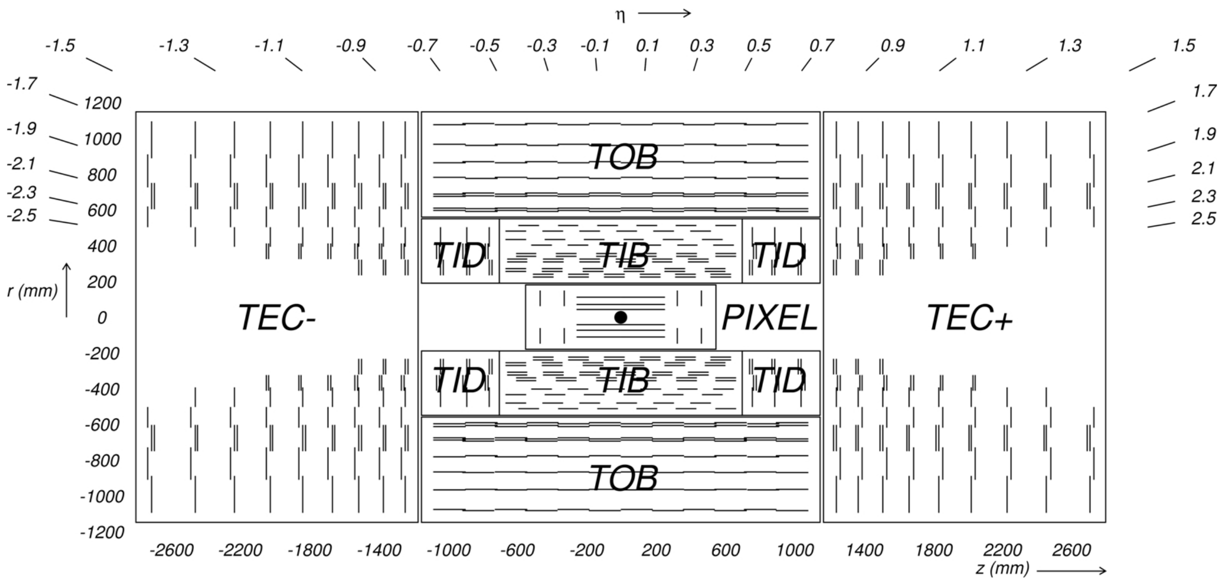

Figure 1.3: CMS tracking system [3].

The tracking system consists of several subdetectors, whose positions and η-coverage are shown in figure 1.3. While the pixel detector in the center works independently, the outer strip detectors form together a subdetector, often referred to as "tracker".

Central tracks that traverse the tracking system in the range $|\eta| < 2.4$ cross at least 9 active layers. At least 4 of them are two-dimensional from the pixel detector and from double strip detector modules.

In total, the tracker includes 9.3 million strips that cover $198\,\mathrm{m}^2$ and about 66 million pixels: 48 million pixels in the barrel pixel detector (BPix) and 18 million pixels in the forward pixel detector (FPix). They cover $0.78\,\mathrm{m}^2$ (BPix) and $0.28\,\mathrm{m}^2$ (FPix).

In terms of radiation length X_0, the material budget of the whole tracking system varies between $0.4X_0$ at $\eta = 0$ and $1.8X_0$ at $|\eta| = 1.4$.

Pixel Detector

The BPix detector is the very innermost subdetector just around the beam pipe. It consists of three 53 cm long, cylindrical layers of silicon pixel detectors at radii of 4.4 cm, 7.3 cm and 10.2 cm. The coverage of small angles ϑ is reached with the additional FPix detector consisting in total of 4 disks at $z = \pm 34.5\,\mathrm{cm}$ and $z = \pm 46.5\,\mathrm{cm}$ with inner radius 6 cm and outer radius 15 cm. Figure 1.4 shows the coverage of the pixel detector in terms of the pseudo rapidity η.

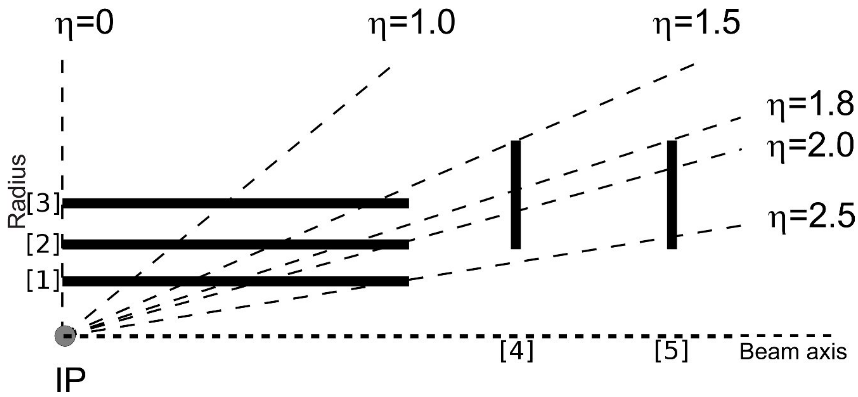

Figure 1.4: CMS pixel detector [3].
The dashed lines show the coverage of the three layers of BPix, [1], [2] and [3] and of the two discs of FPix, [4] and [5] in terms of the pseudorapidity η.

The pixel size of BPix is $100\,\mu$m in the $r\varphi$-direction and $150\,\mu$m in the z-direction with a spatial resolution of $15\ldots20\,\mu$m. This excellent resolution smaller than the pixel size can be achieved due to the large magnetic field of 4 T along z: The electrons and holes produced by a traversing particle are shifted in the $\pm\varphi$-direction by the magnetic field, such that they hit several pixels (charge sharing). From the distribution of the signal amplitudes of the hit pixels one can get this high resolution, which allows the three-dimensional detection of primary and secondary vertices.

The BPix detector is explained in more detail in the next chapter.

Inner Tracker

The inner part of the strip detector surrounds the pixel detector as shown in figure 1.3. The barrel detector (TIB[9]) contains 4 layers of longitudinally oriented strips at radii of 25.5, 33.9, 41.9 and 49.8 cm. The two endcaps (TID[10]) contain three identical disks each at z between ± 80 and ± 90 cm. Here the strips are radially oriented. As consequence, only r and φ of a hit are measured by the TIB, z and φ by the TID.

The pitch between strips is $80\,\mu$m for the inner two and $120\,\mu$m for the outer two layers of the TIB. This leads to a single hit resolution of $23\,\mu$m and $35\,\mu$m, respectively. For the TID, the pitch between strips depends on r and lies between $100\,\mu$m and $141\,\mu$m, which leads to a single hit resolution below $35\,\mu$m.

The thickness of the strips (r direction for the TIB, z direction for the TID) is $320\,\mu$m.

Outer Tracker

The outer tracker consisting of the TOB[11] and the TEC[12] detectors surrounds the inner tracker and contains the same active elements but larger: TOB consists of 6 layers of longitudinally oriented silicon strips at radii of 60.8, 69.2, 78.0, 86.8, 96.5 and 108.0 cm between $z = \pm 109.0$ cm. Each endcap of the TEC contains 9 wheels that extend radially from 22.0 to 113.5 cm and from ± 124.0 to ± 280.0 cm along the z-axis. Each wheel contains up to 7 rings. The 4 inner rings are $320\,\mu$m thick, the outer ones $500\,\mu$m as the TOB strips.

The pitch between strips is $183\,\mu$m for the 4 inner TOB layers and $122\,\mu$m for the 2 outer ones. The single hit resolution is 53 and $35\,\mu$m, respectively. For the TEC, the pitch between strips varies between 97 and $184\,\mu$m, leading to a single hit resolution below $50\,\mu$m.

Some layers and disks — they are drawn as double lines in figure 1.3 — contain additional modules of strips that are oriented azimuthally and provide measurements of the third coordinate (z in the TIB/TOB, r in the TID/TEC). The single hit resolution of these additional modules is $230\,\mu$m for the TIB/TID and $530\,\mu$m for the TOB/TEC.

1.2.2 Electromagnetic Calorimeter

The electromagnetic calorimeter (ECAL) of CMS is organized in 36 so called supermodules that form the barrel and in 4 dees that form the two endcaps. They are shown in figure 1.5. The high granularity of 360 in φ and of 170 in η in the barrel is reached with 61 200 crystals (endcaps: 14 648 crystals). The crystal axes are tilted in φ and η by $3\,^\circ$C against radial vectors from the interaction point to not loose tracks in dead material. The front end of the barrel crystals is at $r = 129$ cm, the front end of the endcap crystals at $z = \pm 315$ cm. The barrel covers $|\eta| < 1.479$, the endcaps cover $1.479 < |\eta| < 3.0$.

[9] Tracker Inner Barrel
[10] Tracker Inner Disks
[11] Tracker Outer Barrel
[12] Tracker End Caps

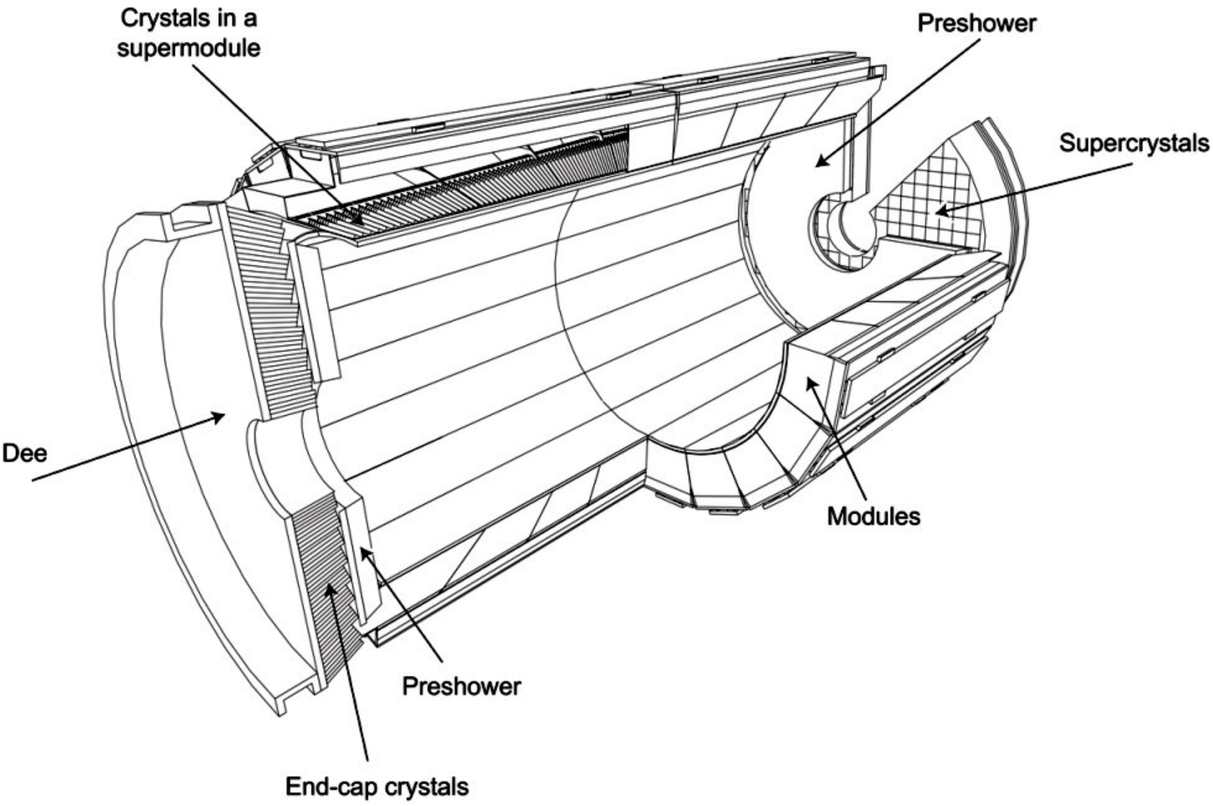

Figure 1.5: CMS electromagnetic calorimeter [3].

The crystals are lead tungstate ($PbWO_4$) with quadratic front and rear cross sections: $2.2\,\text{cm} \times 2.2\,\text{cm}$ and $2.6\,\text{cm} \times 2.6\,\text{cm}$ for the barrel and $2.9\,\text{cm} \times 2.9\,\text{cm}$ and $3.0\,\text{cm} \times 3.0\,\text{cm}$ for the endcaps. The width of the crystals is therefore in the order of the Molière radius (2.2 cm). Their length is 23 cm (barrel) and 22 cm (endcaps), which corresponds to $25.8X_0$ and $24.7X_0$, respectively.

The crystals emit 80 % of the blue-green scintillation light within 25 ns, which is the time between two bunch crossings. The readout of the emitted light is done with two avalanche photo diodes (APDs) per crystal in the barrel and with a vacuum photo triode (VPT) in the endcap. Both APDs and VPT collect 4.5 photoelectrons per MeV at 18 °C.

The high density (small radiation length) and the small Molière radius of the radiation hard $PbWO_4$ crystals allow a compact calorimeter with a high energy resolution. These are the main advantages of the homogeneous calorimeter compared to sampling calorimeters.

The preshower detectors on the inner side of the endcaps are sampling calorimeters with two layers of silicon strips orthogonal to each other and lead as radiators. They are dedicated to convert π^0 particles to photons that can be identified in the endcaps.

1.2.3 Hadron Calorimeter

The hadron calorimeter (HCAL) is a sampling calorimeter designed to measure the energy of hadron jets. Its 4 parts HB[13], HE[14], HO[15] and HF[16] are shown in figure 1.6 together with the muon detector (see section 1.2.4).

The pseudorapidity range $|\eta| < 1.3$ is covered by the HB, $1.3 < |\eta| < 3$ by the HE. Both are placed inside the magnet solenoid, which restricts together with ECAL the radius of the HB and HE to $177\,\mathrm{cm} < r < 295\,\mathrm{cm}$. The range $3 < |\eta| < 5.2$ is covered by the HF, which is placed at $z = \pm 1\,120\,\mathrm{cm}$ outside the solenoid.

The HB and HE consist of typically 15 layers of active material with absorber material in between parallel to φz-planes and to $r\varphi$-planes, respectively. The towers of layers are segmented, such that in each plane tiles of $(\Delta\eta, \Delta\varphi) = (0.087, 0.087)$ for the HB and of at most $(\Delta\eta, \Delta\varphi) = (0.17, 0.17)$ for the HE are read out.

Steel is the absorber material for the most inner and outer layers and brass (70 % Cu, 30 % Zn) for all others. Plastic scintillators (Bicron BC408 and Kuraray SCSN81) serve as active materials. They are read out via different wavelength shifting fibres (WLS's) by hybrid photo diodes (HPDs).

The absorber thickness corresponds to at least 5.84 interaction lengths λ_I at $\theta = 90\,^\circ$ with additional $1.1\lambda_I$ from the electromagnetic calorimeter.

A 19.7 cm thick piece of iron around the solenoid coil returns the magnetic field and increases together with the solenoid coil the minimal interaction length to $11.8\lambda_I$. The HO consists of an active layer outside this tail catcher iron and of an additional active layer between the solenoid coil and the tail catcher in the central barrel region around $\theta = 90\,^\circ$. It is dedicated to catch the tail of hadron showers. Its segmentation in φ and z matches the segmentation of the HB.

Due to the requirement of extreme radiation hardness, the HF had to be built differently and detects Cherenkov light instead of scintillation light, that the other hadron calorimeters use. It consists of a steel absorber structure with embedded quartz fibres along z. The fibres are of different length to separate γ particles from electrons. The depth of the HF is 165 cm, which corresponds to $10\lambda_I$.

1.2.4 Muon Detector

The muon detector consists of the muon barrel system (MB) and of the muon endcap system (ME). It is dedicated to detect muons, to measure their momentum and to trigger the readout of many other subdetectors. The position of the subsystems within the CMS detector is shown in figure 1.6.

The MB consists of 4 cylindric stations separated radially by 3 parts of the iron yoke that return the magnetic field. Between the iron plates, the magnetic field is weak and homogeneous enough

[13] Hadron Barrel calorimeter
[14] Hadron Endcap calorimeter
[15] Outer Hadron calorimeter
[16] Forward Hadron calorimeter

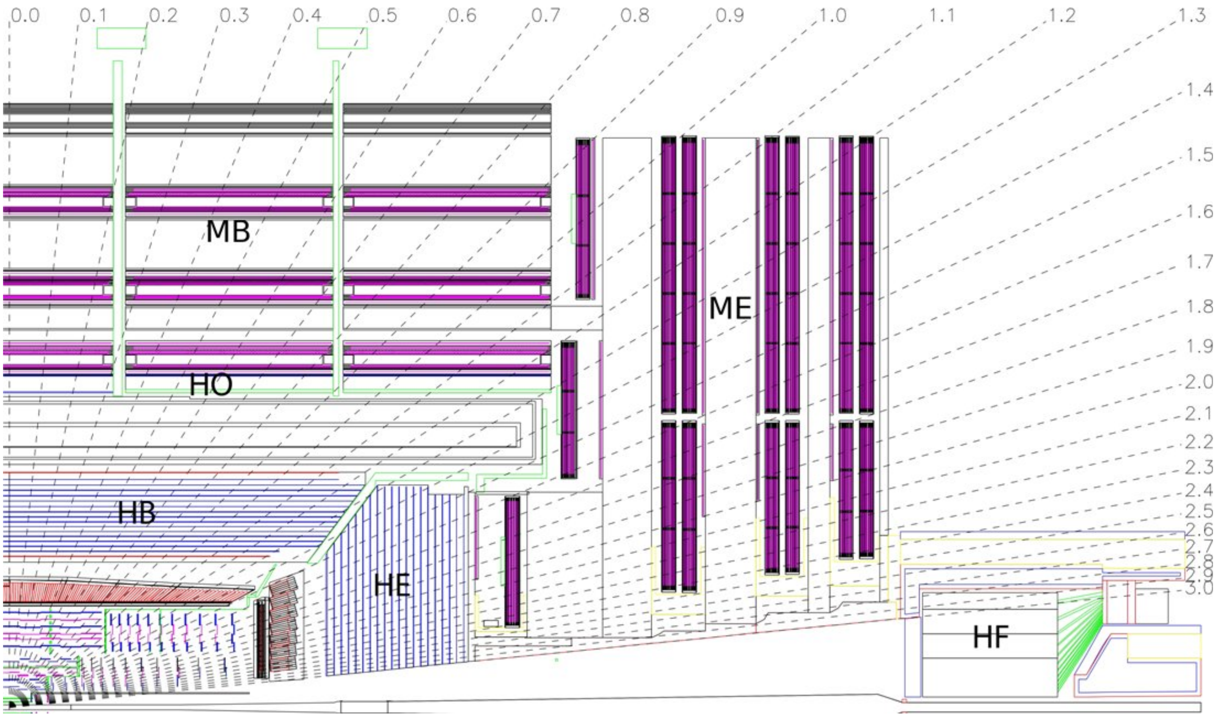

Figure 1.6: CMS hadron calorimeter and muon detector [3].
The main parts of the hadron calorimeter (HB and HE) are placed between the electromagnetic calorimeter and the solenoid, which is surrounded by the outer hadron calorimeter (HO) and the muon detectors MB and ME.
The dashed lines show the coverage of the subdetectors in terms of the pseudorapidity η.

to allow the operation of standard drift tubes (DTs). Their cross section of $1.3\,\text{cm} \times 4.5\,\text{cm}$ corresponds to a maximum drift time of 380 ns in the gas containing 85 % Ar and 15 % CO_2.

The DTs are organized in drift chambers: Each of the three inner stations contains 5 rings of 12 drift chambers along z, the outer station contains 5 rings of 14 drift chambers. Their length is limited to $\Delta z = 240\,\text{cm}$ by the segmentation of the iron yoke.

Drift chambers are made of 3 super layers (SLs): two with wires parallel to z (measuring φ), one with azimuthally oriented wires measuring z. (Azimuthally oriented wires are missing in station 4). Each SL contains 4 layers of parallel DTs. The cathodes are $50\,\mu$m thick gold-plated steel wires, the anode strips (on the sides) and the field-shaping electrodes (on top and bottom) are $50\,\mu$m thick aluminum stripes.

Outside the super layers are included RPCs[17] in the drift chambers. They serve as additional triggers.

The MB covers $|\eta| < 1.2$ with 12 dead zones in φ due to the iron yoke structure. Nevertheless, the efficiency of track reconstruction for high transverse momenta ($p_T > 40\,\text{GeV}$) by MB data only is above 95 % for $|\eta| < 0.8$, where a track passes all 4 stations. The global time resolution of a DT is a few nanoseconds, its spatial resolution in $r\varphi$ is in the order of $250\,\mu$m.

[17]Resistive Plate Chamber: double-gap chamber operated in avalanche mode

Because of the high rate and the strong and non-uniform magnetic field in the endcaps, cathode strip chambers (CSCs) are used in the ME instead of drift tubes. They cover $0.9 < |\eta| < 2.4$ and consist of 7 plates with azimuthal anode strips and of 6 layers with radial cathode strips in between. The wires are of $50\,\mu$m thick gold-plated tungsten.

The spatial resolution of single CSCs is about 2 mm on a trigger level and in the order of $100\,\mu$m in offline analysis. Muons traverse typically 3 or 4 CSCs.

1.2.5 Very Forward Detectors

The two small very forward detectors CASTOR[18] and ZDC[19] are not shown in figure 1.2. They are placed at $z = \pm 14.38\,$m (CASTOR) and $z = \pm 140\,$m (ZDC), respectively.

Both are mainly for low angle scattering and ion-ion collisions important and have to deal with a very high radiation.

CASTOR

CASTOR is a sampling calorimeter in concept similar to the HF: Covering $5.2 < |\eta| < 6.6$, it consists of plates of tungsten as absorber with fused quartz plates as active media in between. The plates and particle tracks enclose angles of $45\,^\circ$, such that a maximum of Cherenkov light reaches the photo multiplier tubes (PMTs).

The calorimeter is divided into an electromagnetic (closer to origin) and a hadronic part. They differ mainly in the thickness of the plates, which is 5 mm (tungsten) and 2 mm (quartz) for the electromagnetic part and twice that for the hadronic part.

The thickness of the electromagnetic part (10 double plates) corresponds to $20.1X_0$ $(0.077\lambda_I)$, the thickness of the hadronic part (60 double plates) to additional $9.24\lambda_I$.

Zero Degree Calorimeter

The ZDC is a calorimeter, that covers $|\eta| > 8.3$. It is built similarly to CASTOR: 33 vertically oriented tungsten plates (2 mm) and quartz plates (0.7 mm) corresponding to $19X_0$ form the electromagnetic part, while 24 tungsten plates (15.5 mm, tilted by $45\,^\circ$) and quartz plates (0.7 mm) corresponding to $6.5\lambda_I$ form the hadronic part.

[18] Centauro And Strange Object Research

[19] Zero Degree Calorimeter

2 Barrel Pixel Detector

This chapter covers aspects of the BPix detector relevant for this work. After an introduction to the components of the BPix detector in section 2.1, section 2.2 concentrates on the BPix readout system. Section 2.3 finally presents some DAC[1] parameters and their influence on the data acquisition.

2.1 Components of the BPix Detector

2.1.1 From Pixels to ROCs

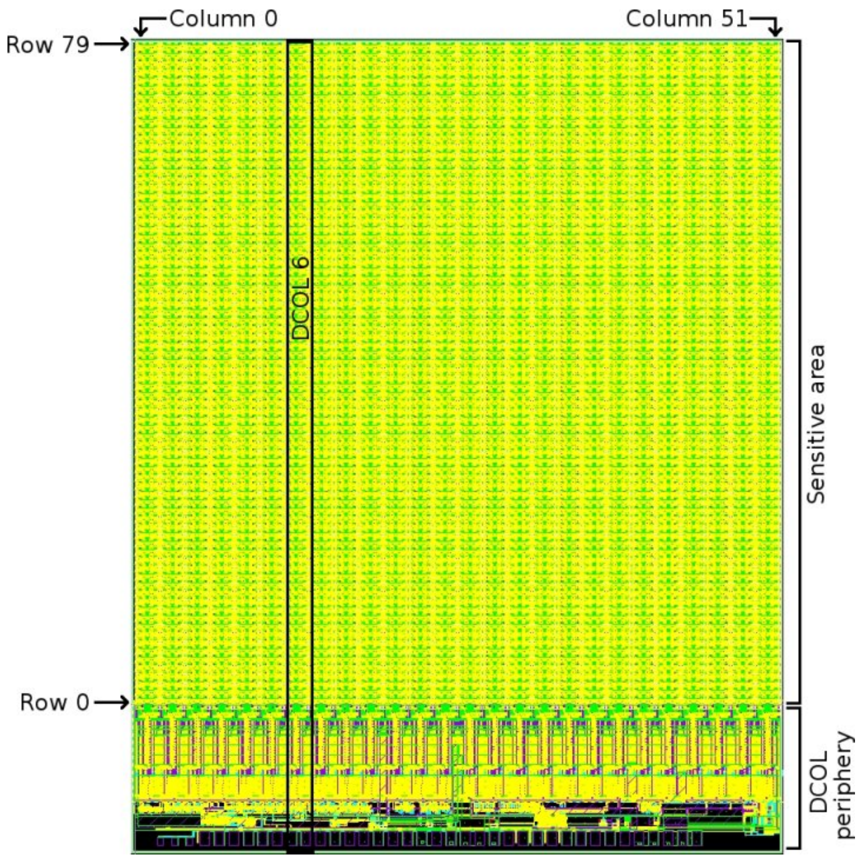

Figure 2.1: Illustration of a ROC [10].

[1]Digital to Analog Converter

The sensitive elements of the detector are pixels of size $\Delta z \times \Delta r\varphi = 150\,\mu\text{m} \times 100\,\mu\text{m}$ and of a thickness of $285\,\mu$m. They are organized in arrays of 80 rows $\times$ 52 columns = 4 160 pixels. These pixel arrays are bump-bonded to readout chips[2] (ROCs), where a pixel unit cell (PUC) belongs to each single pixel and provides the electronics for it. The PUCs are grouped in double columns (DCOLs) with buffers and readout electronics in the DCOL periphery. An illustration of a ROC with the DCOL periphery is shown in figure 2.1.

For more information see [9] for pixels and [10] for ROCs.

2.1.2 From ROCs to Modules

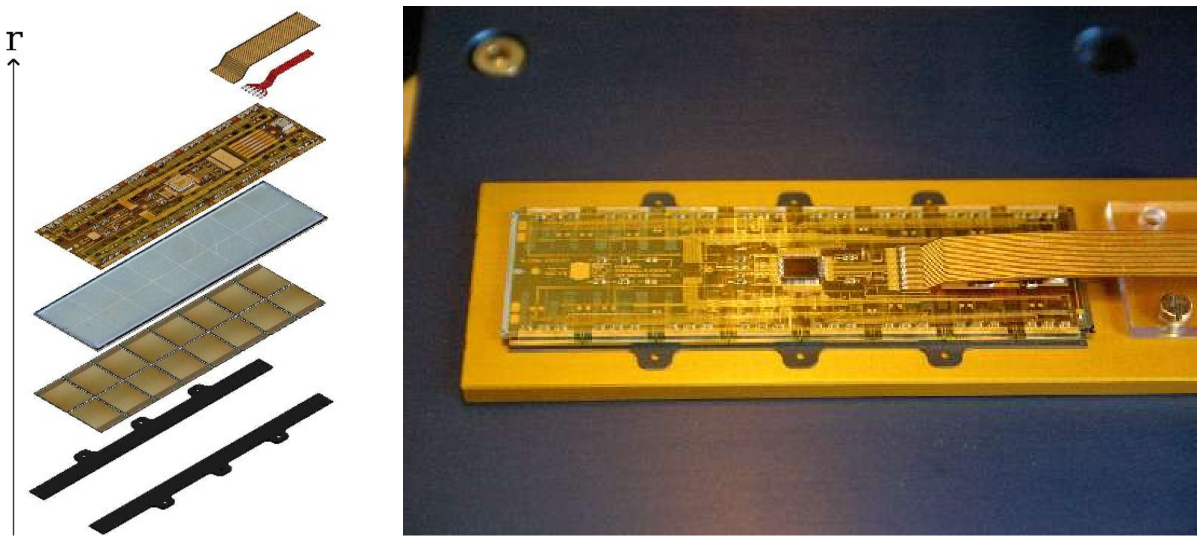

(a) (b)

Figure 2.2: Illustrations of a BPix module [11].
(a) Components of a BPix module. From top: signal cable, power cable, HDI, silicon sensor, 16 ROCs and base strips. (b) Picture of a module.

ROCs are organized in modules, forming the largest standardized units. There exist full modules of 2×8 and half modules of 8 ROCs, which are arranged in a way that the DCOL periphery is at the borders of the module. A module with its components is shown in figures 2.2. The ROCs with the grey silicon sensor bump bonded on top are mounted on base strips that provide mechanical stability. The periphery of the ROCs double columns is wire bonded to the high density interconnect (HDI) that provides readout and configuration electronics for the whole module. On top of the HDI is the token bit manager (TBM) which organizes the readout of the ROCs via the multi-channel kapton signal cable. In addition, the same kapton cable carries the control signals. The power cable provides the power and bias voltages.

A full module has a size of $\Delta z \times \Delta r\varphi = 66.6\,\text{mm} \times 26\,\text{mm}$ and a weight of 3.5 g.

[2]The chip version used for the BPix detector is psi46v2.1

2.1.3 From Modules to Layers

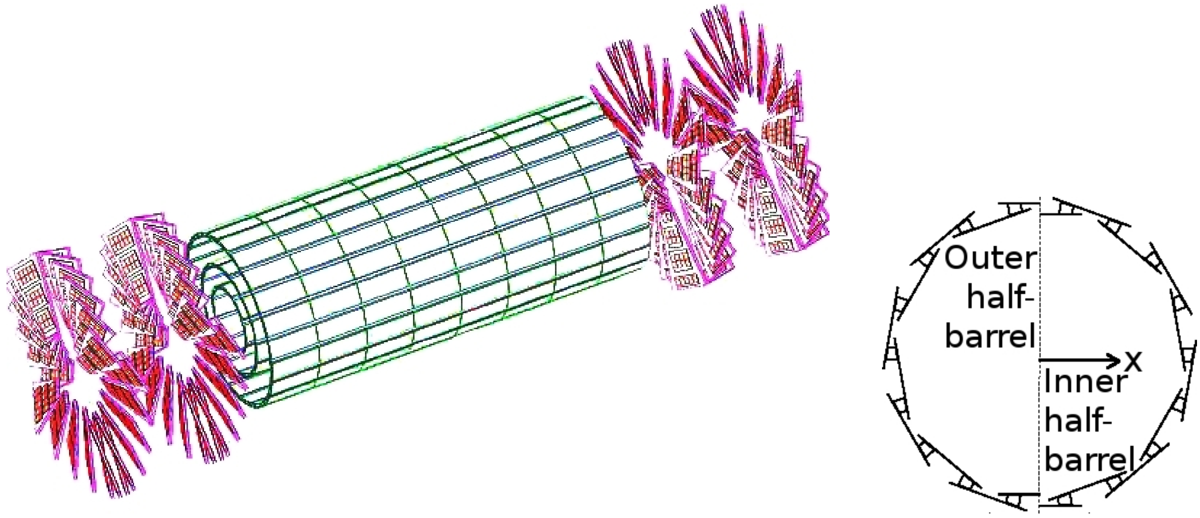

(a) (b)

Figure 2.3: Illustrations of BPix layers.
(a) Setup of the pixel detector with the three BPix layers of the length of 8 modules and the 4 FPix wheels [11]. (b) Cross section of layer 1 of the BPix detector [12].

Figures 2.3 show, how the (half-)modules are arranged to the 3 layers of the BPix detector: The modules and half-modules are mounted in an inner (positive x) and an outer (negative x) half-barrel. Half-modules are needed on top and bottom to fill the gap in the 2π-coverage of φ between the two half-barrels. Always 8 (half-)modules are longitudinally mounted together along z to cover the total length of 53 cm.

Layer 1 contains 8×16 modules and 8×4 half-modules.
Layer 2 contains 8×28 modules and 8×4 half-modules.
Layer 3 contains 8×40 modules and 8×4 half-modules.

Therefore the BPix detector consists of 672 modules and 96 half-modules. The total number of pixels in the BPix detector is therefore

$$[2 \cdot 672 \text{ (modules)} + 96 \text{ (half-modules)}] \times [8 \text{ (ROCs)}] \times [4\,160 \text{ (pixels)}] = 47\,923\,200.$$

2.2 Data Flux

Figure 2.4 shows the different steps of the pixel readout chain, of which the relevant ones will be explained in this and the following sections. More detailed information can be found in [14] and in the references given there.

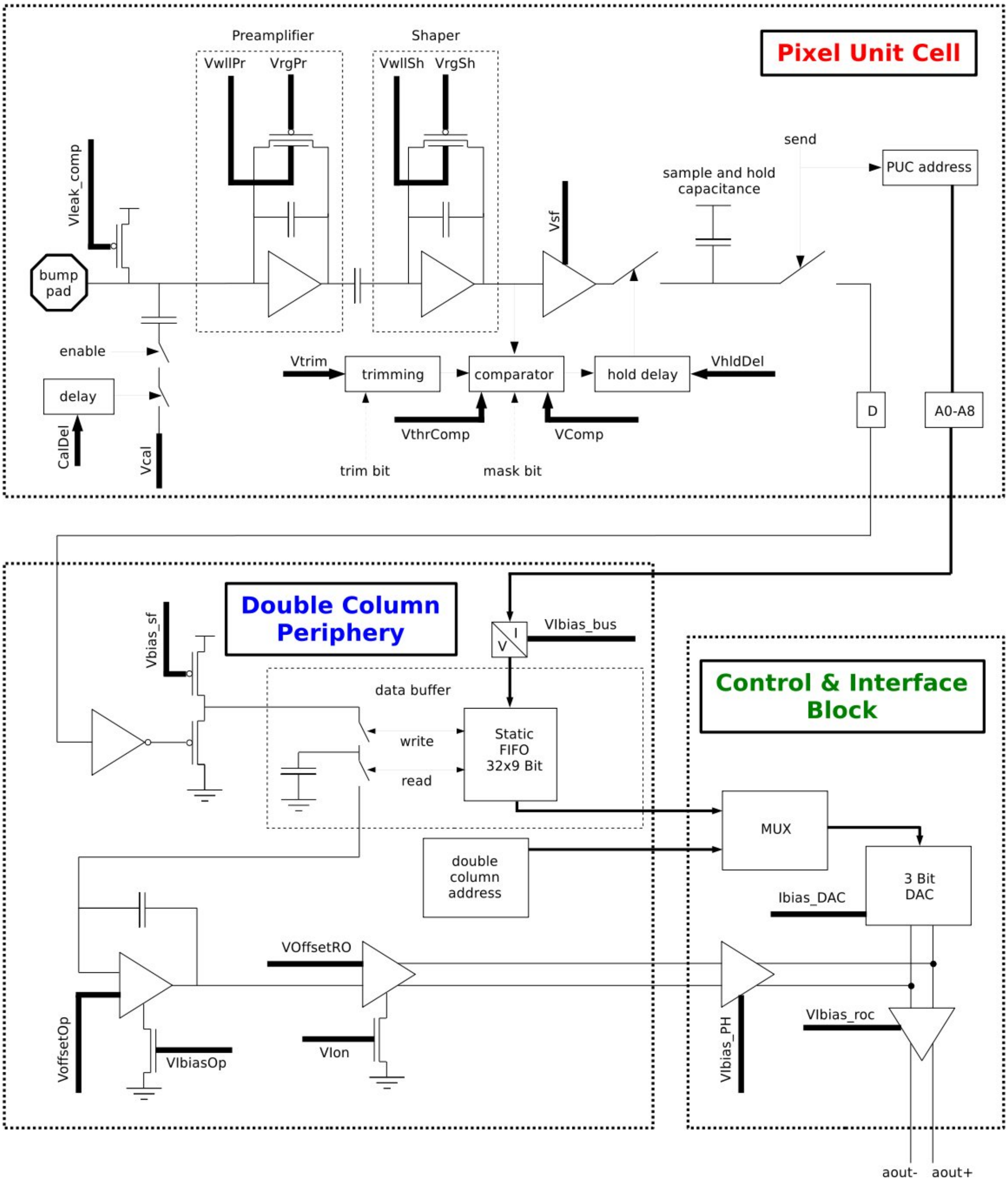

Figure 2.4: Schema of the pixel readout chain [13].

When a charged particle traverses a pixel, typically 20 000 electron-hole pairs are produced within the sensitive area of a pixel. This charge is pulled off by a bias voltage of about 150 . . . 600 V depending on the irradiation dose. In the PUC, the charge is collected and amplified. Every 25 ns it is compared to the preset threshold and — if it is above — stored within the PUC as a analog signal with a time stamp. The time information is sent within one clock cycle of 25 ns to the time stamp buffer in the DCOLs periphery, while the analog signal and the address of the hit pixel is sent to a second buffer within typically 6 clock cycles. This mechanism of reading the pixel signals and saving the data in the DCOLs buffers is called “drain” and takes place in parallel for all DCOLs. The time stamps and hit data are stored in the buffers for 3.2 μs due to the trigger latency. More than 32 recorded hits or more than 12 time stamps per DCOL lead to buffer overflow and can no more be stored. In this case the whole DCOL is temporarily blind. On average 2.2 pixels are hit per hit DCOL.

If the level 1 (L1) trigger decides to read out an event, the triggered data are sent zero suppressed through optical links to the readout electronics. The TBM organizes the access of the DCOLs to optical links. As optical links for the data serve analog optical hybrids (AOHs). The AOHs are placed with the digital optical hybrids (DOHs) in the service tube adjoining the pixel detector. The AOHs convert the electrical signals from the TBMs to optical signals and send them to the front end drivers (FEDs), while the DOHs handle the digital control signals from and to the front end controllers (FECs). FEDs and FECs are placed outside the detector in a control room and are linked to the pixel control system and the CMS data acquisition system (DAQ).

2.3 Relevant DAC Parameters

Each ROC contains 26 DACs for configuration and calibration. They are controlled by their corresponding DAC parameters. Most of them act on the ROC as a whole, only `TrimBit` can be defined differently per pixel. Those DAC parameters, which are relevant for this work, are presented in the following. All parameters are roughly described in [10].

By convention, DAC parameters are written in `DAC`-mode, while their physically corresponding variables are written in *physics*-mode. If nothing else is mentioned, the DAC parameters are 8-bit, i.e. they are integers in the range $[0, 255]$.

2.3.1 `Vcal`: Calibration Voltage

It is possible to inject a charge into the pixel simulating the charge deposited by a traversing particle for the calibration of the efficiency of a pixel (see figure 2.4). Therefore, the calibration voltage V_{cal} is applied to the pixel. It is supposed to be proportional to the injected charge and can be defined by the DAC parameter `Vcal`.

The 256 distinct values of `Vcal` do not provide a fine enough granularity or cover a too small range of V_{cal} and of injected electrons for many applications as for the study at hand. To cover a wider range of `Vcal` with an appropriate segmentation, different ranges are defined by `CtrlReg`. For this work, two settings of `CtrlReg` have been used: `Vcal` low range (LR) with `CtrlReg` $= 0$ and `Vcal` high range (HR) with `CtrlReg` $= 4$. The relation between LR and HR DAC units is

$$\texttt{Vcal}\ \text{HR} \approx 7 \cdot \texttt{Vcal}\ \text{LR}. \tag{2.1}$$

As both `Vcal` LR and `Vcal` HR are restricted to the range $0 \ldots 255$, `Vcal` HR covers the `Vcal` LR $0 \ldots 1\,785$ but with a coarser segmentation. The `Vcal` LR DAC values set voltages in the range $V_{cal} = 0 \ldots 280\,\text{mV}$, the `Vcal` HR DAC values set $V_{cal} = 0 \ldots 1\,800\,\text{mV}$. To calibrate `Vcal` DAC units to the number of electrons can be used the relation

$$1\ \texttt{Vcal}\ \text{LR DAC unit} \approx 65\ \text{electrons}. \tag{2.2}$$

However, for the analysis and simulation in chapters 4 and 5 has been used a more accurate value from the X-ray calibration, which is different for each pixel (see [15]). It is discussed in more detail in section 3.4.

2.3.2 `Vcthr`: Threshold

The DAC parameter `Vcthr` defines the threshold θ, to which the comparator compares the pulse height of a recorded signal. If the signal amplitude exceeds θ in the comparator, the signal is recorded as a hit in the buffer in the DCOL periphery.

`Vcthr` is inverted to θ, that is measured in units of `Vcal` or electrons. With `Vcthr` $= 0$ only very high amplitudes are accepted as hits, while with `Vcthr` $= 255$ very small signals as well as noise are interpreted as a hit, which leads immediately to buffer overflow. For the calibration of the threshold θ from `Vcthr` DAC units to `Vcal` LR DAC units and to electrons see section 3.4.

In addition to `Vcthr`, θ depends on the two other DAC parameters `Vtrim` (8 bit) and `TrimBit` (4 bit). While `Vcthr` only defines the highest possible threshold of a ROC, `Vtrim` defines the lowest possible threshold of the ROC. `TrimBit` finally is set individually per pixel and determines in 16 steps between the thresholds set by `Vcthr` and `Vtrim`, which threshold is valid for the concrete pixel. For the determination of these trim parameters see the diploma thesis by M. Waser [16]. Default values for the parameters `Vtrim` and `TrimBit` have been used for the analysis here, while `Vcthr` has been varied.

2.3.3 I_{ana}: Analog Current

The analog voltage V_{ana} is the voltage applied to the electronics in the PUC (preamplifier, shaper). The corresponding DAC parameter `Vana` regulates V_{ana} in the range 800 to $1\,300\,\text{mV}$. Nevertheless, for reasons of uniformity, cooling and highest overall efficiency, not V_{ana} but the analog current I_{ana} has been chosen to be the same for all pixels by I_{ana}-calibration. Although I_{ana} itself is not a DAC parameter, it can be treated as such in most cases. I_{ana} is set typically in the order of $24\,\text{mA}$.

2.3.4 `CalDel`: Calibration Delay

`CalDel` is like `Vcal` a DAC parameter, that plays a role for calibration only. It sets the time *CalDelay*, by which the charge insertion and with it the start of the calibration signal is artificially delayed with respect to the CalTrigReset signal.

The relation between *CalDelay* and `CalDel` is given in [10] as

$$CalDelay \approx 0.45\,\text{ns} \cdot (256 - \texttt{CalDel}) + 30\,\text{ns}. \tag{2.3}$$

This is contrary to the measurements presented in this study. As will be explained in section 3.7, it has been found

$$CalDelay = (0.4265 \pm 0.0046)\,\text{ns} \cdot \texttt{CalDel} + c. \tag{2.4}$$

The offset c has not been determined. For the simulations in chapter 5 we will use this latter relation.

The relation (2.4) might depend on temperature and differ among ROCs, which is not taken into account here. An overview of the different time-related DAC-parameters is given in figure 2.5.

2.3.5 `WBC`: Bunch Crossing Counter

`WBC`[3] is the DAC parameter that counts the bunch crossings back in time as shown in figure 2.5. It is needed as a time-code to read out the correct events from the DCOL periphery's buffer triggered by L1. Therefore one `WBC` unit corresponds to the time of one bunch crossing i.e. to 25 ns, and an event at larger `WBC` has happend earlier than an event with a smaller `WBC`.

For calibration signals, `WBC` can be treated as a coarse time parameterization that shifts the range of `CalDel`. A reasonable range of `WBC` is 98 . . . 100 to match the range of `CalDel`.

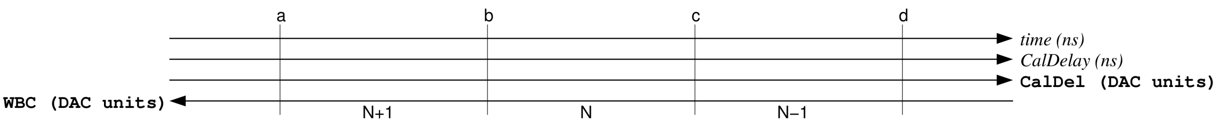

Figure 2.5: Relations of time, *CalDelay*, `CalDel` and `WBC`.
Let a, b, c and d be separated by 25 ns and $N+1$, N and $N-1$ be the `WBC` values of the corresponding bunch crossings. For a signal at time a being of the same shape as a signal at time b has either V_{cal} been applied $CalDelay = 25\,\text{ns}$ later (corresponding to a $\texttt{CalDel} = \frac{25}{0.4265} = 58.6$ larger) than b, or b has been read out with a $\texttt{WBC} = 1$ lower compared to a.

[3] Write Bunch Crossing

3 Measurements

After the definitions of in-time threshold and absolute threshold, a short overview of the scope of this work is given in section 3.1, followed by a description of the measurement setup in section 3.2 and the principles of threshold determination in section 3.3. In section 3.4 the calibration of θ from `Vcthr` to `Vcal` DAC units and to electrons is discussed. In the sections 3.5 to 3.8 are presented methodical and reproducibility checks as well as measurements that allow error estimations of the main analysis in chapter 4.

3.1 Scope of this Work

3.1.1 In-time and Absolute Thresholds

This work is about the determination of the threshold θ, to which signals from calibration or real events are compared in the comparator (see figure 2.4). Only signals above the threshold are referred to as event and are saved in the DCOLs periphery's buffer. Two thresholds are differentiated:

The absolute threshold θ_{abs} is defined as the minimal signal amplitude `Vcal`, for which the threshold θ (set by `Vcthr`) is reached. It can therefore be considered to be the threshold itself in `Vcal` units, which might be calibrated to units of electrons or pulse height (volts). θ_{abs} does not depend on any time parameterization as `WBC` or `CalDel`.

In contrast, the in-time threshold θ_{int} depends highly on the timing. It is the `Vcal` value a signal has to reach such, that it reaches the threshold θ *within the time window of the bunch crossing of interest.*

Figure 3.1 shows the difference between θ_{int} and θ_{abs}. Assume the BC of interest corresponds to the time between t and $t + 25\,\text{ns}$ and θ is set at b. Both red and blue signals starting at t, they reach their maximum approximately at the same time. But only the red signal reaches the threshold within the time window set by the `WBC`, while the blue signal reaches the threshold only in the time window with another `WBC` and will be interpreted as belonging to another event. Corresponding to the definitions above, the maximum amplitude of the red signal defines θ_{int} at a and the maximum amplitude of the blue signal θ_{abs} at b.

With θ_{abs} and θ_{int} one defines their difference as $\Delta\theta$:

$$\Delta\theta \doteq \theta_{int} - \theta_{abs}. \tag{3.1}$$

$\Delta\theta$ is always positive.

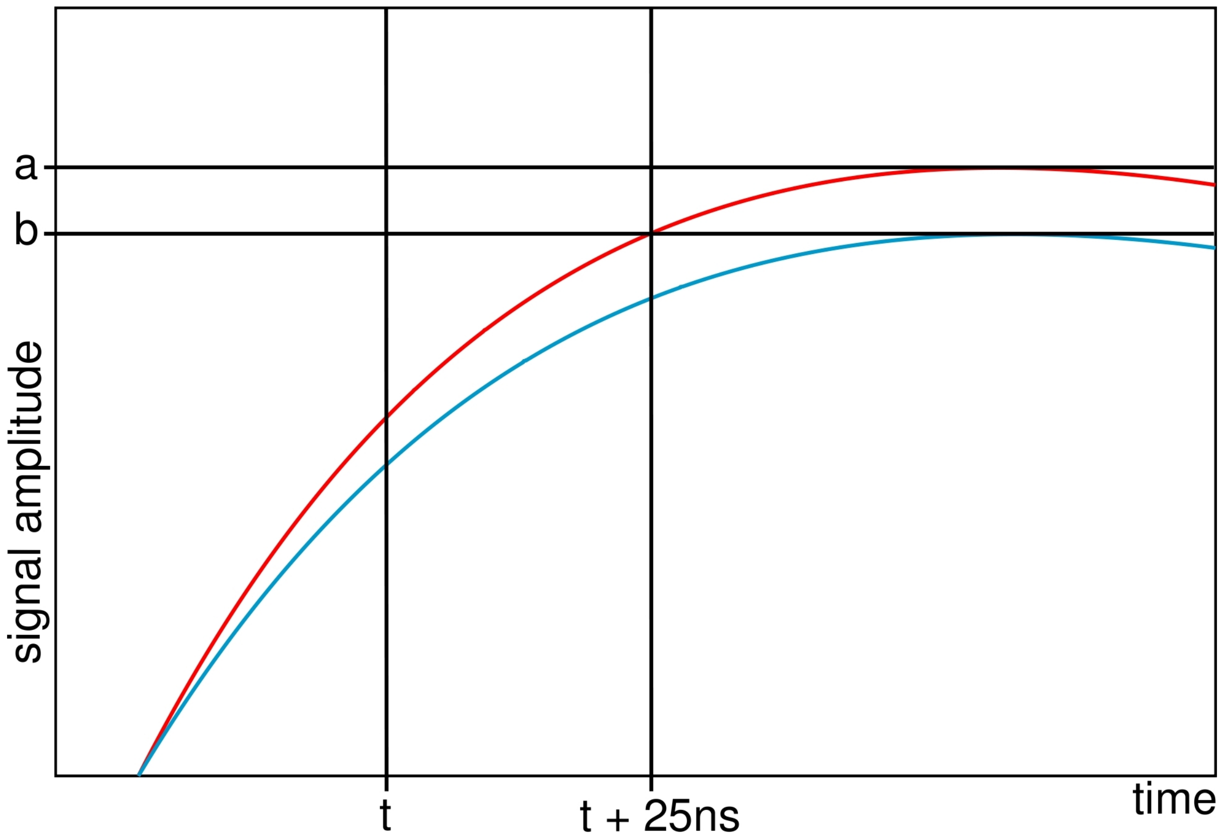

Figure 3.1: In-time (θ_{int}) and absolute (θ_{abs}) thresholds.
The red signal defines $\theta_{int} = a$, the blue signal defines $\theta_{abs} = b$.

3.1.2 Relevance of $\Delta\theta$

The scope of this work was to determine $\Delta\theta$ as a function of θ and to look further into dependencies on the analog current I_{ana} and on the temperature. $\Delta\theta$ was determined first by measurements (see chapter 4). In a second step, these results have been compared to the expectations with a simple simulation (see chapter 5).

Why is $\Delta\theta$ of interest? Due to the high collision rate of 40 MHz it is — with a reasonable cooling — not possible to amplify the signals fast enough, such that they reach their maximum within 25 ns. Therefore only that part of the rising edge of the signal, that lies within one BC, can be used to analyze, if the signal will reach the threshold and therefore to decide, if it belongs to a hit or not. One compares the signal amplitude with θ_{int}, while the physical threshold is θ_{abs}. This difference between θ_{int} and θ_{abs} can be compensated, if it is known with its dependencies.

The set of `Vcthr` values currently used for different ROCs covers a wide range due to different noise level, efficiency and signal amplification, although the physical thresholds can be adjusted by the two other DAC parameters `Vtrim` and `TrimBit`. It is currently not clear, which DAC parameters (and with it which thresholds) will be used for data taking and how widely they will be distributed among pixels and ROCs. This underlines the need of knowing about dependencies of $\Delta\theta$ and of the threshold calibration in general.

3.2 Experimental Setup

3.2.1 Experimental Hardware

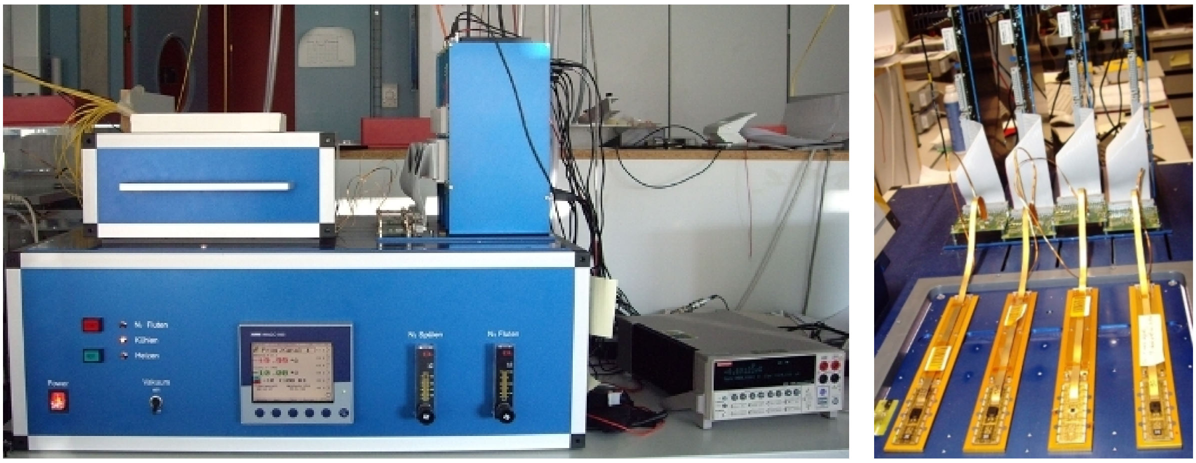

(a) (b)

Figure 3.2: Measurement setup.
(a) Closed cooling box (left) and read out units (center).
(b) Opened cooling box with 4 modules in the front and the read out electronics behind.

All measurements have been carried out at the Paul Scherrer Institute in Villigen, Switzerland. This decision was driven by the superior capabilities to control environmental influences such as the temperature at the laboratory facilities at PSI and by the higher availability for such measurements, in contrast to the place where the experiment is set up, namely at Cern.

A cooling box (see figure 3.2) provided constant temperature and was constantly flooded by nitrogen to avoid condensation on the sensors and attached electronics at low temperatures. The default temperature was 17 °C with 15.8 °C effectively measured (see chapter 4).

The data have been taken on the pixels in row 5, column 5 of the ROCs $0 \ldots 15$ of module M0090 on the module readout unit 0 if nothing else is mentioned. Module M0090 has been chosen because it meets the same quality criteria as the modules installed in CMS and has been calibrated by X-rays. The choice of the pixels in row 5, column 5 is arbitrary, only the outermost pixels of a ROC should not be considered due to larger pixels and boundary effects.

3.2.2 Experimental Software

All software code used for the measurements and analysis is based on the `root`-framework [17]. For the steering of the measurements the program `psi46expert` has been used via its graphic user interface (GUI), which is shown in figure 3.3. Most parameters could be set via this GUI. Only for changing I_{ana} the original `C++`-Code had to be changed and recompiled (in units of Ampère on the line 467 of the file `TestModule.cc`). The range of ROCs and pixels to be activated and read out can be defined in the lowest editable row of the GUI, while `Vcthr` (by `psi46expert` called `VthrComp`) as well as LR(`CtrlReg` = 0)/HR(`CtrlReg` = 4) are set two lines above.

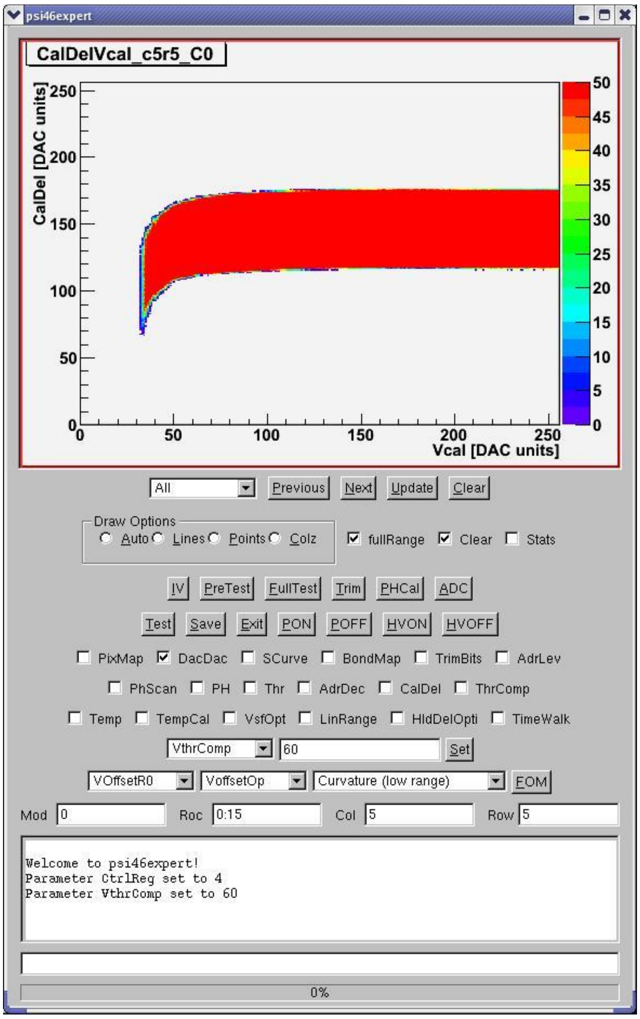

Figure 3.3: The GUI of `psi46expert`.

This screenshot has been taken after a HR scan of the number of readouts as a function of `Vcal` and `CalDel` at `Vcthr` = 60 for the pixel in column 5, row 5 for all 16 ROCs.

The main feature of `psi46expert` used for this study is the ability of measuring the number of readouts (i.e. the number of signals above the threshold) in a two dimensional scan of two arbitrary DAC parameters. These parameters as well as the number of triggers have been adapted to the respective needs on the lines 3 to 5 of the file `testParameters.dat`. The default values of the DAC parameters are ROC-wise defined in the files `dacParameters_C<ROC-nr>.dat`. Changes of the `WBC` have been done in these files.

After having changed I_{ana} or for measurements at different temperature, `PreTest` was run for setting DAC parameters (mainly `Vana`), followed by a `PixMap` check to see, if the parameters were set reasonably. If I_{ana} and the temperature remained stable, it was not necessary and unwanted to repeat `PreTest` between two measurements. The parameter settings have always been saved and could be reloaded (without subsequent `PreTest`), when failed measurements had to be repeated later or when long measurements had been divided into several shorter measurements.

3.3 Threshold Determination

In this section is explained, how the macro `threshold.C` determines θ_{int} and θ_{abs} using data taken with `psi46expert`.

3.3.1 Measured Data

For the main measurements, the number of readouts was measured as a function of `Vcal` and `CalDel`, once in `Vcal` HR mode and once in `Vcal` LR mode. In the following HR or LR measurements will be referred to as "scans", both together are called a "measurement". Such measurements have been done for different parameter settings (see chapter 4).

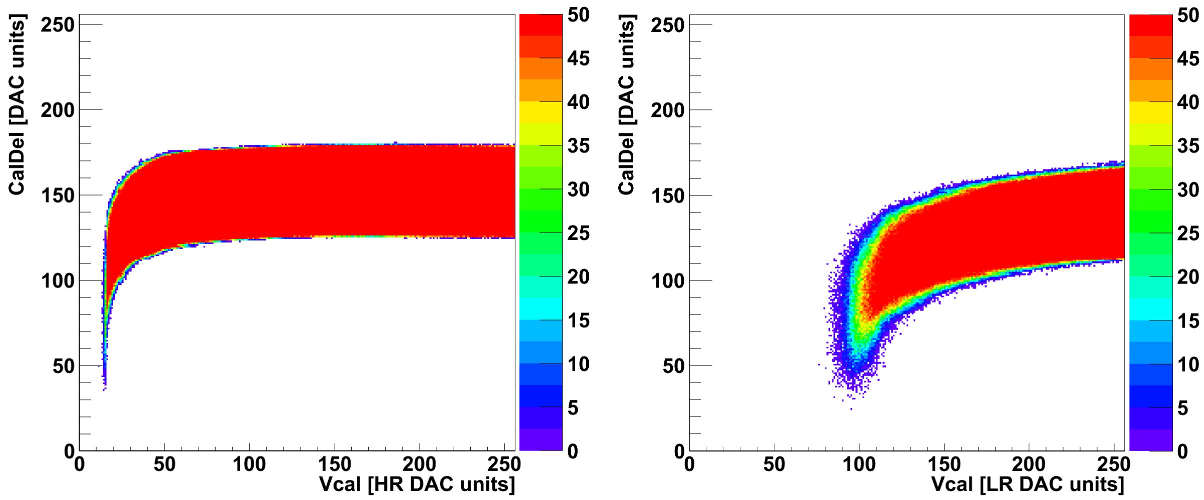

(a) HR scan (b) LR scan

Figure 3.4: Measurement of the number of readouts vs. `Vcal` and `CalDel`.
For this measurement has been set `Vcthr` = 60 with 50 triggers.

The scans of a measurement are shown in figures 3.4. To get one data point, a charge corresponding to `Vcal` is injected to the pixel with a delay set by `CalDel`. If the resulting signal exceeds θ (set by `Vcthr`) within the time window defined by `WBC`, it is interpreted as a hit and 1 is returned, otherwise 0 is returned. This procedure is repeated 50 times, therefore the bin content of the histograms is in the range $0 \ldots 50$ corresponding to a readout probability of $0 \ldots 1$ with 0.02 step size.

3.3.2 Determination of θ_{int}

Principle of θ_{int} Determination

Starting with plots as shown in figures 3.4a and 3.4b, the `CalDel` value of the lower asymptote of the HR plot is determined (see figure 3.5a). This `CalDel` value at 50 % readout probability at the highest possible `Vcal` is called $\texttt{CalDel}_{\texttt{LA}}$. It corresponds to the earliest possible starting time

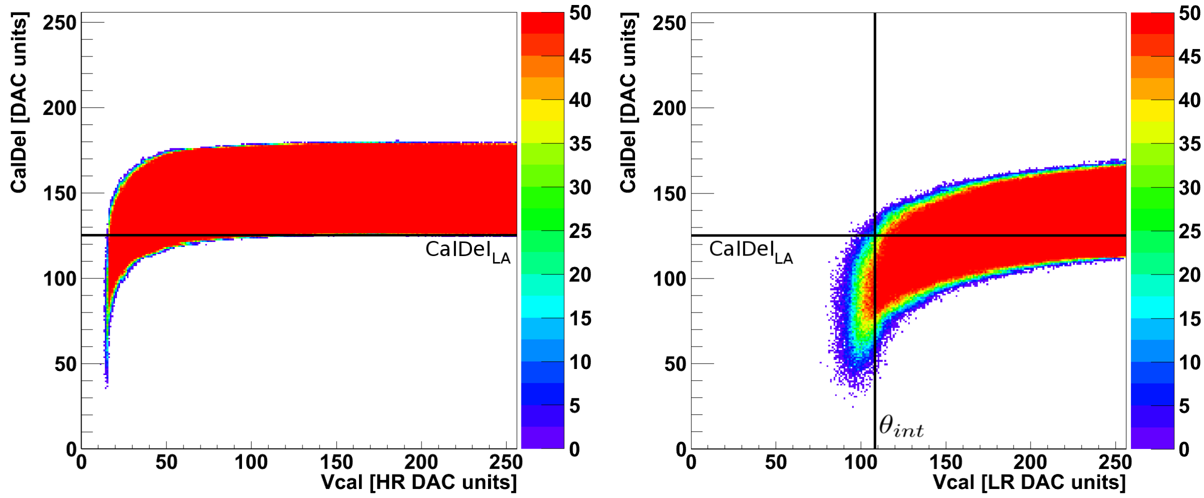

(a) HR scan (b) LR scan

Figure 3.5: Getting `CalDel`$_{LA}$ and θ_{int}.
The black horizontal lines at `CalDel`$_{LA}$ are found as the lower asymptote in the HR scan (a), out of which the black vertical line at `Vcal` $= \theta_{int}$ is determined in the LR scan (b).

of large signals that reach θ within the bunch crossing of interest and opens the time window of the corresponding `WBC`.

The determination of `CalDel`$_{LA}$ is the only reason for taking the HR scan. For all further steps only low range data is used due to higher resolution in `Vcal`. As `CalDel` is the same for HR and LR, one can transfer `CalDel`$_{LA}$ without complications from HR to LR (figure 3.5b).

Extending the lower asymptote from large towards low `Vcal`, the `Vcal` value, where the number of readouts is 50 % of the number of triggers, is the in-time threshold θ_{int} according to the definition of section 3.1.1 as the smallest signal, that reaches the threshold within the selected `WBC`. Smaller signals (in the figure 3.5b all bins left from the vertical line) might still reach θ, but as they have started earlier, they belong to another bunch crossing (with a larger `WBC` value).

Determination of θ_{int} by `threshold.C`

Determination of `CalDel`$_{LA}$

Five one dimensional histograms are filled with the entries of all `CalDel` values for the five largest `Vcal` values of the HR scan. These are the `Vcal` values 255, 254, 253, 252 and 251. To each histogram an SCurve fit is applied twice. Once with rising `CalDel` to determine `CalDel`$_{LA}$ and once with falling `CalDel` to determine the upper asymptote `CalDel`$_{UA}$. `CalDel`$_{UA}$ and `CalDel`$_{LA}$ are set to the mean value of the five SCurve fit results.

SCurve Fit

When an SCurve fit is applied to a histogram, the following procedure is used: The first series of 4 bins with 100 % readouts (usually 50 because of 50 triggers) after the rising edge is determined, and all following bins are set to 100 % readouts. Next, the function

$$f(x) = a \cdot \mathrm{Erf}\left(c \cdot (x - b)\right) + d \quad \text{with} \quad \mathrm{Erf}(x) = \frac{2}{\sqrt{\pi}} \cdot \int_0^x e^{-t^2} dt \tag{3.2}$$

is fitted to the modified histogram. The modification avoids failing fits due to falling entries in ranges out of interest. Binomial errors have been used for all fits, i.e. the errors of the single points to fit have been set to

$$N \cdot \sqrt{\left| \frac{w \cdot (1 - w)}{N} \right|} \quad \text{with} \quad w = \frac{n}{N}, \tag{3.3}$$

where n is the bin content and N the number of triggers. For bins having $n = 0$ or $n = N$, n has been set to 0.005. An example of an SCurve fit can be seen in figure 3.6. The fitted range is restricted to the points between the first series of 4 points with 0 % readout probability and the first series of 4 points of 100 % readout probability.

The parameters a, b, c and d of the fit function have the following impact:

- a: Stretches the Erf-function, which is normalized to 1, to the number of triggers. Default: $a = 25$ for 50 triggers.
- b: Provides the value of interest. It is the value of the x-axis, at which the fit function reaches 50 % of its maximum. The default value of b is determined dynamically and may be in the whole DAC-range.
- c: Defines the slope of f. Default: $c = 0.1$.
- d: Offset, shifts Erf(0) from 0 to 50 % of the number of triggers. Default: $d = 25$.

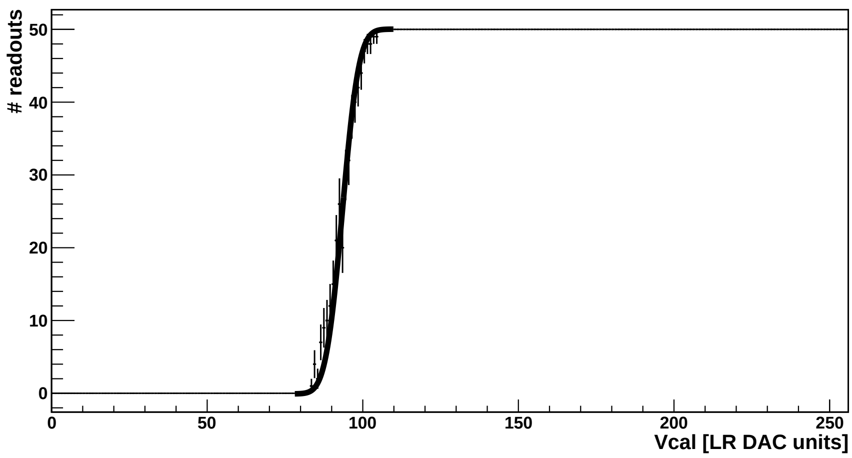

Figure 3.6: SCurve fit for the determination of $\theta_{\texttt{CalDel}}$.
With such SCurve fits of the number of readouts as a function `Vcal` at a fixed `CalDel` is determined the `Vcal` value $\theta_{\texttt{CalDel}}$, at which the number of readouts exceeds 50 %.

Determination of θ_{int}

As the accuracy of $\texttt{CalDel}_{\texttt{LA}} = b$ provided by an SCurve fit is a double, but `CalDel` values are integers by construction, it is set $\texttt{CalDel}^{\texttt{r}}_{\texttt{LA}} \doteq (\texttt{CalDel}_{\texttt{LA}}$ rounded to an integer).

A SCurve fit is applied now to determine the `Vcal` value, at which the number of readouts exceeds 50 % for a fixed `CalDel` value. This `Vcal` value is called $\theta_{\texttt{CalDel}}$ — it is the minimum `Vcal` value, for which signals that start at the time corresponding to `CalDel` reach the threshold. Such an SCurve fitted to the number of readouts as a function of `Vcal` is shown in figure 3.6.

$\theta_{\texttt{CalDel}}$ is determined for all 7 `CalDel` values between $(\texttt{CalDel}^{\texttt{r}}_{\texttt{LA}} - 3)$ and $(\texttt{CalDel}^{\texttt{r}}_{\texttt{LA}} + 3)$. The considered `CalDel` values are those around the horizontal black line in figure 3.5b. Next, a linear curve is fitted to a graph `CalDel` vs. $\theta_{\texttt{CalDel}}$ containing these 7 points. Such a linear fit can be seen in figure 3.7. The curve provides $\theta_{\texttt{CalDel}}$ as a function of `CalDel`, where `CalDel` as argument is no more restricted to integers. The function evaluated at $\texttt{CalDel}_{\texttt{LA}}$ provides finally θ_{int}.

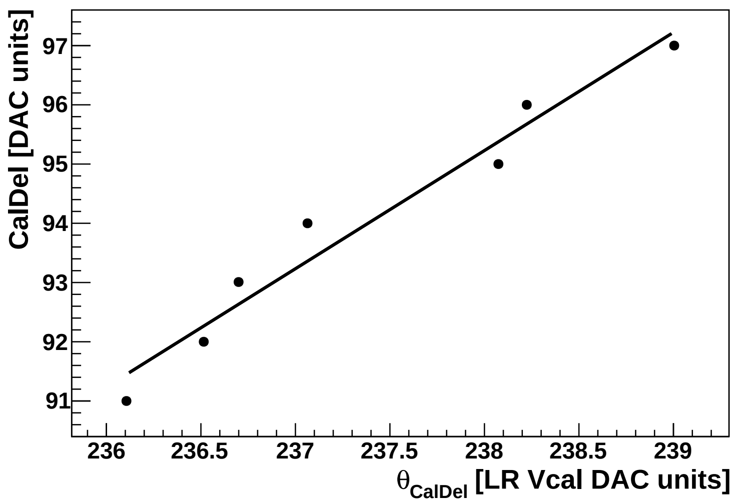

Figure 3.7: Linear fit providing $\theta_{\texttt{CalDel}}(\texttt{CalDel})$ for the θ_{int} determination.

Error Determination of θ_{int}

The error of θ_{int} is set to the RMS of the distribution of the 7 $\theta_{\texttt{CalDel}}$ values. Mainly two sources contribute to the error of θ_{int}:

- Statistical fluctuations: Although many `Vcal` values at $\texttt{CalDel}^{\texttt{r}}_{\texttt{LA}}$ are used to determine $\theta_{\texttt{CalDel}}$ by an SCurve fit, it fluctuates. The effect of these fluctuations is reduced by the evaluation of the linear fit from 7 `CalDel` values. However, if more than 7 `CalDel` values were considered to reduce the fluctuations further, the upper curve of 50 % read out signals of the LR scan can no more be considered to be linear, leading to a larger systematic error.
- The just mentioned upper curve has typically a slope of 1 in the `CalDel` range of interest for θ_{int}. This introduces an error of up to 0.5 `Vcal` units to single $\theta_{\texttt{CalDel}}$ due to rounding of $\texttt{CalDel}_{\texttt{LA}}$ to $\texttt{CalDel}^{\texttt{r}}_{\texttt{LA}}$.
- An additional error that is not considered here is introduced already by the determination of $\texttt{CalDel}_{\texttt{LA}}$, that fluctuates statistically. However, this error is supposed to be small compared to the others, as an average of 5 `Vcal` values is considered do determine $\texttt{CalDel}_{\texttt{LA}}$. As can be seen in figure 3.5a, the fluctuations are very small for large `Vcal` values.

3.3.3 Determination of θ_{abs}

Principle of θ_{abs} Determination

Starting with the LR scan already used for the θ_{int} determination (see figure 3.4b), θ_{abs} in LR `Vcal` units is just the smallest `Vcal` value at any `CalDel`, at which the readout probability is 50 %. In somewhat extreme cases, where the first entries at low `Vcal` form a vertical line as shown in figure 3.8a, this is easy to be determined. However, in most cases (depending on parameter settings that will be discussed later in this chapter), there is no such vertical line and θ_{abs} depends strongly on the selected determination algorithm and cuts (see figure 3.8b). The uncertainty in the θ_{abs} determination would be in the order of several LR `Vcal` units and with it in the order of $\Delta\theta$, which is not acceptable.

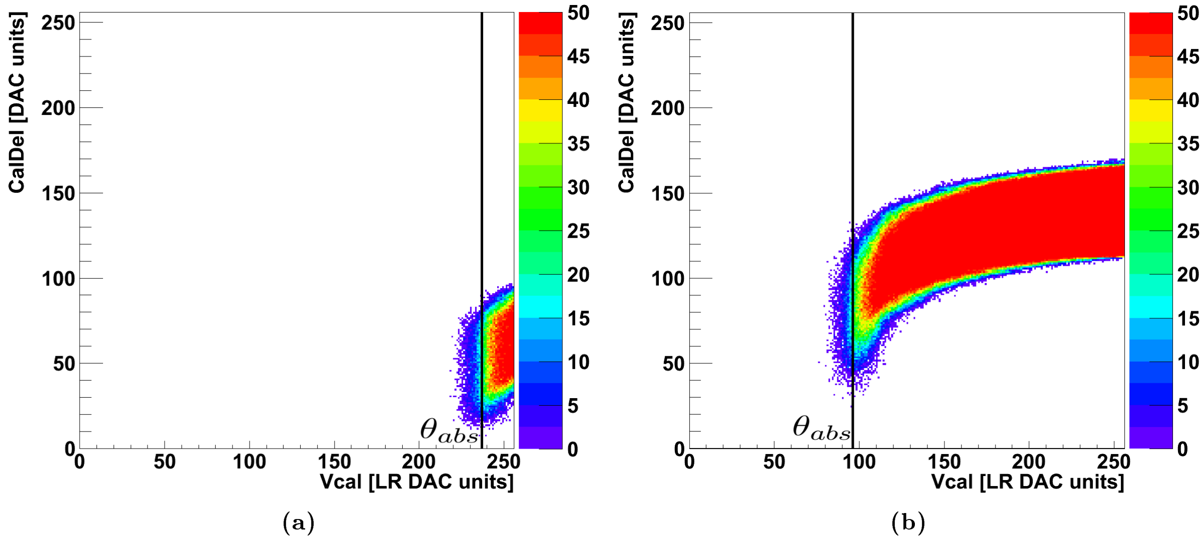

Figure 3.8: Difficulty of the θ_{abs} determination depending on parameter settings. While the determination of θ_{abs} (vertical lines) as the lowest `Vcal` values with 50 % readout probability is clear in cases as in (a), it is not well defined in cases as in the example from the θ_{int} determination (b).

The problem is, that in these cases the signals at low `Vcal`, that should define θ_{abs} building a vertical line, are distributed over several `WBC`s, while only one is measured by default. This leads to a large systematic error.

In order to avoid this, one can repeat the LR scans for two additional `WBC`s before and after the default one and finally merge the three histograms into one. While this has hardly any effect on the θ_{abs} determination in cases as in figure 3.8a, θ_{abs} can be determined clearly also in cases as in figure 3.8b. Figure 3.9a shows this exemplarily. The LR scan measurement of figure 3.8b has been repeated twice with `WBC` set to 98 and 100, respectively. In the sum of the three plots shown here the signals at low `Vcal` build a vertical line and θ_{abs} can be easily determined.

The obvious disadvantage of this method is a doubling of the scans to take. (One LR and one HR scan are taken by default plus two LR scans for additional `WBC`s. There is no need to take additional HR scans, as HR scans are not at all needed for the θ_{abs} determination.)

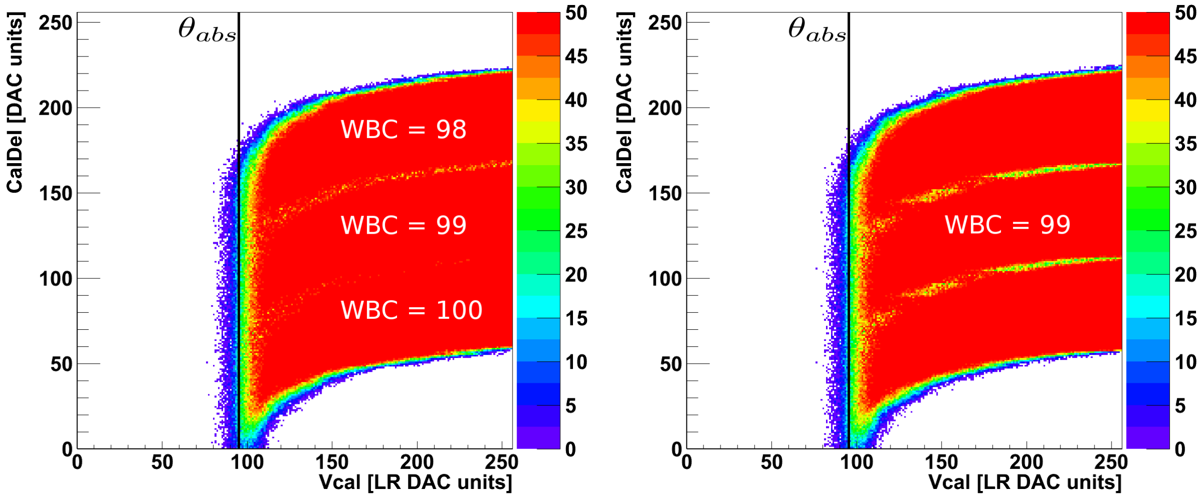

(a) (b)

Figure 3.9: Merged LR histograms from different `WBC`s.
Vertical lines represent θ_{abs}. The maximum bin content has been set artificially to 50 to provide the same color scale in both figures. Due to statistical fluctuations occur bins with more than 100 % read out signals.
(a) 3 LR scans measured with 3 different `WBC` values (among these the scan of figure 3.4b) are merged into one.
(b) The LR scan of figure 3.4b is shifted numerically by $\pm\Delta\mathtt{CalDel}_{\mathtt{LR}}$ (corresponding to ±1 `WBC`) and merged with the shifted scans into one.

It is important to note, that the `WBC` value is arbitrarily chosen such, that the whole plot lies in the range $0 \leq \mathtt{CalDel} \leq 255$. Choosing a neighboring `WBC` value just shifts the plot by about −56 `CalDel` units for one `WBC` unit above and by about +56 `CalDel` units for one `WBC` unit below. The measured data is — except for statistical fluctuations — exactly the same. Therefore it is possible to simulate scans of different `WBC`s by shifting the whole scan by the number of `CalDel` units corresponding to one `WBC` unit, if this correspondence is known well enough.

One can determine the upper ($\mathtt{CalDel}_{\mathtt{UL}}$) and lower limits ($\mathtt{CalDel}_{\mathtt{LL}}$) of `CalDel` for large `Vcal` values in the LR scan by the same algorithm that has been used to determine $\mathtt{CalDel}_{\mathtt{UA}}$ and $\mathtt{CalDel}_{\mathtt{LA}}$ in the HR scan. Their difference, $\Delta\mathtt{CalDel}_{\mathtt{LR}} \doteq \mathtt{CalDel}_{\mathtt{UL}} - \mathtt{CalDel}_{\mathtt{LL}}$, is the number of `CalDel` units that corresponds to 1 `WBC` unit or 25 ns. Now it is possible to shift the LR scan numerically by $\Delta\mathtt{CalDel}_{\mathtt{LR}}$ with no need to take scans with different `WBC` values. In principle one could determine the shift from the HR scan as $\Delta\mathtt{CalDel}_{\mathtt{HR}} \doteq \mathtt{CalDel}_{\mathtt{UA}} - \mathtt{CalDel}_{\mathtt{LA}}$ instead. Because of the higher accuracy of the SCurve fits in the LR scans it was decided to shift by $\Delta\mathtt{CalDel}_{\mathtt{LR}}$. $\Delta\mathtt{CalDel}_{\mathtt{LR}}$ and $\Delta\mathtt{CalDel}_{\mathtt{HR}}$ will be investigated in more detail in section 3.7.

Figure 3.9b shows the scan of figure 3.9a with $\mathtt{WBC} = 99$ merged with this scan shifted numerically by $\pm\Delta\mathtt{CalDel}_{\mathtt{LR}}$. The similarity of figures 3.9a and 3.9b implies already, that there is no significant difference to be expected between shifting the LR scan to two different `WBC`s numerically and measuring them directly. In section 3.5 this difference will be investigated in detail.

Determination of θ_{abs} by `threshold.C`

The analysis of scans from 1 `WBC` and of scans from 3 `WBC`s is nearly the same. By default, both cases — the single `WBC` scan and the single `WBC` scan shifted numerically to 3 `WBC`s (triple) — are analyzed in the same run of `threshold.C`. The case with triple `WBC` is presented in the following, deviations for the single `WBC` case are mentioned.

In principle θ_{abs} is the overall lowest $\theta_{\texttt{CalDel}}$, that is determined for all `CalDel` values via SCurve fits as described in section 3.3.2. However, for the selection of the lowest value several aspects that are presented in the following paragraphs have to be considered:

- SCurve fits contribute by far the largest part to the calculation time. Therefore, to save time one wants to restrict `CalDel`, for which $\theta_{\texttt{CalDel}}$ is determined, to a reasonable range without excluding candidates for θ_{abs}.
- The problem of statistical fluctuations of different $\theta_{\texttt{CalDel}}$ is even more severe here than for the θ_{int} determination, as will be seen later.
- Outliers should be excluded.

Determination of a Reasonable `CalDel` Range

$\theta_{\texttt{CalDel}}$ is determined only for those lines of the LR scan, that have at least 4 bins in series with 100 % read out signals (so called good lines). This avoids SCurve fits not well defined and failing. The maximum of considered lines is 151 starting with the good line at the smallest `CalDel` value. In the single `WBC` case, further lines are far away from being candidates for θ_{abs}, while in the triple `WBC` scans further lines are exactly the same as previously considered ones.

Minimization of Statistical Fluctuations

To minimize statistical fluctuations, not the absolutely smallest $\theta_{\texttt{CalDel}}$ value is taken as θ_{abs}, but the smallest mean value of 17 $\theta_{\texttt{CalDel}}$ values from neighboring `CalDel` lines. In the single `WBC` case are considered 7 $\theta_{\texttt{CalDel}}$ values. The central of these 17 (7) $\theta_{\texttt{CalDel}}$ values is called $\theta^0_{\texttt{CalDel}}$.

Excluding Outliers — Getting θ_{abs}

To exclude outliers and to get θ_{abs}, all $\theta_{\texttt{CalDel}}$ values are filled in a histogram shown in figure 3.10a. The 17 $\theta^i_{\texttt{CalDel}}$ values, whose mean value is θ_{abs}, have to meet each of the following criteria:

1. $\chi^2/\mathrm{NDF} < 20$ for each SCurve fit leading to the $\theta^i_{\texttt{CalDel}}$ values. This criterion prevents from considering failed fits.
2. $\theta^0_{\texttt{CalDel}}$ has to lie in the flat region of figure 3.10a (flatness criterion):

$$3 > \left| \left(\frac{1}{17} \sum_{i=-8}^{8} \theta^i_{\texttt{CalDel}} \right) - \left(\frac{1}{17} \sum_{i=9}^{25} \theta^i_{\texttt{CalDel}} \right) \right| \tag{3.4}$$

   For the single `WBC` case, this criterion is much less sharp:

$$3 > \left| \left(\frac{1}{7} \sum_{i=-3}^{3} \theta^i_{\texttt{CalDel}} \right) - \left(\frac{1}{7} \sum_{i=4}^{11} \theta^i_{\texttt{CalDel}} \right) \right| \tag{3.5}$$

3. Outliers must not be included:

$$3 > \max_{-8\leq i\leq 8}\left(\theta^i_{\texttt{CalDel}}\right) - \min_{-8\leq i\leq 8}\left(\theta^i_{\texttt{CalDel}}\right) \tag{3.6}$$

For the single `WBC` case, this criterion is:

$$3 > \max_{-3\leq i\leq 3}\left(\theta^i_{\texttt{CalDel}}\right) - \min_{-3\leq i\leq 3}\left(\theta^i_{\texttt{CalDel}}\right) \tag{3.7}$$

If one criterion is not met for a $\theta^i_{\texttt{CalDel}}$, $\theta^i_{\texttt{CalDel}}$ must not belong to the range of the 17 $\theta_{\texttt{CalDel}}$ values considered for the θ_{abs} determination.

Error Determination of θ_{abs}

The error of θ_{abs} is supposed to be symmetric and is set to the RMS of the 17 (7) $\theta^i_{\texttt{CalDel}}$ values.

Other Methods of θ_{abs} Determination

Tests have been done varying the criteria described above as well as the quality criteria and cuts described in the following subsection. The presented ones have lead to the best results providing consistent θ_{abs} values with small errors, but excluding not too many measurements.

Other methods of θ_{abs} determination have been investigated as well. To mention is mainly the attempt to fit the upper curves of 50 % values in the LR and HR scans, where θ_{abs} could be determined as the divergence of the fit. (The determination of θ_{abs} as the `Vcal` value of the fit function at `CalDel` $= 0$ was excluded, as this `CalDel` value depends on the choice of the `WBC`). However, the function to fit the upper curves is not known. Different fit functions have been investigated — they lead to very different results. This is a systematic problem of this method, as θ_{abs} would be an extrapolated value that depends strongly on deviations of the fitted range. The method presented here in contrast does not need any extrapolation and produces much more reliable results.

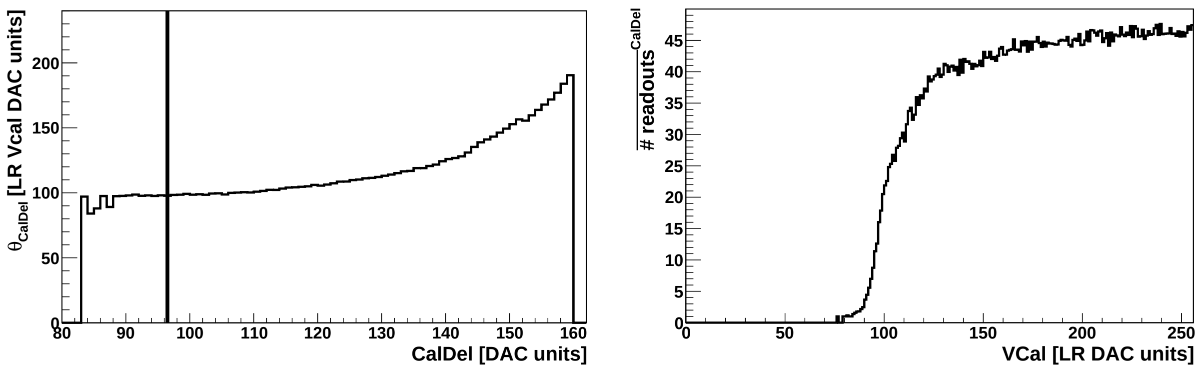

(a) (b)

Figure 3.10: Histogram of $\theta_{\texttt{CalDel}}$ values and LR scan projection to the `Vcal`-axis.
(a) The vertical line in this histogram of all considered $\theta_{\texttt{CalDel}}$ values indicates the $\theta_{\texttt{CalDel}}$ value finally chosen to be $\theta^0_{\texttt{CalDel}}$. The mean value of $\theta^{-8}_{\texttt{CalDel}} \ldots \theta^{8}_{\texttt{CalDel}}$ is θ_{abs}.
(b) This projection of the LR scan to the `Vcal`-axis is normalized to the number of bins with entries above 0.

3.3.4 Quality Criteria and Cuts

Cuts and quality criteria have been introduced at two different steps. Cuts on one hand lead to failure of the analysis of the measurement by `threshold.C` due to failure of essential parts of the analysis. Quality criteria on the other hand mark a measurement and print out warnings with the critical parameters that are out of the range of acceptance, but do not stop the analysis. Only when analyzing the resulting θ_{abs} and θ_{int} with `thranalyze.C`, these measurements are excluded. This distinction allowed appropriate adjustment of the criteria checking several plots that are produced by default for each measurement visually.

Cuts Causing Break of Analysis by `threshold.C`

Before θ_{abs} is determined by `threshold.C`, the LR scan is projected to the `Vcal`-axis, i.e. in a one-dimensional histogram every bin is filled with the sum of all bin contents of the scan for a fixed `Vcal`, divided by the number of bins with entries. Such a projection histogram is shown in figure 3.10b. Out of this histogram $\texttt{Vcal}_{\texttt{min}}$ and $\texttt{Vcal}_{\texttt{max}}$ are determined. $\texttt{Vcal}_{\texttt{min}}$ is the lowest `Vcal` value, for which $\mathrm{Proj}(\texttt{Vcal}) > 0.001$ is valid. $\texttt{Vcal}_{\texttt{max}}$ is smallest `Vcal`, for which $\mathrm{Proj}(\texttt{Vcal}) > 0.6$ holds.

The following cuts cause a break of the analysis of a measurement by `threshold.C`:

1. $\texttt{CalDel}_{\texttt{LA}}$, $\texttt{CalDel}_{\texttt{UA}}$, $\texttt{CalDel}_{\texttt{LL}}$ or $\texttt{CalDel}_{\texttt{UL}}$ are not found: As the determination of these values is very stable, this criterion triggered only when either the LR or the HR scan is out of the measurable `CalDel` range due to a badly chosen `WBC` value.
2. $\texttt{Vcal}_{\texttt{min}}$ or $\texttt{Vcal}_{\texttt{max}}$ are not found: This means, that the LR scan does not contain analyzable data, which is caused by a too low or too high threshold set or by running out of the `CalDel` range $0 \ldots 255$.
3. The `CalDel` range, within which $\theta_{\texttt{CalDel}}$ should be determined, is not found: This means, that there are no good lines for reliable SCurve fits.

The cuts number 1 and 3 rely on SCurve fits. They trigger, if χ^2/NDF of a SCurve fit is larger than 20 or if SCurve fits are not applied. This is the case if one of the following criteria is met:

- The one-dimensional histogram (basis for the SCurve fit) is empty.
- There are no 4 empty bins in series.
- There are no 4 bins of 100 % readout probability in series.

Quality Criteria that Cause Measurements Exclusion by `thranalyze.C`

The following criteria lead to the rejection of measurements by `thranalyze.C`:

1. $\Delta\texttt{CalDel}_{\texttt{HR}} < 40$ or $\Delta\texttt{CalDel}_{\texttt{LR}} < 40$ or $\Delta\texttt{CalDel}_{\texttt{HR}} > 70$ or $\Delta\texttt{CalDel}_{\texttt{LR}} > 70$: This criterion triggers, if upper/lower amplitudes or limits are found but unreliably low or high. This is usually the case, when the threshold is set too low resulting in scans with read out signals widely spread in `CalDel`.
2. $\frac{1}{3}\sum_{\texttt{Vcal}=253}^{255}\mathrm{Proj}(\texttt{Vcal}) < 30$: This criterion triggers, if the number of readouts at high `Vcal` rises not fast enough with rising `CalDel` to determine $\texttt{CalDel}_{\texttt{LA}}$ reliably.

3. Proj($\texttt{Vcal} = 0$) > 0: This means that the measurement is dominated by noise instead of calibration signal.
4. θ_{abs} is not found: This is the most critical triggering criterion observed quite often, particularly in single `WBC` scans. It means usually, that the flatness criterion triggers for all points of the curve seen in figure 3.10a, and that there is no flat region which would allow a reliable determination of θ_{abs}. This is exactly the reason, why the final analysis is done only with the three `WBC`s, for which the flatness criterion is much sharper but triggers less. Visual check of measurements with triggering flatness criterion for triple `WBC` has shown, that in these few cases $\Delta\texttt{CalDel}_{\texttt{LR}}$ has been determined badly, such that the scans from single `WBC`s overlap or there is a gap in between, leading to similar problems as in the single `WBC` case.
5. θ_{int} is not found: This has never been the case unless another quality criterion triggered as well.
6. $\theta_{int} < \theta_{abs}$: By definition θ_{int} has to be larger than θ_{abs}. Luckily this criterion never triggered if other criteria did not trigger as well.

3.4 Threshold Calibration

As described in section 2.3, `Vcthr` is the DAC parameter, which sets in the comparator the threshold on the signal from a particle hit as well as from calibration signals. The default `Vcthr` values currently used show a wide distribution among ROCs. In addition, the corresponding threshold in the physically relevant units of electrons for the same `Vcthr` value varies a lot among pixels. Therefore it is necessary to calibrate the threshold θ from `Vcthr` DAC units to electrons. Due to a lack of experimental access to measure directly the calibration `Vcthr` $\leftrightarrow$ electrons, this is done via `Vcal` calibration.

3.4.1 Calibration from `Vcthr` to `Vcal`

A measurement of the number of readouts vs. `Vcthr` and `Vcal` is shown in figure 3.11. It can be seen, that there is a sharp edge at $\texttt{Vcthr} = 127$, which is the threshold, for which noise becomes larger than the threshold and leads to entries independent of `Vcal`. The smaller the threshold is (the larger `Vcthr`), the more often buffer overflow occurs and the entries disappear. More interesting is the border at high thresholds: The curve connecting 50 % readout probability provides the threshold in LR `Vcal` units as a function of `Vcthr`. The determination of the function `Vcal(Vcthr)` by SCurve fits would lead to the calibration wanted. However, this curve would have to be measured for each I_{ana}, temperature and ROC separately. For the simulation, `Vcal(Vcthr)` has been determined this way for one set of parameters. However, for consistency and convenience another way of `Vcthr` $\leftrightarrow$ `Vcal` calibration out of the measured data has been chosen: The absolute threshold θ_{abs}, whose determination is described in the previous subsection, is just the threshold in LR `Vcal` units at the set `Vcthr`. Therefore, for the analysis

$$\theta[\text{LR } \texttt{Vcal} \text{ units}] = \theta_{abs} \tag{3.8}$$

has been used.

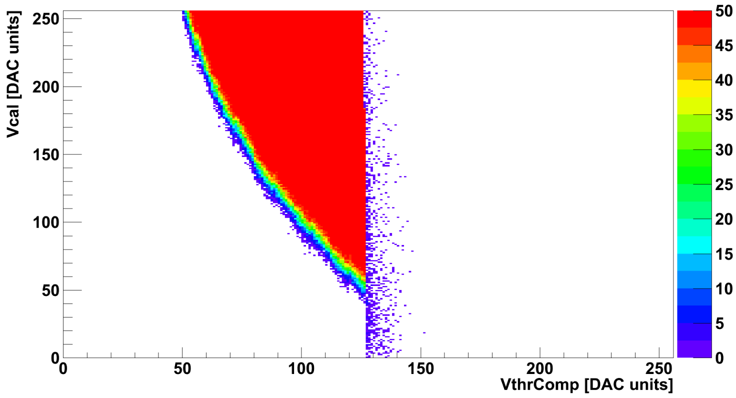

Figure 3.11: Measurement of the number of readouts vs. `Vcthr` and `Vcal`.
This calibration scan (ROC 3, pixel in column 5, row 5, taken at 17 °C) could be used for `Vcthr` to `Vcal` calibration and has been used for the simulation in chapter 5.

The problematics of temperature dependencies of the relation between the `Vcal` and `Vcthr` DAC units and their corresponding voltages (which are not examined in this study) are the same for both ways of calibration. In fact they use the same method — both determine the `Vcal` value corresponding to a distinct `Vcthr` value by SCurve fits of the number of readouts.

3.4.2 Calibration from `Vcal` to Electrons

In first approximation, 1 LR `Vcal` unit corresponds to 65 electrons. A more accurate pixel by pixel calibration has been done with X-rays at room temperature (see [15] for details). Temperature effects are in the order of $0.4\,\frac{\%}{^\circ\mathrm{C}}$, which have not been corrected here as calibration data exist for room temperature only. Therefore, a systematic error of the threshold in the order of 10 % might be introduced here. As will be seen in the following chapter, this is still negligible compared to the ROC to ROC variation.

Two calibration points of molybdenum and silver have been used for the X-ray calibration: A photon of the molybdenum line (17.44 keV) produces $E^{Mo} = 4\,844$ electron-hole pairs, a photon of the silver line (22.10 keV) produces $E^{Ag} = 6\,139$ pairs. The `Vcal` values $\mathtt{Vcal}^{Mo}$ and $\mathtt{Vcal}^{Ag}$ leading to the same output of electrons have been determined for each pixel. Assuming a linear correlation between `Vcal` and the number of electrons, this provided a 2×2 system of equations:

$$E^{Mo} = m \cdot \mathtt{V}^{Mo}_{\mathtt{cal}} + q \tag{3.9}$$

$$E^{Ag} = m \cdot \mathtt{V}^{Ag}_{\mathtt{cal}} + q \tag{3.10}$$

This system was solved to get m and q for each analyzed pixel, which provided the calibration from arbitrary LR `Vcal` values to the corresponding number of electrons E:

$$\mathtt{Vcal}[\text{electrons}] = E = m \cdot \mathtt{Vcal}[\text{DAC units}] + q \tag{3.11}$$

Due to the offset q, the calibrations of θ_{int}, θ_{abs} or θ to electrons have to be done separately (or only the slope m is considered), the direct calibration of $\Delta\theta[\mathtt{Vcal}\text{ units}] \rightarrow \Delta\theta[\text{electrons}]$ with equation (3.11) leads to a wrong result.

3.5 Methodical Checks

It is clear from the definition of θ_{abs}, that the determination of θ_{abs} out of 3 added LR scans from different `WBC`s (see subsection 3.3.3) leads to a more accurate result than the determination of θ_{abs} out of the LR scan of just one `WBC`. The error introduced in this case is investigated in subsection 3.5.1. As it requires twice as many scans to determine θ_{abs} out of 3 merged LR scans from different `WBC`s, it is examined in subsection 3.5.2 for a subset of possible parameters, if this effort is necessary or if the gained improvement compared to three numerically shifted scans is negligible.

3.5.1 Comparison of $\Delta\theta^{\mathtt{1WBC}}_{\mathbf{meas}}$ with $\Delta\theta^{\mathtt{3WBC}}_{\mathbf{meas}}$

LR and HR scans have been taken for all ROCs with $I_{ana} = 24\,\mathrm{mA}$ and the `WBC`s 98, 99 (the standard `WBC` for $I_{ana} = 24\,\mathrm{mA}$) and 100 in the whole range of thresholds that leads to analyzable results (`Vcthr` $= 30 \ldots 150$ DAC units with step size 10). By the algorithm described in subsection 3.3.3, $\Delta\theta = \theta_{int} - \theta_{abs}$ has been determined for triple `WBC` (considering the scans of all 3 measured `WBC`s) and for single `WBC` (considering only the scan with `WBC` $= 99$). The results have been plotted as a function of θ for all ROCs.

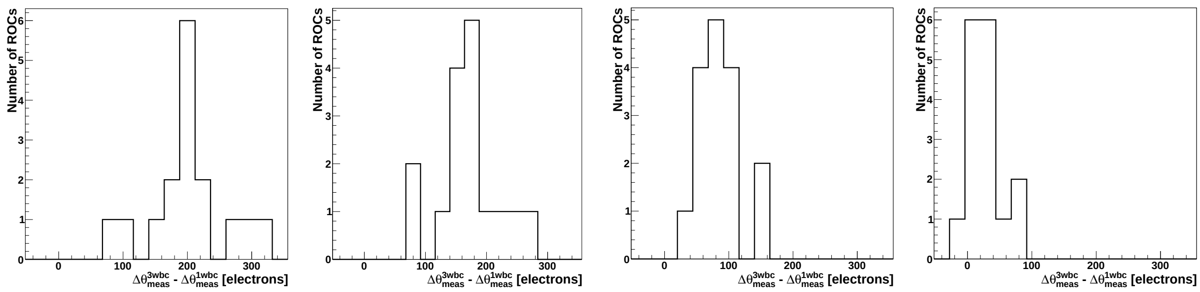

(a) $\theta = 2\,000$ electrons Mean: 202 ± 60 el.
(b) $\theta = 3\,000$ electrons Mean: 168 ± 50 el.
(c) $\theta = 6\,000$ electrons Mean: 85 ± 33 el.
(d) $\theta = 10\,000$ electrons Mean: 25 ± 25 el.

Figure 3.12: Distribution of $\Delta\theta^{\mathtt{3WBC}}_{\mathbf{meas}} - \Delta\theta^{\mathtt{1WBC}}_{\mathbf{meas}}$ at 4 distinct thresholds.

Due to the different θ_{abs} and with it different calibration of the threshold in `Vcthr` DAC units into electrons, $\Delta\theta(\theta)$ of triple `WBC` ($\Delta\theta^{\mathtt{3WBC}}_{\mathrm{meas}}$) and of single `WBC` ($\Delta\theta^{\mathtt{1WBC}}_{\mathrm{meas}}$) are not directly comparable. Therefore a polynomial fit of 2^{nd} degree has been applied to the graph of $\Delta\theta$ vs. θ for each ROC. These fits are shown together with the measured points $(\theta, \Delta\theta)$ on the pages 71 to 73 in the appendix. Next, the fitted $\Delta\theta$ have been evaluated at 20 fixed thresholds between 0 and 19 000 electrons. This allowed to determine the difference between $\Delta\theta^{\mathtt{3WBC}}_{\mathrm{meas}}$ and $\Delta\theta^{\mathtt{1WBC}}_{\mathrm{meas}}$ at the distinct thresholds for all ROCs. For each threshold this difference has been filled into histograms (16 entries each from 16 ROCs) to determine their mean value and distribution among ROCs. Four such histograms are shown in figures 3.12. The mean values and RMS (providing the error) of all thresholds are plotted vs. the threshold in figure 3.13a.

It can be seen clearly, that mainly for low θ (the aimed range is about $2\,000 \ldots 4\,000$ electrons) $\Delta\theta^{\mathtt{1WBC}}_{\mathrm{meas}}$ differs a lot from $\Delta\theta^{\mathtt{3WBC}}_{\mathrm{meas}}$. This matches the expectations, since for low θ (see figure 3.8b) the entries at the lowest `Vcal` show no vertical line in the single `WBC` LR scan as it is the case for high thresholds (see figure 3.8a). Due to the failure of SCurve fits at very low `CalDel` values, where the number of readouts never reaches 100 %, θ_{abs} is found at too high `Vcal` for low thresholds, i.e. $\Delta\theta$ is found too small. The fact, that the flatness criterion triggers more often in this range also indicates that.

The rising difference for thresholds above 12 000 electrons is due to statistical effects and the fit algorithm: In this range not all ROCs provide analyzable data, for these $\Delta\theta^{\mathtt{1WBC}}_{\mathrm{meas}}$ and $\Delta\theta^{\mathtt{3WBC}}_{\mathrm{meas}}$ are based on extrapolations of the polynomial fits. However, this can not fully explain the rising part of these ROCs. Manual check of control plots automatically generated during the analysis by `threshold.C` show, that due to statistical fluctuations slightly smaller θ_{abs} are found in the scans with the `WBC` values 98 and 100 than in the scans with `WBC` = 99. The consideration of all ROCs at high thresholds shows no systematic shift of θ_{abs} between scans with different `WBC`.

From figure 3.13a it can be seen further, that the systematic error introduced if $\Delta\theta$ is determined as $\Delta\theta^{\mathtt{1WBC}}_{\mathrm{meas}}$ instead of $\Delta\theta^{\mathtt{3WBC}}_{\mathrm{meas}}$ can be in the order of 200 electrons for low θ, which corresponds to about 3 LR `Vcal` DAC units. Therefore $\Delta\theta$ should always be determined from several `WBC`s. The consideration of more than 3 `WBC`s leads to no further improvement, as the LR scan is spread over no more `CalDel` values corresponding to 3 `WBC`s.

$\Delta\theta$ has been determined also with the LR scans of 2 different `WBC` values ($\Delta\theta^{\mathtt{2WBC}}_{\mathrm{meas}}$). The comparison with $\Delta\theta^{\mathtt{3WBC}}_{\mathrm{meas}}$ shows, that $\Delta\theta^{\mathtt{2WBC}}_{\mathrm{meas}}$ is slightly lower for high thresholds, but within the errors of $\Delta\theta^{\mathtt{3WBC}}_{\mathrm{meas}}$. The reasons are the same as for the difference between $\Delta\theta^{\mathtt{3WBC}}_{\mathrm{meas}}$ and $\Delta\theta^{\mathtt{1WBC}}_{\mathrm{meas}}$ for high thresholds. For low thresholds $\Delta\theta^{\mathtt{3WBC}}_{\mathrm{meas}} - \Delta\theta^{\mathtt{2WBC}}_{\mathrm{meas}}$ is larger. This is expected, as a single `WBC` scan does not fit into the `CalDel` range covering 2 `WBC`s, which means a 3$^{\mathrm{rd}}$ `WBC` will add entries to both other `WBC`s measured.

As a conclusion it is recommended to use always measurements with LR scans of 3 `WBC`s.

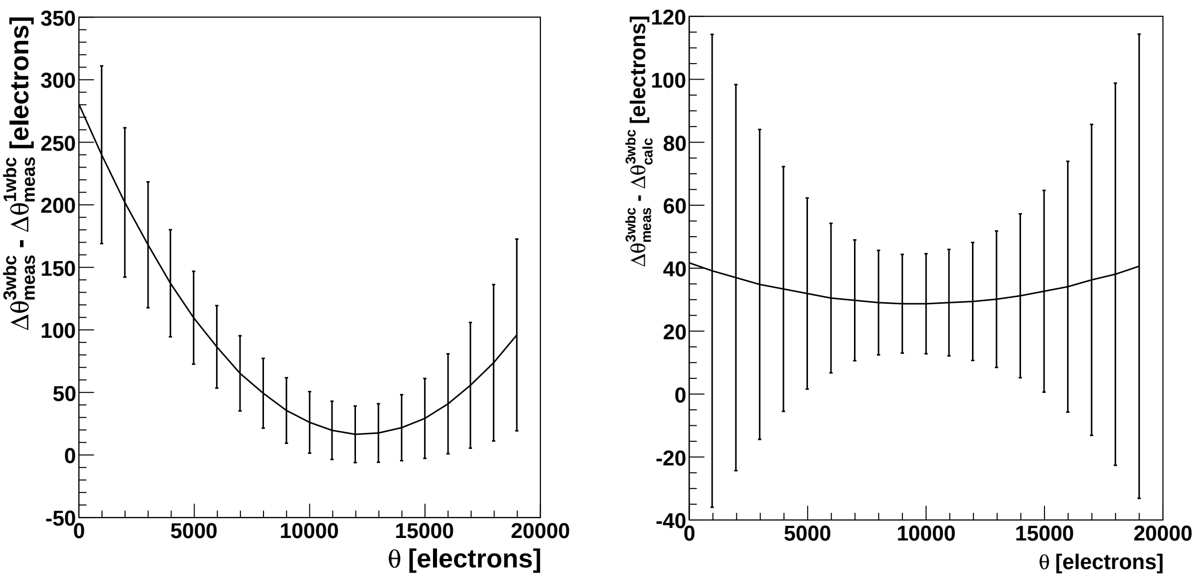

(a) (b)

Figure 3.13: Comparison of $\Delta\theta^{\mathtt{3WBC}}_{\mathrm{meas}}$ with $\Delta\theta^{\mathtt{1WBC}}_{\mathrm{meas}}$ (a) and with $\Delta\theta^{\mathtt{3WBC}}_{\mathrm{calc}}$ (b).
The points show $\Delta\theta^{\mathtt{3WBC}}_{\mathrm{meas}} - \Delta\theta^{\mathtt{1WBC}}_{\mathrm{meas}}$ (a) and $\Delta\theta^{\mathtt{3WBC}}_{\mathrm{meas}} - \Delta\theta^{\mathtt{3WBC}}_{\mathrm{calc}}$ (b) evaluated at 20 distinct thresholds with the distribution among ROCs shown as error bars.

3.5.2 Comparison of $\Delta\theta^{\texttt{3WBC}}_{\text{calc}}$ with $\Delta\theta^{\texttt{3WBC}}_{\text{meas}}$

To avoid taking the LR scans in 3 different `WBC`s, the scans of `WBC` = 99 have been shifted numerically along the `CalDel` axis, simulating scans of other `WBC`s (see section 3.3.3). It has been checked, if the resulting $\Delta\theta$ of 3 such numerically shifted and merged scans ($\Delta\theta^{\texttt{3WBC}}_{\text{calc}}$) differs from $\Delta\theta$ determined from 3 scans effectively measured with different `WBC` values ($\Delta\theta^{\texttt{3WBC}}_{\text{meas}}$). This analysis has been realized exactly the same way as the analysis in subsection 3.5.1. The data points $\Delta\theta^{\texttt{3WBC}}_{\text{calc}}(\theta)$ are shown on pages 71 to 73 with a 2^{nd} degree polynomial fit applied. From these fits $\Delta\theta^{\texttt{3WBC}}_{\text{meas}} - \Delta\theta^{\texttt{3WBC}}_{\text{calc}}$ has been determined for 20 distinct thresholds in the range $0 \ldots 19\,000$ electrons. The distributions of $\Delta\theta^{\texttt{3WBC}}_{\text{meas}} - \Delta\theta^{\texttt{3WBC}}_{\text{calc}}$ among ROCs are shown in figures 3.14 for the same 4 thresholds as in the previous subsection.

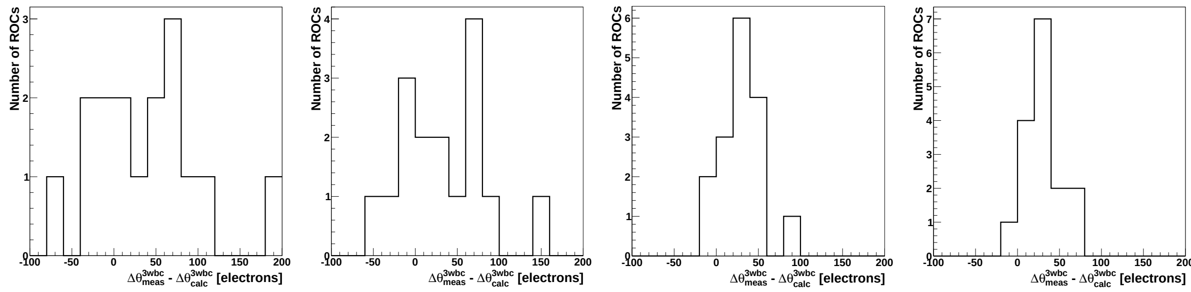

(a) $\theta = 2\,000$ electrons
Mean: 37 ± 61 el.

(b) $\theta = 3\,000$ electrons
Mean: 35 ± 50 el.

(c) $\theta = 6\,000$ electrons
Mean: 30 ± 24 el.

(d) $\theta = 10\,000$ electrons
Mean: 29 ± 16 el.

Figure 3.14: Distribution of $\Delta\theta^{\texttt{3WBC}}_{\text{meas}} - \Delta\theta^{\texttt{3WBC}}_{\text{calc}}$ at 4 distinct thresholds.

In figure 3.13b the mean values of these distributions are plotted together with the RMS as a function of the threshold. It can be seen, that the mean systematic error introduced considering $\Delta\theta^{\texttt{3WBC}}_{\text{calc}}$ instead of $\Delta\theta^{\texttt{3WBC}}_{\text{meas}}$ lies between 30 and 40 electrons or about half a LR `Vcal` DAC unit and does not depend strongly on the threshold. It is by far lower than considering $\Delta\theta^{\texttt{1WBC}}_{\text{meas}}$ instead of $\Delta\theta^{\texttt{3WBC}}_{\text{meas}}$. For these reasons, it seems acceptable to use $\Delta\theta^{\texttt{3WBC}}_{\text{calc}}$ instead of $\Delta\theta^{\texttt{3WBC}}_{\text{meas}}$ for $\Delta\theta$ and it is used

$$\Delta\theta \equiv \Delta\theta^{\texttt{3WBC}}_{\text{calc}} \tag{3.12}$$

for all analysis presented further. Although all analysis has been done in parallel for the single `WBC` case ($\Delta\theta^{\texttt{1WBC}}_{\text{meas}}$), these results are not presented here as they show the same effects as $\Delta\theta^{\texttt{3WBC}}_{\text{calc}}$ but with a larger systematic error.

3.6 Reproducibility Check

For all ROCs one measurement of $\Delta\theta$ has been repeated 16 times to check the reproducibility of single measurements. The set of parameters was therefore always the same: $T = 17\,°\text{C}$, $I_{ana} = 24\,\text{mA}$, `Vcthr` $= 60$, `WBC` $= 99$. The resulting $\Delta\theta$ are shown in figure 3.15.

The measurements $1 \ldots 14$ have been done right after each other i.e. with about 25 minutes difference in time. This is twice the time, a HR or LR scan takes. Scans of different ROCs of the same measurement have always been taken within a few minutes.

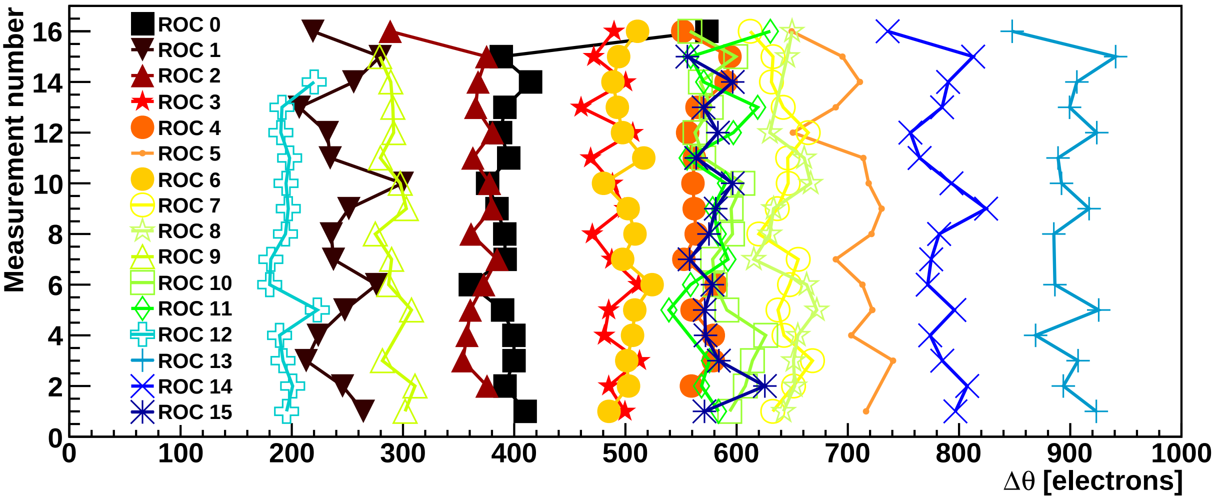

Figure 3.15: Reproducibility check of $\Delta\theta$ with 16 measurements for 16 ROCs. Errors are not drawn for clarity.

The measurement 15 has been done some days before, but still with the HR and LR scans taken right after each other. Between the measurements 15 and 1, other measurements have been done and the cooling box was switched off (the module has warmed up). For the measurements $1 \ldots 14$ the DAC-files from the measurement 15 have been reloaded, i.e. PreTest runs taken in between and changes of the parameter settings had no effect. Therefore one does not expect a different behavior of the measurements $1 \ldots 14$ and 15. This is confirmed by the measurements.

In contrast, the measurement 16 produces some outliers. It has been taken as the first measurement of this series several days before the measurement 15 with a separate PreTest calibration. This lead to slightly different DAC parameters (namely `Vana`) compared to the measurements $1 \ldots 15$. However, what lead to the difference in $\Delta\theta$ might be rather the fact, that between the LR and HR scans a few days passed. This could have led for instance to a small shift in the correspondence of `CalDel` DAC units to time and with it to an error in θ_{int}. Therefore the measurement 16 has been excluded from the further analysis. Consequences for the reliability of the results presented in the following sections and chapters are not to be expected: LR and HR scans have always been taken right after each other except for the measurements of all pixels of a ROC in the following two sections, where it was not possible. However, absolute values of $\Delta\theta$ are of minor importance there.

Missing points in figure 3.15 indicate measurements that failed the analysis. In most cases, the flatness criterion (see section 3.3.4) triggered for these measurements, which is not a hint for bad data but for the difficulty to standardize the analysis with a minimal error and minimal exclusion of measurements at the same time.

The variation of $\Delta\theta$ among different measurements is in the order of 15 electrons, which is about a fourth of the error of a single measurement (see next page). This indicates, that the errors of single measurements as they are determined by `threshold.C` are rather high.

The lines of different ROCs are mostly separated — this means, that the error of single $\Delta\theta$ measurements is by far lower than the ROC to ROC variation. The distributions of $\Delta\theta$ from all measurements are shown for each ROC in the figures on pages 74 to 75.

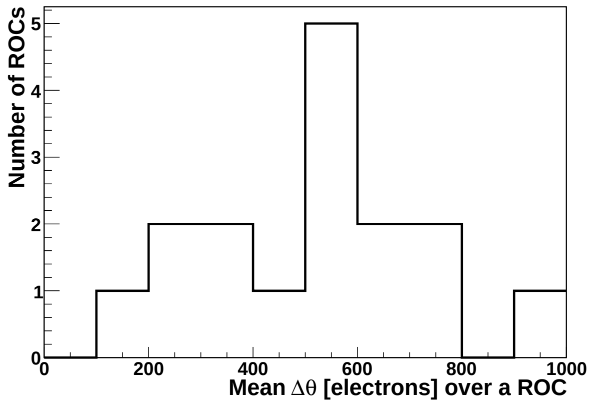

(a) Mean: 531 ± 189 electrons

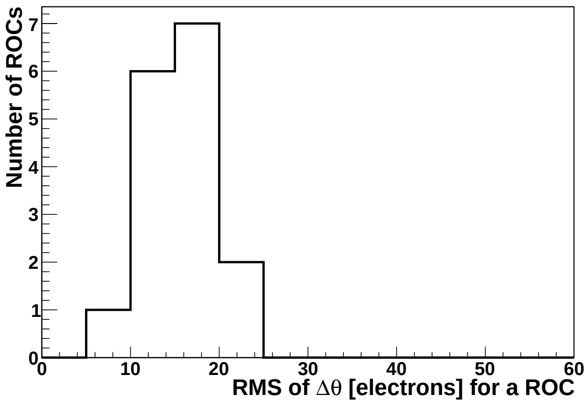

(b) Mean: 15.6 ± 4.2 electrons

Figure 3.16: Distribution of $\overline{\Delta\theta}^{meas}$ and of the RMS of $\Delta\theta$.
(a) Distribution of $\Delta\theta$ averaged over 15 measurements of a ROC
(b) Distribution of the RMS from 15 measurements of a ROC

The mean value of the 15 $\Delta\theta$ values of a ROC as well as the RMS of the measurements have been filled in histograms (the measurement 16 has been excluded). They are shown in figures 3.16a and 3.16b, respectively. It can be seen, that the mean values of different ROCs are with a RMS of 179 electrons widely distributed, while the reproducibility of single measurements is with a mean RMS of 15.6 electrons well acceptable.

To compare the variation of measurements for different ROCs, the $\Delta\theta$ values of single measurements have been shifted by the mean $\Delta\theta$ of a ROC. The resulting 0-centered distribution of the shifted $\Delta\theta$ of all ROCs is shown in figure 3.17a. The RMS of this distribution (16 electrons) is as expected about the same as the mean value of the distribution of figure 3.16b. The distribution of errors of $\Delta\theta$ (determined by `threshold.C` from the single measurements) is plotted in figure 3.17b (mean: 47, RMS: 16 electrons).

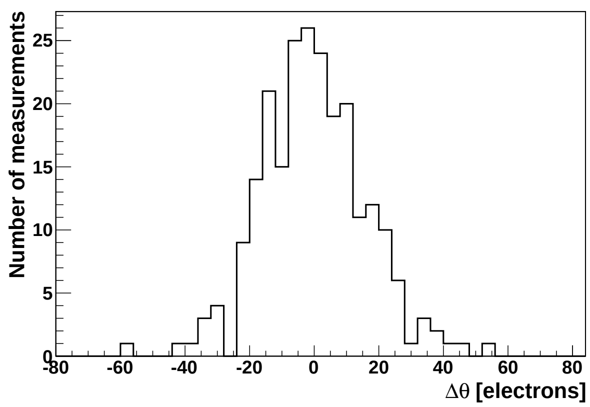

(a) Mean: 0 ± 16 electrons

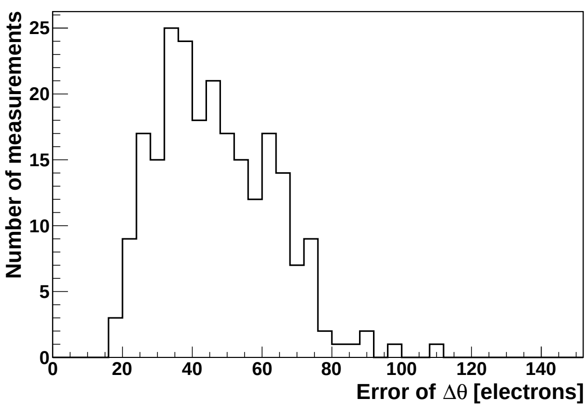

(b) Mean: 47 ± 16 electrons

Figure 3.17: $\Delta\theta - \overline{\Delta\theta}^{meas}$ and error distribution.
(a) Distribution of $\Delta\theta$ for 15 measurements per ROC, shifted by the mean $\Delta\theta$ of a ROC.
(b) Error of $\Delta\theta$ for 15 measurements and 16 ROCs determined by `threshold.C`.

3.7 Time Corresponding to 1 `CalDel` Unit

HR and LR scans have been taken for all pixels of ROC 0 for the same set of parameters that had been used for the reproducibility check presented in the previous section ($T = 17\,°\text{C}$, $I_{ana} = 24\,\text{mA}$, $\texttt{Vcthr} = 60$, $\texttt{WBC} = 99$). The time that corresponds to 1 `CalDel` unit has been determined as $\frac{25\,\text{ns}}{\Delta\texttt{CalDel}_{\texttt{HR}}}$ from these HR scans and as $\frac{25\,\text{ns}}{\Delta\texttt{CalDel}_{\texttt{LR}}}$ from the LR scans based on

$$25\,\text{ns} = \text{time of 1 bunch crossing} \mathrel{\hat{=}} 1\,\texttt{WBC}\ \text{DAC unit} \mathrel{\hat{=}} \Delta\texttt{CalDel}. \tag{3.13}$$

For the definition and determination of $\Delta\texttt{CalDel}_{\texttt{HR}}$ and $\Delta\texttt{CalDel}_{\texttt{LR}}$ see subsection 3.3.3. Histograms of $\frac{25\,\text{ns}}{\Delta\texttt{CalDel}_{\texttt{HR}}}$ and $\frac{25\,\text{ns}}{\Delta\texttt{CalDel}_{\texttt{LR}}}$ can be seen in figures 3.18. The number of entries (3988) is smaller than the number of pixels (4160), as only measurements that match the quality criteria of the $\Delta\theta$ determination have been considered (see sections 3.3.4 for the criteria and 3.8 for a discussion of the measurements). The mean values and RMS are listed in table 3.1.

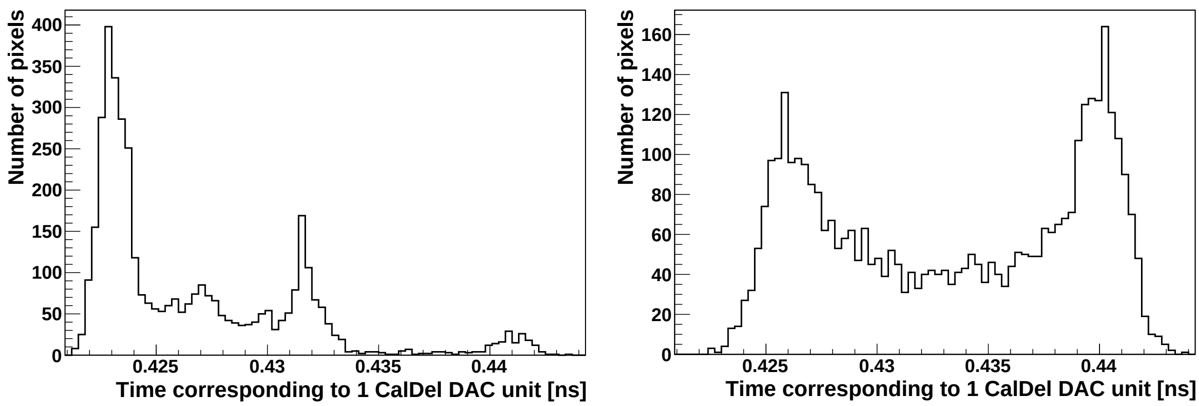

(a) Determined from HR scans. **(b)** Determined from LR scans.

Figure 3.18: Time corresponding to 1 `CalDel` unit.

The RMS is small, and the two mean values are compatible with each other and with the expected value of roughly 0.45 ns [13]. This confirms, that the chosen method to determine the number of `CalDel` units corresponding to 25 ns is appropriate for shifting histograms as done in the analysis. The correspondence *CalDelay* $\leftrightarrow$ `CalDel` of equation (2.4) has been determined from the mean value of the HR scans in table 3.1. It might be used also for other type of calibration, where the time correspondence of `CalDel` is needed.

Table 3.1: Mean time corresponding to 1 `CalDel` unit.

	Mean $\frac{\Delta t}{\Delta\texttt{CalDel}}$ [ns]	RMS [ns]
HR scan:	0.4265	0.0046
LR scan:	0.4334	0.0059

Naively one would expect a gaussian distribution of $\frac{\Delta t}{\Delta\texttt{CalDel}}$ for the two histograms of figure 3.18. Obviously this is not the case and one can see several peaks. They are a feature of the constraint of `CalDel` to integers: If no SCurve fit would be applied to find $\texttt{CalDel}_{\texttt{UA}}$, $\texttt{CalDel}_{\texttt{LA}}$, $\texttt{CalDel}_{\texttt{UL}}$ and

$\texttt{CalDel}_{\texttt{LL}}$, $\Delta\texttt{CalDel}_{\texttt{HR}}$ and $\Delta\texttt{CalDel}_{\texttt{LR}}$ would be constrained to integers of $\Delta\texttt{CalDel} \approx 55\ldots60$. Only the SCurve fits smear out (and determine more precisely) these integers and add peaks at half-integers, when an upper *or* lower `CalDel` value is an integer. This can explain also, why only two peaks can be seen in the LR histogram, while rather 4 peaks are visible in the HR histogram: In LR scans the SCurve rises over many more different `CalDel` values than in HR scans, which leads to a stronger smearing. The table 3.2 shows the peaks and their probable correspondence to (half-)integers of Δ`CalDel`. The expected peaks have been calculated as $\frac{25\,\mathrm{ns}}{\Delta\texttt{CalDel}}$.

Table 3.2: Time corresponding to 1 `CalDel` unit: peaks corresponding to Δ`CalDel`.

Δ`CalDel`:	59	58.5	58	57.5	57	56.5
Expected peak $[\frac{\mathrm{ns}}{\mathrm{DAC}}]$:	0.424	0.427	0.431	0.435	0.439	0.442
Visible peak HR $[\frac{\mathrm{ns}}{\mathrm{DAC}}]$:	0.423	0.427	0.432	–	–	0.441
Visible peak LR $[\frac{\mathrm{ns}}{\mathrm{DAC}}]$:	–	0.426	–	–	–	0.440

3.8 Distribution of $\Delta\theta$ over a ROC

Based on the same scans that had been used to determine the time corresponding to one `CalDel` DAC unit in the previous section, $\Delta\theta$ has been determined for all pixels of the ROC 0 at `Vcthr` $= 60$ and $I_{ana} = 24\,\mathrm{mA}$ to check the distribution of $\Delta\theta$ over a ROC. Due to their different calibrations from `Vcthr` to electrons, the results of different pixels are not directly comparable. Therefore $\Delta\theta$ (after calibration to electrons) has been normalized to the threshold (also calibrated to electrons). A histogram with the distribution of the normalized $\Delta\theta$ is shown in figure 3.19a. This gives an estimate of the pixel to pixel variation within a ROC.

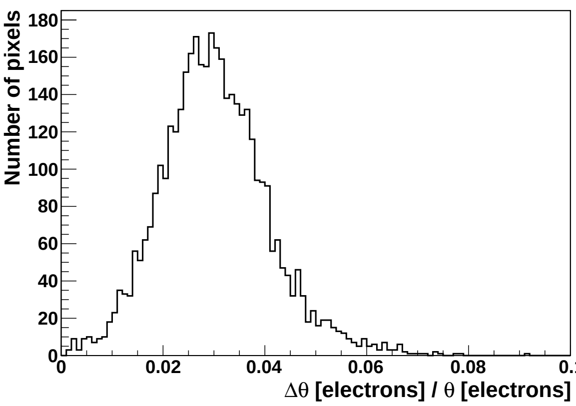

(a) Mean: 0.030 ± 0.011

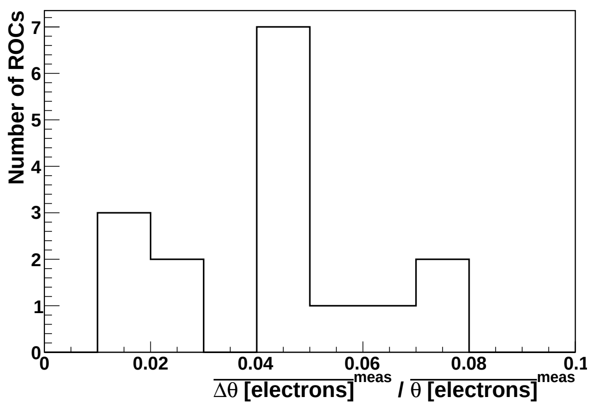

(b) Mean: 0.047 ± 0.018

Figure 3.19: Pixel to pixel and ROC to ROC variation of $\Delta\theta$.
(a) $\frac{\Delta\theta}{\theta}$ for all Pixels of ROC 0 after separate calibration of $\Delta\theta$ and θ to electrons.
(b) Based on the measurements of the reproducibility check: For the pixel in column 5, row 5 of all 16 ROCs has been divided the mean $\Delta\theta$ from 15 measurements by the mean of the corresponding threshold. Before their mean values have been taken, $\Delta\theta$ and θ have been calibrated to electrons.

For the comparison of the pixel to pixel with the ROC to ROC variation of $\Delta\theta$, the results of the reproducibility check (see section 3.6) have been normalized to the threshold also. Figure 3.19b shows the histogram with $\overline{\Delta\theta}^{15\text{meas}}[\text{electrons}]/\overline{\theta}^{15\text{meas}}[\text{electrons}]$ of 16 ROCs, where $\overline{\Delta\theta}^{15\text{meas}}[\text{electrons}]$ is the mean value of $\Delta\theta$ from the first 15 measurements of the reproducibility check and $\overline{\theta}^{15\text{meas}}[\text{electrons}]$ the mean threshold of these measurements. $\Delta\theta$ and θ of each measurement have been calibrated to electrons before their mean values have been taken.

Although the statistics is too low for an appropriate comparison, it can be seen, that the ROC to ROC variation is at least of the same order of magnitude as the pixel to pixel variation; probably it is larger.

Figure 3.20 shows a two-dimensional histogram with the bin content $\frac{\Delta\theta[electrons]}{\theta[electrons]}$ at the pixel position within the ROC. Not only at the borders, where pixels are larger and a different threshold behavior is expected, but also horizontally are patterns visible. Such patterns are known from other measurements, but it is not completely clear, what their origin is. An experimental feature can not completely be excluded here: The measurements of the whole ROC have been done in horizontal blocks of the rows $0\ldots1$, $2\ldots9$, $10\ldots40$, $41\ldots70$ and $71\ldots79$. All these measurements together took 4 days, and even LR/HR measurements of the same block had to be done on different days. This had a negative impact on the accuracy and could lead to failure of the analysis (triggering of the flatness criterion, see section 3.6). Such pixels are drawn white in figure 3.20. There are no dead pixels on that ROC, which was checked every day that measurements have been taken by a so called PixelAlive scan. However, if the measurement in blocks was the origin of the pattern, one would rather expect vertical pattern with differences between measured blocks than horizontal structures.

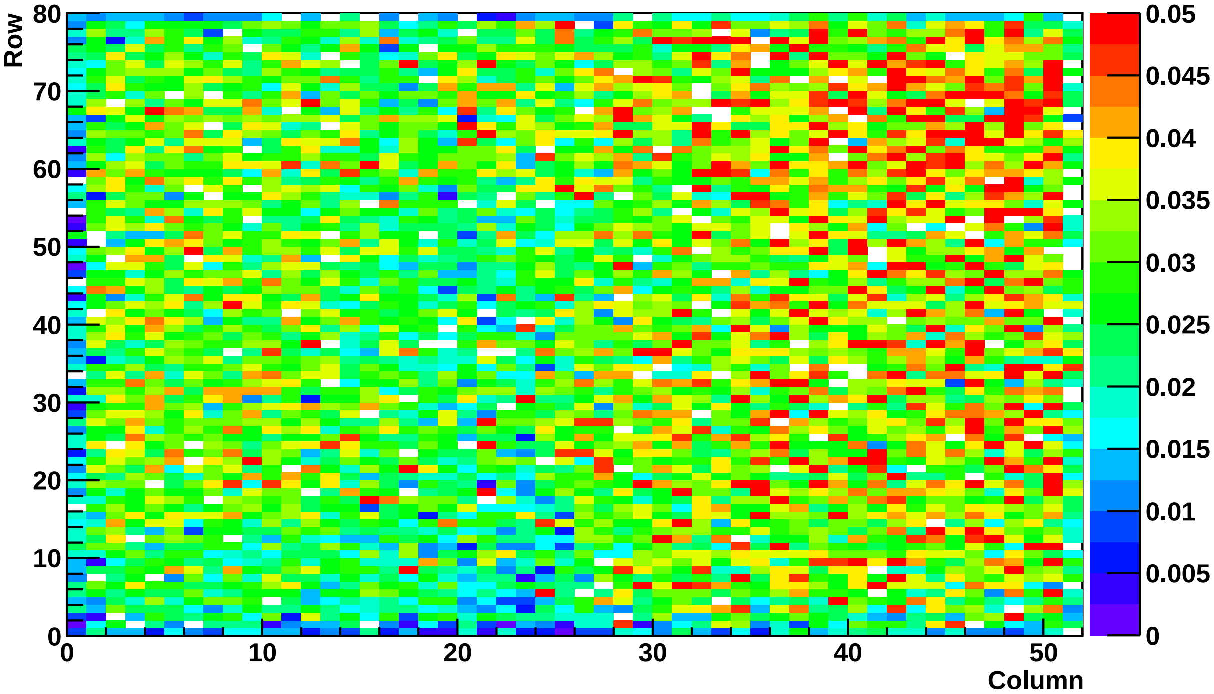

Figure 3.20: Pixel map with $\frac{\Delta\theta[electrons]}{\theta[electrons]}$ for all Pixels of ROC 0.
For white pixels, the analysis has failed. The maximum bin content has been artificially moved from 0.091 to 0.05 to make visible the wide range and patterns throughout the ROC.

4 Results

All measurements presented in this chapter have been taken for the pixel in column 5, row 5 for all 16 ROCs of the module M0090. HR and LR scans of the number of readouts have been taken as a function of `Vcal` and `CalDel` with the following parameters:

- Temperature: The temperature in the cooling box was set to 17 and $-10\,°C$. However, the effectively measured temperature was $15.8 \pm 0.2\,°C$ as a feature of the cooling box when it was set to $17\,°C$. The reason might be aging of the peltier element. When the temperature was set to $-10\,°C$, the expected temperature of $-10.00 \pm 0.05\,°C$ was measured.
- I_{ana}: The analog current was set to 16, 20, 24, 28 and 32 mA.
- `WBC`: The chosen `WBC` value depends on I_{ana}. It was set `WBC` $= 99$ by default and `WBC` $= 98$ for $I_{ana} = 20\,mA$. However, the choice of `WBC` is supposed to be irrelevant for this analysis as long as the scans match the `CalDel` range.
- `Vcthr`: The threshold was set in the range $0 \ldots 170$ (10 `Vcthr` DAC units step size), where analyzable results could be obtained. The actual range varies and depends on the ROC and on I_{ana}. It is slightly enlarged toward higher `Vcthr` (lower θ) for higher I_{ana} and is typically `Vcthr` $\approx 30 \ldots 110$ for $I_{ana} = 16\,mA$ and `Vcthr` $\approx 40 \ldots 150$ for $I_{ana} = 32\,mA$ corresponding to thresholds of about $19\,000 \ldots 2\,000$ electrons. Depending on the ROC, this provides about 7 points of $\Delta\theta(\theta)$ for $I_{ana} = 16\,mA$ and about 10 points for $I_{ana} = 32\,mA$.

$\Delta\theta$ has been determined from these measurements and calibrated to electrons as described in the previous chapter. For $T = 17$ and $-10\,°C$ separate parameterizations of $\Delta\theta$ as a function of θ and I_{ana} have been determined. They are presented together with the results of the measurements in sections 4.1 and 4.2, respectively. A comparison of the results from the measurements at different temperatures is given in section 4.3.

4.1 $\Delta\theta$ as a Function of θ and I_{ana} at $T = 17\,°C$

4.1.1 Measurements of $\Delta\theta(\theta,\ I_{ana})$

Figure 4.1 shows $\Delta\theta$ as a function of θ and I_{ana} determined from the measurements for the ROC 11 as an example. The corresponding figures for all ROCs are shown in the appendix on pages 76 to 78. The lines are a two-dimensional polynomial fit of 2^{nd} degree that is explained in the next subsection. As in all figures of this chapter, errors of θ are drawn too, but covered by the data point. In absolute values, the errors of θ are about $80 \ldots 90\,\%$ of the errors of $\Delta\theta$. Due to the larger scale of θ, they are not visible.

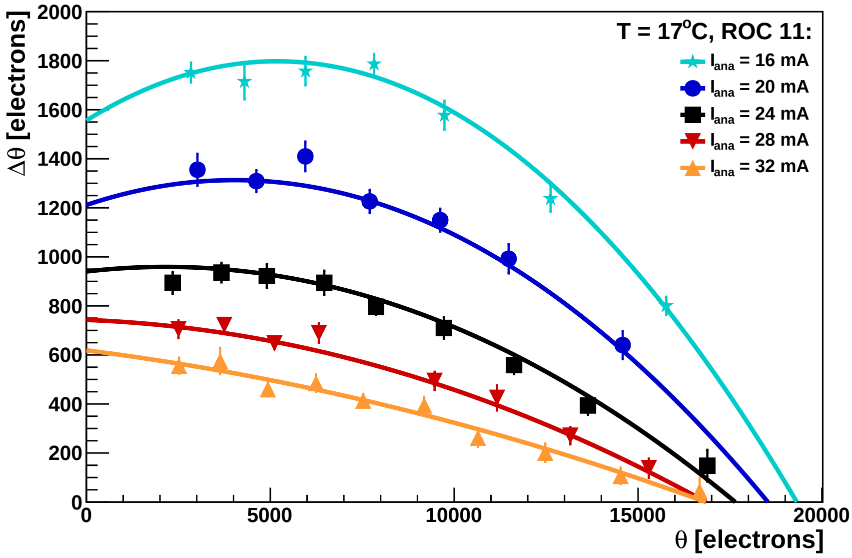

Figure 4.1: $\Delta\theta$ as a function of θ and I_{ana} at $T = 17°\mathrm{C}$ for the ROC 11 as an example. The lines are a two-dimensional polynomial fit of 2^{nd} degree.

Obviously $\Delta\theta$ depends strongly on the threshold θ and on I_{ana}. The fact, that for low I_{ana} a larger $\Delta\theta$ is measured than for high I_{ana} matches the expectations. This is not the case for the dependency of $\Delta\theta$ on θ. Naïvely, one would expect a positive slope of $\Delta\theta(\theta)$, which is measured only for some ROCs for low I_{ana} and low thresholds. The expectations and reasons for the measured dependencies of $\Delta\theta$ are discussed with the simulations in chapter 5.

4.1.2 Parameterization of $\Delta\theta(\theta, I_{ana})$: Parameters α, β, γ and A, B, C

The threshold calibration from `Vcthr` DAC units to electrons (see section 3.4) is different for each measurement. Therefore it is not possible to compare measurements from different ROCs directly with each other — although they have been measured with the same `Vcthr` and I_{ana}, the thresholds corresponding to `Vcthr` are different. Only fitted functions $\Delta\theta(\theta)$ evaluated at the same θ allow a comparison among ROCs.

For each ROC, a two-dimensional graph has been drawn showing all measured points $\Delta\theta(\theta, I_{ana})$. To parameterize the dependency of $\Delta\theta$ on θ and on I_{ana}, a two-dimensional polynomial fit of 2^{nd} has been calculated:

$$\Delta\theta(\theta, I_{ana}) = \alpha(I_{ana}) \cdot \theta^2 + \beta(I_{ana}) \cdot \theta + \gamma(I_{ana}) \tag{4.1}$$

with

$$\alpha(I_{ana}) = A_\alpha \cdot I_{ana}^2 + B_\alpha \cdot I_{ana} + C_\alpha \tag{4.2}$$

$$\beta(I_{ana}) = A_\beta \cdot I_{ana}^2 + B_\beta \cdot I_{ana} + C_\beta \tag{4.3}$$

$$\gamma(I_{ana}) = A_\gamma \cdot I_{ana}^2 + B_\gamma \cdot I_{ana} + C_\gamma \tag{4.4}$$

These fit functions are drawn for each ROC, see the appendix on pages 79 to 80. They have been evaluated at 17 distinct values of I_{ana} between 16 mA and 32 mA and at 17 distinct thresholds between 2 000 and 18 000 electrons. Although a few ROCs could be measured at lower or higher thresholds, the consideration of a wider range of thresholds would include extrapolations of all other ROCs leading to less reliable results.

The resulting $\Delta\theta$ at distinct θ and I_{ana} could now be compared among ROCs. For each of the pairs (θ, I_{ana}) a histogram has been filled with the evaluated fit functions $\Delta\theta(\theta,\, I_{ana})$ from the 16 ROCs, providing a set of $17 \times 17 = 289$ mean values $\overline{\Delta\theta(\theta,I_{ana})}^{ROCs}$ with the corresponding RMS. A selection of these histograms is shown in the appendix on page 81.

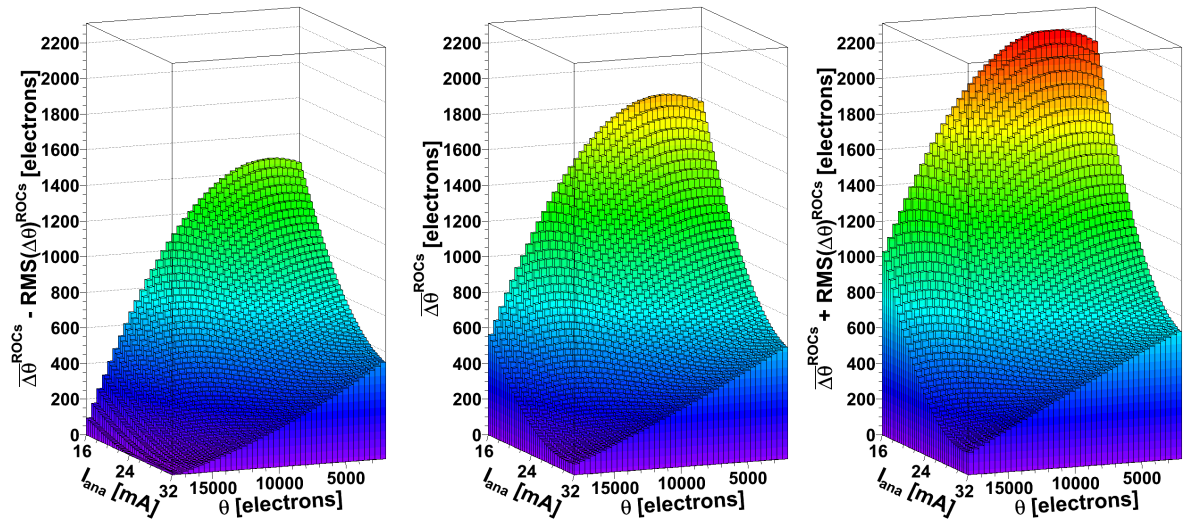

(a) (b) (c)

Figure 4.2: Expectation value and band edges of $\Delta\theta(\theta,\, I_{ana})$ at $T = 17°$C.

(a) $\overline{\Delta\theta(\theta, I_{ana})}^{ROCs} - \mathrm{RMS}(\theta,\, I_{ana})$: lower band edge from the ROC to ROC distribution.
(b) $\overline{\Delta\theta(\theta, I_{ana})}^{ROCs}$: expectation value.
(c) $\overline{\Delta\theta(\theta, I_{ana})}^{ROCs} + \mathrm{RMS}(\theta,\, I_{ana})$: upper band edge from the ROC to ROC distribution.

$\overline{\Delta\theta(\theta,I_{ana})}^{ROCs}$ is shown in figure 4.2b; it provides the expectation value of $\Delta\theta$. To estimate the distribution of $\Delta\theta$ among ROCs, $\overline{\Delta\theta(\theta,I_{ana})}^{ROCs}\pm\mathrm{RMS}(\theta,\, I_{ana})$ are shown in figures 4.2a and 4.2c. These three functions $\overline{\Delta\theta(\theta,I_{ana})}^{ROCs}-\mathrm{RMS}(\theta,\, I_{ana})$, $\overline{\Delta\theta(\theta,I_{ana})}^{ROCs}$ and $\overline{\Delta\theta(\theta,I_{ana})}^{ROCs}+\mathrm{RMS}(\theta,\, I_{ana})$ have been fitted also with the two-dimensional polynomial given in equations (4.1) to (4.4). The fit parameters are listed in table 4.1.

Together with equations (4.1) to (4.4) these parameters provide an error band from the ROC to ROC variation around the expectation value of $\Delta\theta$ for arbitrary θ and I_{ana}. This becomes a tool to calculate θ_{abs} out of θ_{int} and vice versa. As has been seen in the previous chapter, the largest uncertainty contribution to $\Delta\theta$ comes from the ROC to ROC variation considered here.

Table 4.1: Parameters $A_{\alpha,\beta,\gamma}$, $B_{\alpha,\beta,\gamma}$ and $C_{\alpha,\beta,\gamma}$ at $T = 17°C$.

		$\overline{\Delta\theta}^{ROCs}$ − RMS	$\overline{\Delta\theta}^{ROCs}$	$\overline{\Delta\theta}^{ROCs}$ + RMS	
	A_α	−1.954	−1.941	−1.928	$[\cdot 10^{-8} \cdot \text{electrons}^{-1} \cdot \text{mA}^{-2}]$
α	B_α	1.487	1.452	1.417	$[\cdot 10^{-6} \cdot \text{electrons}^{-1} \cdot \text{mA}^{-1}]$
	C_α	−2.668	−2.625	−2.582	$[\cdot 10^{-5} \cdot \text{electrons}^{-1}]$
	A_β	2.680	3.086	3.491	$[\cdot 10^{-4} \cdot \text{mA}^{-2}]$
β	B_β	−2.071	−2.271	−2.470	$[\cdot 10^{-2} \cdot \text{mA}^{-1}]$
	C_β	3.353	3.674	3.995	$[\cdot 10^{-1}]$
	A_γ	2.269	3.167	4.065	$[\cdot \text{ electrons} \cdot \text{mA}^{-2}]$
γ	B_γ	−1.521	−2.116	−2.711	$[\cdot 10^{2} \cdot \text{electrons} \cdot \text{mA}^{-1}]$
	C_γ	3.208	4.257	5.307	$[\cdot 10^{3} \cdot \text{electrons}]$

The function $\Delta\theta(\theta,\, I_{ana})$ with the parameters provided by table 4.1 is shown for distinct values of I_{ana} and thresholds in figures 4.3a and 4.3b.

The figures in the appendix on page 82 show the measured points of $\Delta\theta$ with the fit function of the single ROCs. They are grouped to measurements with the same I_{ana} and underlaid with the ROC to ROC distribution that has been calculated with the parameterization of table 4.1.

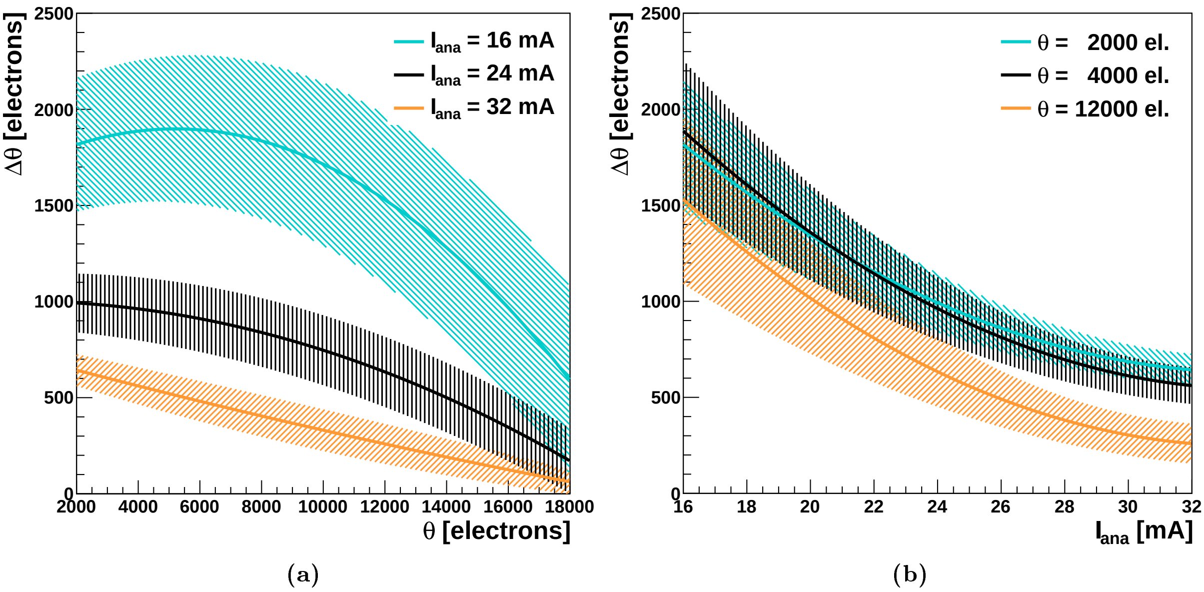

Figure 4.3: Expectation values and bands of $\Delta\theta$ for distinct I_{ana} and θ at $T = 17°C$. The expectation values and bands showing the RMS from the ROC to ROC distribution are calculated with the parameterization provided by table 4.1.

4.2 $\Delta\theta$ as a Function of θ and I_{ana} at $T = -10\,°\mathrm{C}$

Exactly the same measurements (parameters and examined pixels) and analysis as at the temperature $T = 17\,°\mathrm{C}$ (see previous section) have been repeated at the temperature $T = -10\,°\mathrm{C}$. The results are presented in this section.

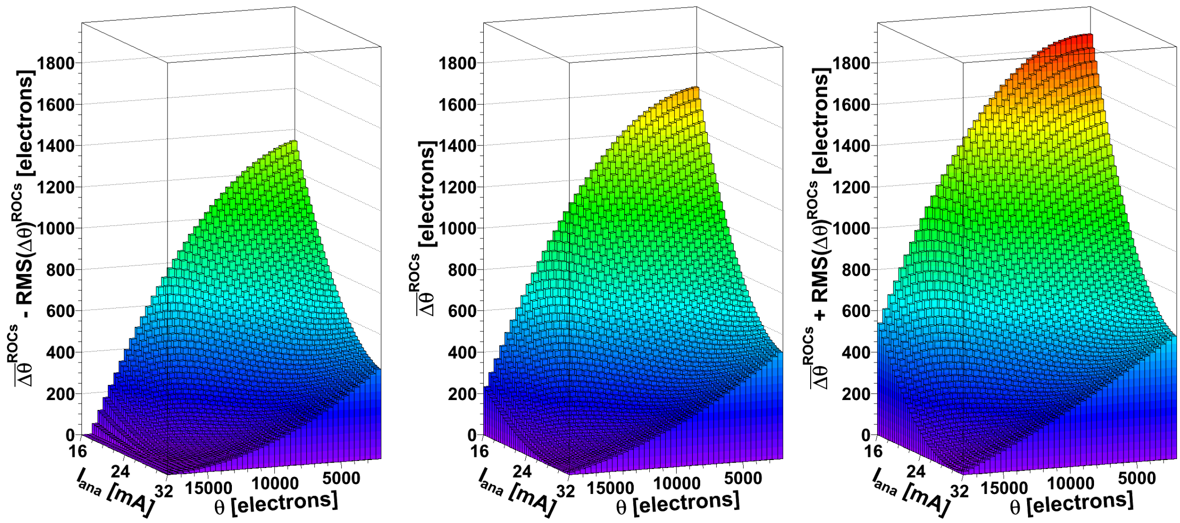

(a) (b) (c)

Figure 4.4: Expectation value and band edges of $\Delta\theta(\theta,\, I_{ana})$ at $T = -10°$C.
(a) $\overline{\Delta\theta(\theta, I_{ana})}^{ROCs} - \mathrm{RMS}(\theta,\, I_{ana})$: lower band edge from the ROC to ROC distribution.
(b) $\overline{\Delta\theta(\theta, I_{ana})}^{ROCs}$: expectation value.
(c) $\overline{\Delta\theta(\theta, I_{ana})}^{ROCs} + \mathrm{RMS}(\theta,\, I_{ana})$: upper band edge from the ROC to ROC distribution.

The measured graphs of $\Delta\theta$ vs. θ are shown for each ROC on pages 83 to 85 in the appendix. The two-dimensional fit function given in equations (4.1) to (4.4) has been applied ROC-wise to the two-dimensional graphs $\Delta\theta(\theta,\, I_{ana})$.

Table 4.2: Parameters $A_{\alpha,\beta,\gamma}$, $B_{\alpha,\beta,\gamma}$ and $C_{\alpha,\beta,\gamma}$ at $T = -10°$C.

		$\overline{\Delta\theta}^{ROCs} - \mathrm{RMS}$	$\overline{\Delta\theta}^{ROCs}$	$\overline{\Delta\theta}^{ROCs} + \mathrm{RMS}$	
	A_α	−4.042	−3.093	−2.429	$[\cdot 10^{-8} \cdot \mathrm{electrons}^{-1} \cdot \mathrm{mA}^{-2}]$
α	B_α	2.348	1.886	1.562	$[\cdot 10^{-6} \cdot \mathrm{electrons}^{-1} \cdot \mathrm{mA}^{-1}]$
	C_α	−3.221	−2.762	−2.464	$[\cdot 10^{-5} \cdot \mathrm{electrons}^{-1}]$
	A_β	6.091	4.648	3.796	$[\cdot 10^{-4} \cdot \mathrm{mA}^{-2}]$
β	B_β	−3.340	−2.687	−2.319	$[\cdot 10^{-2} \cdot \mathrm{mA}^{-1}]$
	C_β	3.859	3.297	3.066	$[\cdot 10^{-1}]$
	A_γ	1.864	2.954	3.806	$[\ \mathrm{electrons} \cdot \mathrm{mA}^{-2}]$
γ	B_γ	−1.417	−2.047	−2.563	$[\cdot 10^{2} \cdot \mathrm{electrons} \cdot \mathrm{mA}^{-1}]$
	C_γ	3.191	4.165	5.006	$[\cdot 10^{3} \cdot \mathrm{electrons}]$

The resulting plots are shown in the appendix on pages 86 to 87. These fit functions have been evaluated at distinct values of θ and I_{ana} and have been filled into histograms. A selection of them is shown on page 88.

Graphs of their mean values $\overline{\Delta\theta}^{ROCs}$ and of $\overline{\Delta\theta}^{ROCs}\pm$RMS are shown in figures 4.4. The fit of equations (4.1) to (4.4) has been calculated for these three graphs too. The resulting parameters are listed in table 4.2.

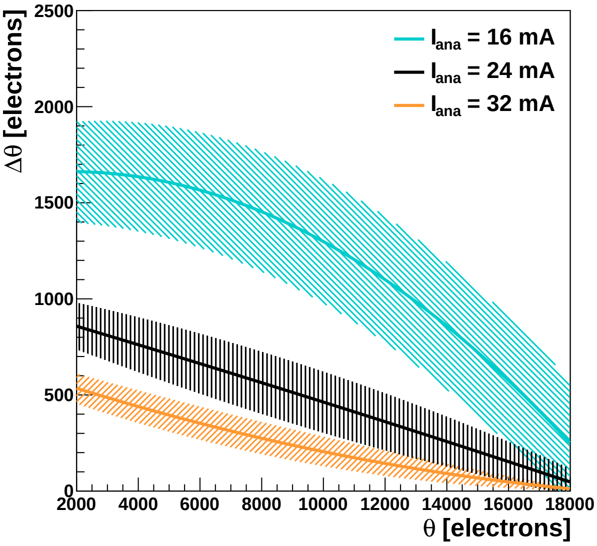

(a)

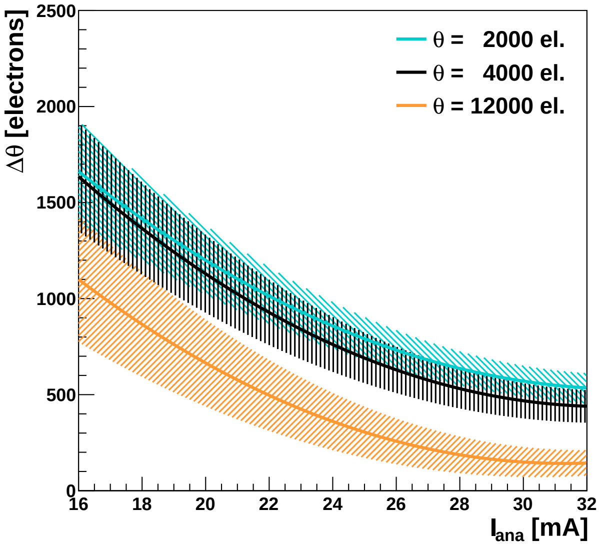

(b)

Figure 4.5: Expectation values and bands of $\Delta\theta(\theta)$ for distinct I_{ana} at $T = -10°$C. The expectation values and the bands showing the RMS from the ROC to ROC distribution are calculated with the parameterization provided by table 4.2.

Together with equations (4.1) to (4.4), these parameters allow predictions of $\Delta\theta$ for arbitrary θ and I_{ana} at $-10\,°$C with the uncertainty due to the ROC to ROC variation. Figures 4.5a and 4.5b show the expectation value of $\Delta\theta$ for distinct θ and I_{ana} with the error bands from the ROC to ROC variation, calculated with the parameterization of table 4.2.

4.3 Temperature Dependency of $\Delta\theta$

To see the influence of the temperature on $\Delta\theta$ more clearly, the graphs of figures 4.3a and 4.3b are shown together with the graphs of figures 4.5a and 4.5b in the figures 4.6 and 4.7. In addition the corresponding graphs for $I_{ana} = 20$ and $28\,$mA and for $\theta = 3000$ and 6000 electrons are shown.

It can be seen, that the temperature change of at least $25\,°$C has no huge effect on $\Delta\theta$. The ranges of $\Delta\theta(T = 17\,°\text{C})$ and of $\Delta\theta(T = -10\,°\text{C})$ overlap, which means that the ROC to ROC variation is at least of the same order as temperature effects. However, $\Delta\theta$ is systematically smaller for low temperatures and the shape of the θ- and I_{ana}-dependencies of $\Delta\theta$ changes with the temperature.

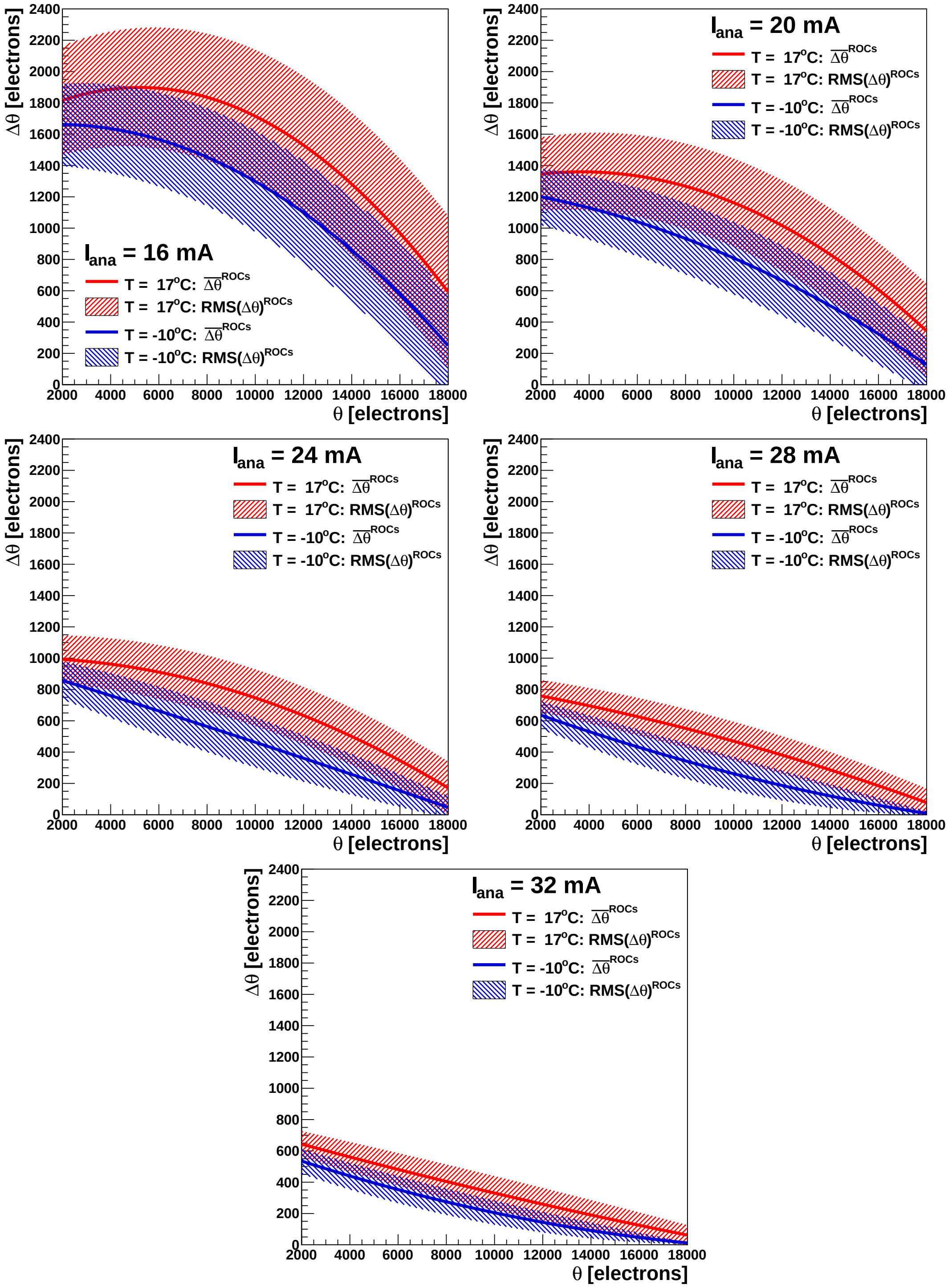

Figure 4.6: Comparison of $\Delta\theta(\theta)$ at $T = -10$ and $17°$C for distinct I_{ana}.

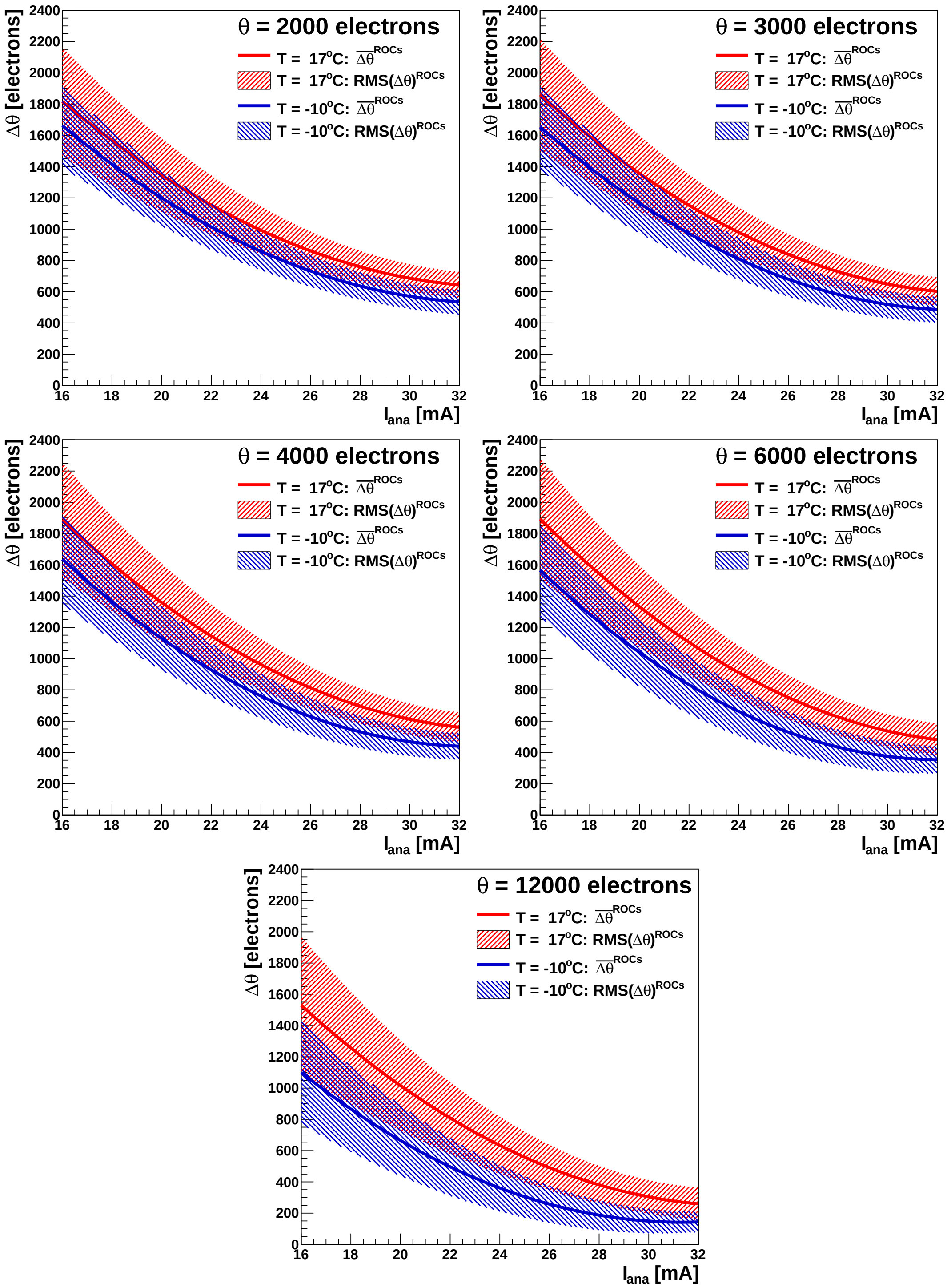

Figure 4.7: Comparison of $\Delta\theta(I_{ana})$ at $T = -10$ and 17°C for distinct θ.

5 Simulations and Discussion

The measured results from the previous chapter are discussed here and compared with toy simulations of the calibration signal to check, if the observed effects can be understood. The aim has not been to do a detailed simulation that could lead to results numerically comparable to the measurements. For such a simulation the knowledge about shape and dependencies of the calibration signal is by far not sufficient. A simple toy simulation (section 5.1) has been done instead to show, what has been naïvely expected for $\Delta\theta(\theta, I_{ana})$. As this simulation does not match the measured results, some effects have been included in an improved toy simulation in section 5.2 to check, if they could explain the measurements. By the way this simulation has been done, it can only provide *possible* explanations of measured effects. Both simple and improved simulation have been done with the program `thrsim.C`.

The main effects that have been measured and are investigated by the simulations are:

- Negative slope of $\Delta\theta(I_{ana})$.
- Negative slope of $\Delta\theta(\theta)$ for high thresholds.
- Saturation or positive slope of $\Delta\theta(\theta)$ for low thresholds and small I_{ana}.
- Convergence of $\Delta\theta(\theta)$ to 0 for very high thresholds and large I_{ana}.

5.1 (Too) Simple Toy Simulation of $\Delta\theta(\theta, I_{ana})$

Although the signal V from pixels is a negative voltage, its absolute value is considered here, which is supposed to be linear in `Vcal` with a positive slope. Therefore, the simulated signal pulse height is always given in units of `Vcal` as it is accessible in measurements. Only when calculating $\Delta\theta$, a calibration to electrons is made to compare the simulation with the measurements.

5.1.1 Pulse Shape of the Pixel Calibration Signal

The main uncertainty of the simulation concerns the shape of the calibration signal. As it is not known (and not trivial to measure, some effort has been done), it is assumed to rise like the signal of a low pass filter: The signal `V` rises suddenly after being triggered at time t_0 and converges to the default voltage `Vcal`,

$$\mathtt{V}(t) = \mathtt{Vcal} \cdot \left[1 - e^{-\frac{t-(t_0+Delays)}{\tau}}\right] + \mathtt{V}_0, \tag{5.1}$$

where `V` is the pulse height at time t, `Vcal` the parameterized applied calibration voltage, τ the time constant defining the rise time and $\mathtt{V}_0$ the offset, i.e. the amplitude, if no voltage is applied. $\mathtt{V}_0$ is in first approximation supposed to be independent of measured variables and will not be discussed here further (for the simulations it has been set to 0). $t_0 + Delay$ is by definition the time, when the signal starts to rise. In the simple case, where no other delays than *CalDelay* are considered, it is

$$Delay = CalDelay = 0.4265 \cdot \texttt{CalDel}, \tag{5.2}$$

the delay which can be experimentally set by the DAC parameter `CalDel` (see section 2.3.4). In order to set the `WBC` value of interest such, that it covers the time range $0 \ldots 25\,\text{ns}$, t_0 is chosen to be $-80\,\text{ns}$. These choices only define the time axis and the relevant range of `CalDel`; they have no physical impact. The offset c of *CalDelay* introduced in equation (2.4) has been set to 0. However, the results of the simulation do not depend on it, as a change of c would only shift the time axis. Figures 5.1 show the dependencies of $\texttt{V}(t)$ on `Vcal`, `CalDel` and τ according to equations (5.1) and (5.2).

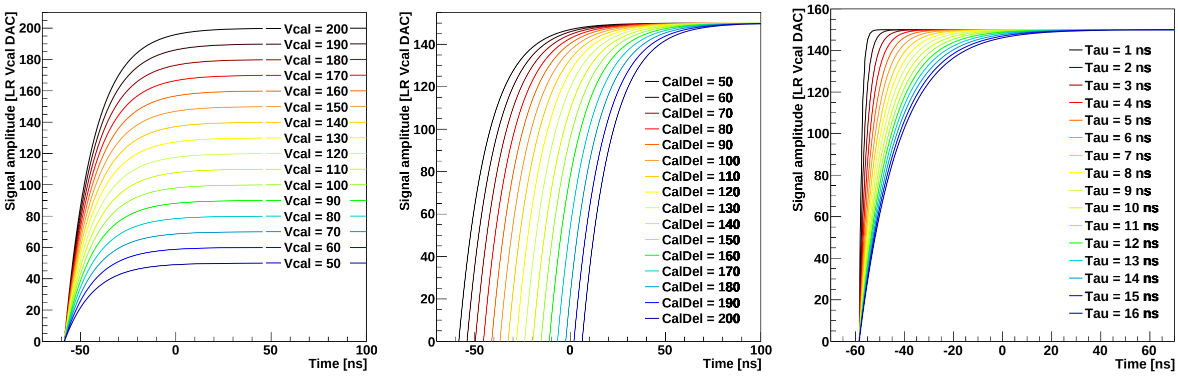

(a) $\texttt{CalDel} = 50$, $\tau = 5$ **(b)** $\texttt{Vcal} = 150$, $\tau = 5$ **(c)** $\texttt{CalDel} = 50$, $\texttt{Vcal} = 150$

Figure 5.1: Amplitude of the calibration signal as a function of `Vcal`, `CalDel` and τ. These curves have been calculated with equations (5.1)and (5.2) and the indicated parameters according to the simple simulation.

One question concerned the impact of I_{ana}. In this simulation it is supposed to act only on τ the following way:

$$\tau(I_{ana}) = \frac{24\,\text{mA}}{I_{ana}} \cdot \tau(I_{ana} = 24\,\text{mA}). \tag{5.3}$$

The background of this equation is the assumption, that I_{ana} is proportional to the gain of amplifiers. $\tau(I_{ana} = 24\,\text{mA})$ is a free parameter.

5.1.2 Naïve Phenomenological Expectation of $\Delta\theta(\theta)$

Figure 5.2 shows phenomenologically, why one would expect a rising $\Delta\theta$ for rising θ, if the signal shape described by equation (5.1) was correct with no other delays than *CalDelay*. It can be seen clearly, that $\Delta\theta$ is larger at high thresholds than at low thresholds. The combination of the following assumptions leads always to a positive slope of $\Delta\theta(\theta)$:

- No falling edge is considered, i.e. the first derivative of the signal amplitude is positive at least until the end of the time-window, within which a signal is accepted (set by the `WBC`).
- The second derivative of the signal amplitude as a function of time is negative for all times.
- The signals start rising at the same time for all θ and `Vcal`.

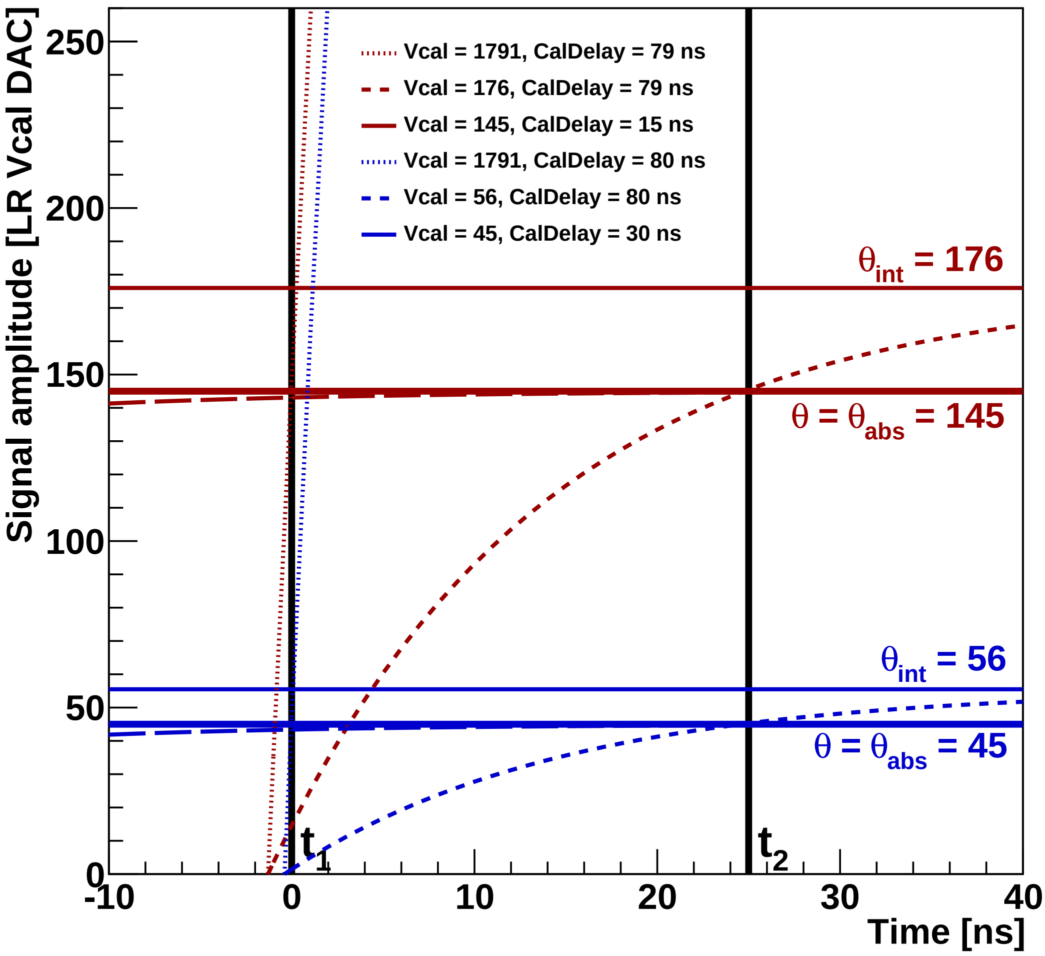

Figure 5.2: Phenomenological explanation of the expected positive slope of $\Delta\theta(\theta)$. This figure is basically the same as figure 3.1 but for two different thresholds and numerically better motivated. Blue lines concern the threshold set to $\theta = 45$ LR `Vcal` units, brown lines the threshold set to $\theta = 145$ LR `Vcal` units. The thresholds are drawn as thick lines. The three smaller lines represent the signals that determine θ_{int} and θ_{abs}. $t_1 = 0$ and $t_2 = 25\,\text{ns}$ define the time window of the `WBC` of interest.
The crossings of the dotted lines (signals at maximum `Vcal` = 1 791 LR DAC units = 255 HR DAC units) with the time axis indicate the time, when at the earliest signals can start to be allocated to the `WBC`. This time corresponds to $\texttt{CalDel}_{\texttt{LA}}$ in the measurements. Therefore the `Vcal` values of the signals starting at this time and reaching the threshold just at t_2 (small dashed lines) define the in-time thresholds. The signals that define the absolute thresholds (widely dashed lines) may start earlier, but they have to reach the threshold between t_1 and t_2 to be allocated to the `WBC` and to be measured in the scans.
All signal amplitudes shown here have been drawn evaluating equation (5.1) with *CalDelay* provided by equation (5.2) and τ provided by equation (5.3). For the `Vcal` values have been taken the results of the simple simulation at $I_{ana} = 24\,\text{mA}$ presented in subsection 5.1.4 with the parameters $\tau(I_{ana} = 24\,\text{mA}) = 15\,\text{ns}$, $I_{ana} = 24\,\text{mA}$, $t_0 = -80\,\text{ns}$, $\texttt{V}_0 = 0$.

5.1.3 Principles of the Simple Toy Simulation

It was not necessary to consider HR `Vcal` units for the simulation. It was simply done in LR, but for the enlarged range $0 \ldots 1\,791 = 7 \cdot 256 - 1$ LR `Vcal` units, which covers the whole HR but with the resolution of the LR.

For given I_{ana} and θ in `Vcal` units, a two-dimensional histogram of the number of readouts as a function of `CalDel` and `Vcal` should first be generated as the measured ones. For the shape of $\texttt{V}(t)$ was considered equation (5.1) with *CalDelay* provided by (5.2) and τ provided by (5.3). For each `CalDel` value in the range $0 \ldots 255$ and each `Vcal` value in the range $0 \ldots 1\,791$, $\texttt{V}(t)$ has been evaluated at times $t_1 = 0$ and $t_2 = 25\,\text{ns}$, the time window of the `WBC` of interest. If

$$\texttt{V}(t_1, \texttt{CalDel}, \texttt{Vcal}) < \theta \qquad \wedge \qquad \texttt{V}(t_2, \texttt{CalDel}, \texttt{Vcal}) > \theta, \tag{5.4}$$

the signal crossed θ within the `WBC` between t_1 and t_2 and has therefore been accepted as a hit. In this case, the bin content of the bin (`Vcal`, `CalDel`) has been set to 50 (the number of triggers in the measurements), else it has been set to 0. Two examples of the resulting histograms are shown in figures 5.3 with lines indicating $\texttt{CalDel}_{\texttt{LA}}$, θ_{abs} and θ_{int}.

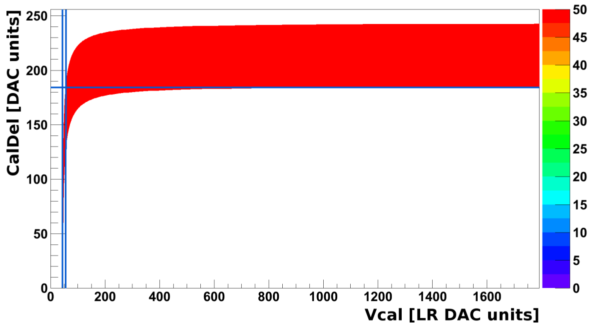

(a) $\theta = 45$ LR `Vcal` units, $\tau = 15$ ns

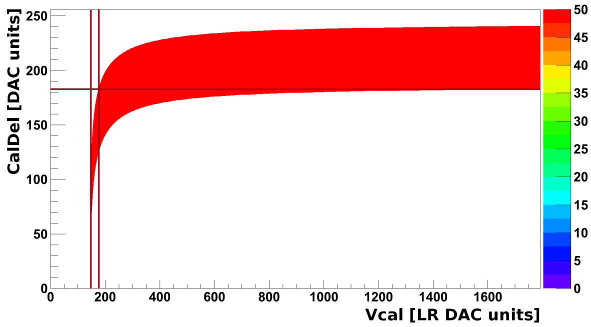

(b) $\theta = 145$ LR `Vcal` units, $\tau = 15$ ns

Figure 5.3: Simulated number of readouts vs. `Vcal` and `CalDel`.
Horizontal lines represent the lower asymptote at $\texttt{CalDel}_{\texttt{LA}}$, the vertical lines θ_{abs} (at lower `Vcal`) and θ_{int} (at higher `Vcal`) as determined by the analysis. These two examples provide the numerical basis for figure 5.2, in which the time development of the relevant calibration signals have been drawn.

θ_{int} and θ_{abs} have been determined from such simulated scans using the same algorithms as for the measurements with some simplifications:

- There was no need of fitting SCurves, as step functions would have been fitted. To have nevertheless a resolution higher than one DAC unit, the number of bins per DAC unit has been a parameter of the simulation. For the results presented here it has been set to 4 bins per DAC unit both for `Vcal` and `CalDel`.
- The lower amplitude needed for θ_{int} has been determined directly from the enlarged LR histogram at $\texttt{Vcal} = 1\,791$ LR DAC units.
- Taking averages over several lines as it had been done in the analysis of the measured data was not necessary for the simulation due to lack of statistical fluctuations.

After the determination of θ_{abs} and θ_{int}, they have been calibrated from `Vcal` units to electrons as it was done in the data analysis. For the values of $\mathtt{V}_{\mathtt{cal}}^{Mo}$ and $\mathtt{V}_{\mathtt{cal}}^{Ag}$ needed for that (see section 3.4) have been taken the values from the X-ray calibration of ROC 3, averaged over all pixels. ROC 3 has been chosen, because the main measured effects (listed in the introduction of this chapter) occur in that ROC.

5.1.4 Results of the Simple Toy Simulation

Simulations of $\Delta\theta$ as described in the previous subsection have been done for $I_{ana} = 16, 20, 24, 28$ and $32\,\mathrm{mA}$ and for all thresholds in the range $45 \ldots 185$ `Vcal` units with step size 20, which is about the range and stepsize typically measured. The simulations have been done with different parameter settings. The results presented here have been achieved with the following settings:

$$\tau(I_{ana} = 24\,\mathrm{mA}) = 15\,\mathrm{ns}$$
$$t_0 = -80\,\mathrm{ns}$$
$$\mathtt{V}_0 = 0$$

In the improved simulation (see the following section) $\tau(I_{ana} = 24\,\mathrm{mA}) = 4\,\mathrm{ns}$ has been used. If this value is used here, the scales change, but the signs of slopes remain the same.

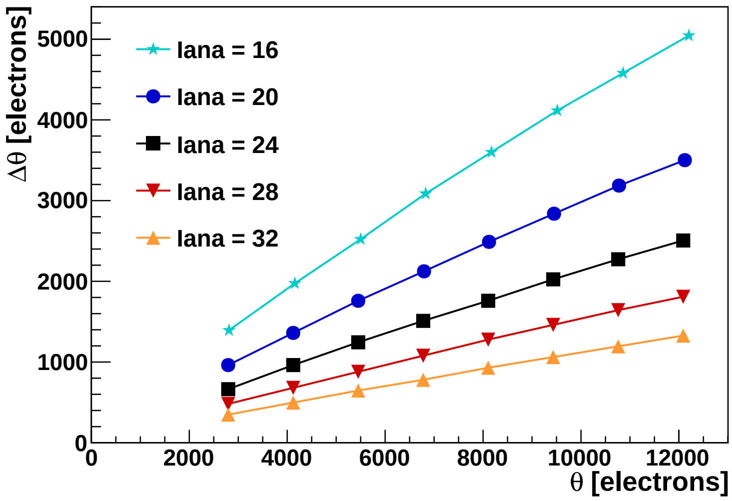

Figure 5.4: $\Delta\theta(\theta)$ for distinct I_{ana}, generated by the simple simulation.

The positive slope of $\Delta\theta(\theta)$ in this model can be derived directly by the assumptions (see section 5.1.2), but it can also be seen in figures 5.3, that the low `Vcal` part is pulled stronger towards low `CalDel` for the larger threshold, i.e. θ_{int} and with it $\Delta\theta$ have to be larger, as indicated in figure 5.2.

Figure 5.4 shows the simulated $\Delta\theta(\theta)$ for all I_{ana} in the whole range of θ. This simple simulation reproduces correctly a negative slope of $\Delta\theta(I_{ana})$, so the impact of I_{ana} might be the simulated one. For the dependency of $\Delta\theta$ on θ, the simulation produces the naïvely expected positive slope, while a negative slope has been measured for nearly the whole range of I_{ana} and θ. Reasons for this unexpected behavior had to be found and a more sophisticated model had to be thought of.

5.2 Improved Toy Simulation of $\Delta\theta(\theta, I_{ana})$

5.2.1 Comparator Effects and Cut on `Vcal`

Meditating on figures of the number of readouts vs. `Vcal` and `CalDel`, it has become clear, that `Vcal`-dependent delays — if they are large for low `Vcal` — can lead to a negative slope of $\Delta\theta(\theta)$. It has been found, that the comparator may introduce such delays.

Impact of Delays Caused by the Comparator on the Calibration Signal

In contrast to *CalDelay*, which effectively causes a delayed start of the calibration signal with respect to the CalTrigReset signal (see [10]), the comparator does actually not have any effect on the starting time of the calibration signal. However, the time stamp of a signal (which allocates the signal to a certain bunch crossing) is set only after it has reached the threshold in the comparator. Therefore it makes no difference if the signal starts delayed or if the comparator introduces a delay before the time stamp is set. Thus delays originated from the comparator, called *CompDelay*, can be introduced in equation (5.1) just like *CalDelay*:

$$Delay = CalDelay + CompDelay. \tag{5.5}$$

θ-dependent Delay Caused by the Comparator: $CompDelay_\theta$

The `Vcthr`-dependency of the delay caused by the comparator has been simulated in detail [18]. The results of this simulation are shown in figure 5.5a. It can be seen, that the introduced delay $CompDelay_\theta$ is large for high θ (low `Vcthr`). This can not explain the negative slope of $\Delta\theta(\theta)$. For each measurement of $\Delta\theta$, `Vcthr` was held constant, which means that $CompDelay_\theta$ produces only shifts of the time axis or of that `CalDel` range in the scans, where the readout efficiency is above 0. In addition, this delay produces larger effects only for high thresholds and is therefore of minor importance for $\Delta\theta$ in the range of interest. Nevertheless, this delay has been considered in this simulation. The evaluation of $CompDelay_\theta$(`Vcthr`) has been done with spline functions.

As θ was set in `Vcal` units for the simulation, it had to be converted to units of `Vcthr` before calculating $CompDelay_\theta$. For this conversion the number of readouts of ROC 3 vs. `Vcal` and `Vcthr` has been measured (ROC 3 has been used also for the calibration from `Vcal` to electrons). This plot is shown in figure 3.11 on page 39. A SCurve fit has been applied to each line of `Vcal`, providing doublets (`Vcal`,`Vcthr`) of 50 % readout probability. These points are shown in figure 5.5b and have been fitted with a 2$^{\text{nd}}$ degree polynomial. The resulting function `Vcthr`(`Vcal`) is

$$\theta[\texttt{Vcthr}] = 0.001097 \cdot \theta^2[\texttt{Vcal}] - 0.7041 \cdot \theta[\texttt{Vcal}] + 159.6. \tag{5.6}$$

The reason for $CompDelay_\theta$ might be, that the time stamp is set only when the signal reaches the threshold. Due to the rising time, a signal will therefore trigger later, if the threshold is set high, than the same signal with a low set threshold.

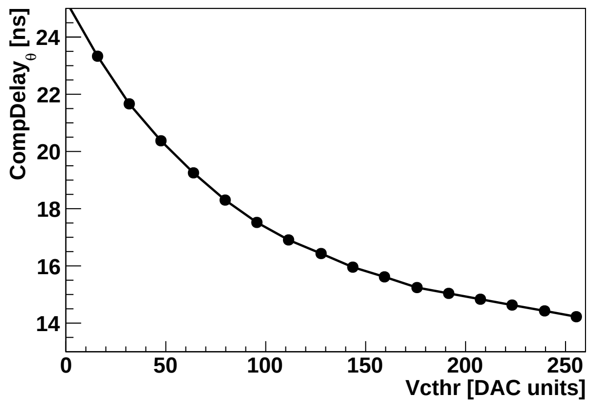

(a)

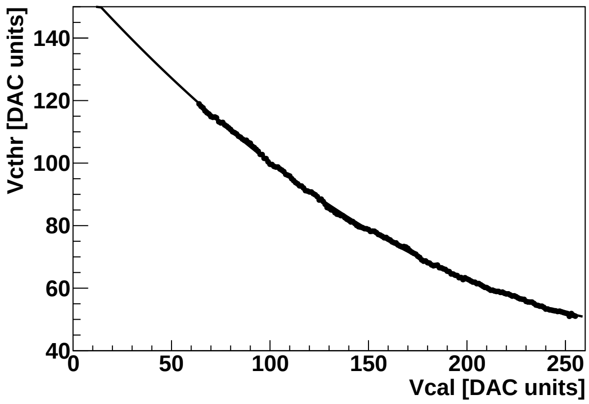

(b)

Figure 5.5: Simulation of $CompDelay_\theta(\texttt{Vcthr})$ and measurement of `Vcthr` vs. `Vcal`.
(a) The points $(\texttt{Vcthr}, CompDelay_\theta)$ resulted from a detailed simulation [18].
(b) The points $(\texttt{Vcal}, \texttt{Vcthr})$ resulted from SCurve fits of the measurement shown in figure 3.11. The line is a 2^{nd} degree polynomial fit.

`Vcal`-dependent Delay Caused by the Comparator: $CompDelay_{\texttt{Vcal}}$

The simulation of the comparator [18] shows, that there is a `Vcal`-dependency caused by the comparator, but until this study has been finished, its shape has not been known at all. To understand possible reasons for `Vcal`-dependent delays, a deeper understanding of the comparator is necessary. In a simplified model it can be considered as shown in figure 5.6.

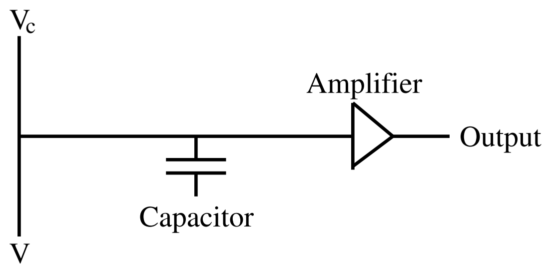

Figure 5.6: Simplified model of the comparator.

The signal amplitude V is compared to an internal voltage V_c that is regulated by `Vcthr`. When the signal exceeds V_c, the difference $V - V_c$ produces a signal that is amplified and triggers the time stamp at the output. A `Vcal` dependent delay might be introduced by unwanted small capacitors between the comparison of V with V_c and the amplifier. Before the comparator triggers, these capacitors are filled. This takes more time for small amplitudes than for large amplitudes and leads to a negative slope of $CompDelay_{\texttt{Vcal}}$.

Due to the fact, that the signal leading to $CompDelay_{\texttt{Vcal}}$ is basically a cut calibration signal, a low pass filter function is assumed too:

$$\texttt{V}_1 = \left[1 - e^{-\frac{CompDelay_{\texttt{Vcal}})}{\tau_c}}\right] \cdot (\texttt{Vcal} + \texttt{V}_{\texttt{shift}}). \tag{5.7}$$

After transformation, this is

$$CompDelay_{\mathtt{Vcal}} = -\tau_c \cdot \ln\left[1 - \frac{\mathtt{V}_1}{\mathtt{Vcal} + \mathtt{V}_{\mathtt{shift}}}\right]. \tag{5.8}$$

The newly introduced parameters $\mathtt{V}_1$, τ_c and $\mathtt{V}_{\mathtt{shift}}$ are free as long as there is not more known about the exact behavior of the comparator. They could be interpreted as follows:

- $\mathtt{V}_1$: The minimal difference between the signal amplitude and the threshold that is necessary to fill the capacitors (corresponding to an additional internal threshold).
- τ_c: The time constant of the signal rise within the comparator.
- $\mathtt{V}_{\mathtt{shift}}$: An additional offset.

The results presented in the following have been achieved with $\mathtt{V}_1 = 10$ LR `Vcal` DAC units, $\tau_c = 150$ ns and $\mathtt{V}_{\mathtt{shift}} = 0$. In conjunction with the setting of the other parameters, this set of parameters produces a negative slope of $\Delta\theta(\theta)$ and is therefore the major improvement compared to the simple model of the previous section.

Cut on Low `Vcal`

As shown in the last paragraph, the filling of the capacitors in the comparator might take time, especially for signals that just reach the threshold. If the signal starts falling before the capacitors are filled, the comparator does not trigger at all. Such situations can occur for low and for high thresholds. But for low thresholds the rise of the signals with maximum amplitudes just above the threshold is slower than for high thresholds. This leads to the allocation of the signal to the wrong bunch crossing. This effect is considered by a cut at $\mathtt{Vcal} = 60$. In the histograms of the number of readouts vs. `Vcal` and `CalDel` the bin content of bins at `Vcal` values below 60 has been set to 0. Such an edge can be seen also in measured histograms, although it is smeared out there.

This cut leads to a positive slope of $\Delta\theta(\theta)$ for very low thresholds for small I_{ana} and to a saturation for large I_{ana}.

5.2.2 Consideration of the Falling Edge of the Calibration Signal

The falling edge of the calibration signal has been considered in the improved simulation by the introduction of an arctan-function cutting smoothly the signal. Normalized to 1, it is

$$\mathtt{V}(t) \propto \frac{1}{2} \cdot \left[1 - \frac{2}{\pi} \cdot \arctan\left(\frac{t - (Delays + t_f)}{\tau_f}\right)\right]. \tag{5.9}$$

The parameter τ_f is the time constant, with which the signal falls, and t_f sets the time, when the signal has been reduced by 50 %, relative to the time, when it starts rising. They have been chosen to be $\tau_f = 25$ ns and $t_f = 180$ ns. If the explanation of the positive slope of $\Delta\theta(\theta)$ in the previous subsection is correct, it should be actually possible to replace the cut on low `Vcal` by an appropriate choice of τ_f and t_f, which is expected to be rather around 25 ns anyway. However, with the chosen set of parameters, the cut was still necessary to produce a positive slope.

The criteria to accept a signal lying within the `WBC` had to be modified with the consideration of the falling edge. The signal $\mathtt{V}(t)$ has been accepted and the corresponding bin content $(\mathtt{Vcal}, \mathtt{CalDel})$ has been set to 50, if

$$\mathtt{V}(t_1) < \theta \quad \wedge \quad \frac{d\mathtt{V}}{dt}(t_1) > 0 \quad \wedge \quad \left[\mathtt{V}(t_1) > \theta \quad \vee \quad \left(\frac{d\mathtt{V}}{dt}(t_2) < 0 \quad \wedge \quad \mathtt{V}(t_2) > \theta\right)\right], \qquad (5.10)$$

else it was set 0. Actually these criteria do not consider signals that exceed the threshold after t_1 and fall below it before t_2. Due to the large t_f this error is negligible (tests have been done). However it could be omitted at all by the determination of the maximum amplitude that a signal reaches. It has not been done to save calculation time.

5.2.3 Modified Pulse Shape of the Calibration Signal

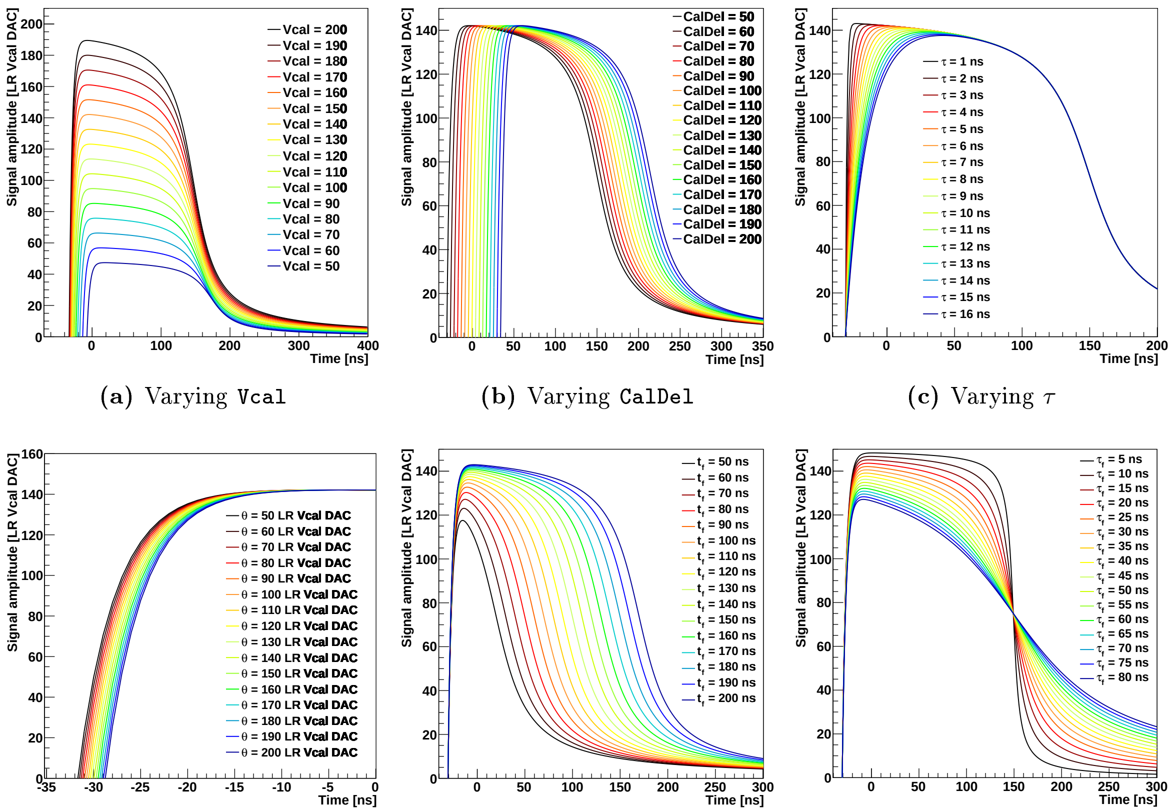

(a) Varying `Vcal` **(b)** Varying `CalDel` **(c)** Varying τ

(d) Varying θ **(e)** Varying t_f **(f)** Varying τ_f

Figure 5.7: Calibration signal as a function of `Vcal`, `CalDel`, τ, θ, t_f and τ_f. The pulse shapes of the calibration signals have been calculated with equation (5.11). The parameters not varied are the default ones listed in subsection 5.2.4. In addition `Vcal` has been set to 150 LR `Vcal` DAC units, θ to 100 LR `Vcal` DAC units, `CalDel` to 50 DAC units.

Considering the comparator effects and the falling edge, the signal shape described by equation (5.1) has been modified to

$$\begin{aligned} \mathtt{V}(t) = &\left(\mathtt{V_{cal}} \cdot \left[1 - e^{-\frac{t-(t_0+CalDelay+CompDelay_\theta+CompDelay_{\mathtt{Vcal}})}{\tau}}\right] + \mathtt{V}_0\right) \\ &\cdot \left(\frac{1}{2} \cdot \left[1 - \frac{2}{\pi} \cdot \arctan\left(\frac{t-(t_0+CalDelay+CompDelay_\theta+CompDelay_{\mathtt{Vcal}}+t_f)}{\tau_f}\right)\right]\right). \end{aligned} \tag{5.11}$$

Figures 5.7 show the behavior of this function varying different parameters. The following differences with respect to figures 5.1 are remarkable:

- The signal amplitude will never reach its default maximum amplitude `Vcal` (here 150 DAC units) due to the falling edge.
- The variation of `Vcal` not only changes the maximum amplitude of the signal but also introduces a shift in time due to $CompDelay_{\mathtt{Vcal}}$.
- The variation of the time-parameters t_f, τ and τ_f not only has effects on the time, but also on the maximum pulse height via their effects on the falling edge.

5.2.4 Results of the Improved Toy Simulation

The ranges $\theta = 45 \ldots 185$ LR `Vcal` units and $I_{ana} = 16, 20, 24, 28$ and $32\,\text{mA}$ that have been simulated are the same as in the previous section. For the evaluation of equation (5.11) has been used the following set of parameters:

$$\begin{aligned} \tau(I_{ana} = 24\,\text{ns}) &= 4\,\text{ns} \\ \tau_c &= 150\,\text{ns} \\ \tau_f &= 25\,\text{ns} \\ t_0 &= 0\,\text{ns} \\ t_f &= 180\,\text{ns} \\ \mathtt{V}_0 &= 0 \\ \mathtt{V}_1 &= 10\,\text{LR } \mathtt{Vcal} \text{ DAC units} \\ \mathtt{V_{shift}} &= 0 \end{aligned}$$

τ has been calculated with equation (5.3), $CalDelay$ with equation (2.4), $CompDelay_\theta$ with equation (5.6) and $CompDelay_{\mathtt{Vcal}}$ with equation (5.8).

Figures 5.8 show two examples of the histograms of the number of readouts vs. `Vcal` and `CalDel` for the thresholds 45 and 145 LR Vcal DAC units. They have been generated the same way as figures 5.3, but with the modified signal shape of equation (5.11), the acceptance criteria of (5.10) and the cut on low `Vcal` applied. The cut plays a role only in figure 5.8a. If it was not set, $\Delta\theta$ would be even larger. Figure 5.10 shows the time development of the signals that define θ_{int} and θ_{abs} in these cases.

The simulated $\Delta\theta$ for the whole range of θ and I_{ana} is shown in figure 5.9. Obviously this toy simulation can reproduce the main measured effects (see the beginning of this chapter), and the considered effects provide a possible explanation for them. However, the simulated shapes do not match the measured shapes, which can have different reasons.

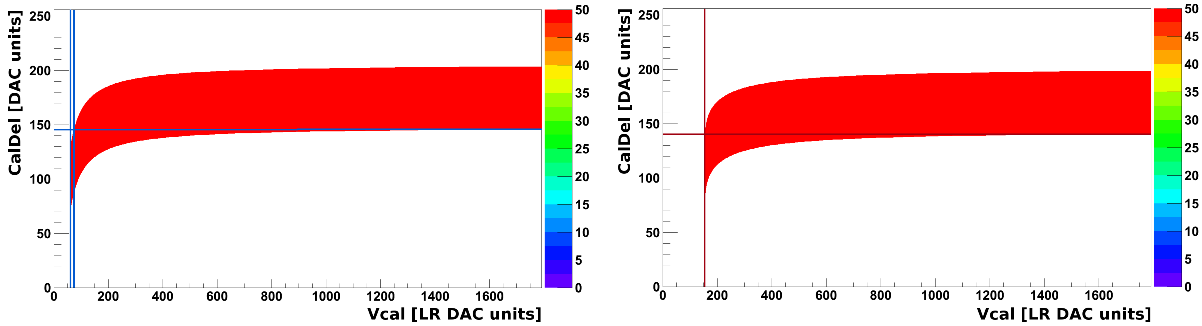

(a) (b)

Figure 5.8: Simulated number of readouts vs. `Vcal` and `CalDel`.
These figures are based on the improved simulation of the calibration signal and correspond to the figures 5.3 in the simple model.
Horizontal lines represent the lower asymptote at $\texttt{CalDel}_{\texttt{LA}}$, the vertical lines θ_{abs} (at lower `Vcal`) and θ_{int} (at higher `Vcal`). In (b) the two lines of θ_{abs} and θ_{int} are very close, such that they can hardly be differentiated.
These two examples provide the numerical basis for figure 5.10.

There are on the one hand too many free parameters to determine easily the best choice of parameters. On the other hand assumptions of the calibration signal and of comparator effects have been made that are not stringent.

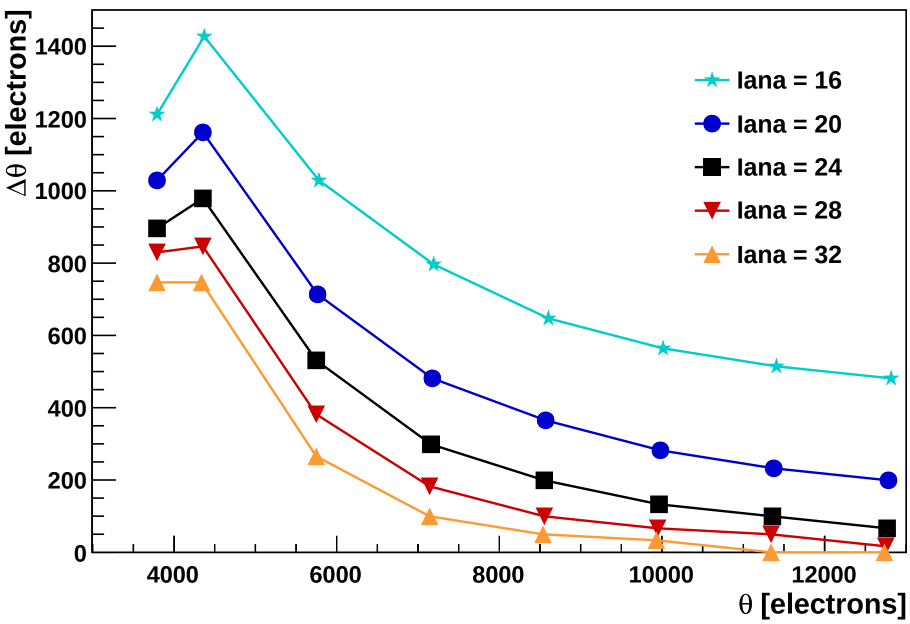

Figure 5.9: $\Delta\theta(\theta)$ for distinct I_{ana}, generated by the improved simulation.

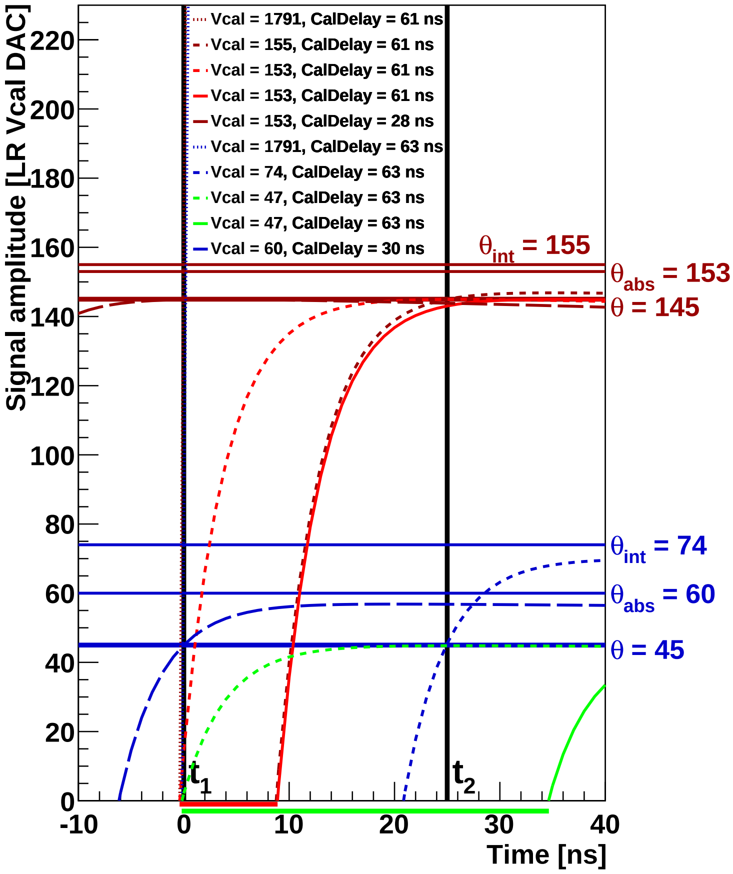

Figure 5.10: Phenomenological explanation of the measured negative slope of $\Delta\theta(\theta)$. As in figure 5.2 for the simple simulation, the time development of those signals that are relevant for the $\Delta\theta$ determination is shown here for two different thresholds (thick lines; blue: $\theta = 45$, brown: $\theta = 145$ LR `Vcal` DAC units). The times $t_1 = 0$ and $t_2 = 25$ ns define the `WBC` of interest.
The crossings of the dotted lines (signals at maximum `Vcal`, they are hardly visible behind the vertical line at t_1) with the time axis indicate the time, when at earliest signals can start to be allocated to the `WBC`. These times correspond to $\mathtt{CalDel_{LA}}$ in the measurements. If no delay caused by the comparator was considered, the green and red small dashed lines starting at these times would define θ_{int}. These signals are shifted by $CompDelay_{\mathtt{Vcal}}$ (green and red horizontal lines) to the solid green and red lines and miss therefore the bunch crossing of interest. (To not disturb, only one time axis is drawn; actually not the signals are shifted but the time stamp is set late, pointing to a later bunch crossing). Instead of the green and red, the blue and brown small dashed lines define θ_{int} — shifted by a smaller $CompDelay_{\mathtt{Vcal}}$ due to their larger `Vcal`.
Being independent of time shifts by $CompDelay_{\mathtt{Vcal}}$, θ_{abs} is determined as in figure 5.2 by signals plotted with widely dashed lines. For $\theta = 145$ `Vcal` units the signal reaches the threshold just at its maximum amplitude. This is not the case for $\theta = 45$ `Vcal` units, where the cut limits the lowest `Vcal` to 60.
The fact, that θ_{abs} and θ_{int} lie well above the set threshold is a feature of the consideration of the decaying edge (see the discussion in section 5.3).

5.3 Discussion and Conclusions

Concluding the results of the simulation, the improved toy simulation has shown:

- The negative slope of $\Delta\theta(I_{ana})$ might originate from the slower amplification (larger τ) for low I_{ana}.
- The negative slope of $\Delta\theta(\theta)$ for high thresholds and its positive slope for small thresholds and low I_{ana} might be caused by a `Vcal`-dependent delay of the comparator, originating from unwanted internal capacitors.
- The convergence of $\Delta\theta(\theta)$ to 0 for very high thresholds is clear by the way θ_{int} and θ_{abs} are determined: In the limit of the highest measurable thresholds only the signals with highest `Vcal` ever reach it. In that case, the signals that determine in-time and absolute thresholds are the same.

However, these are only *possible* explanations of the measured effects. To understand fundamentally the origin of the measured dependencies of $\Delta\theta$, one needs to know more about the shape of the calibration signal and how it is converted propagating through the preamplifier, the shaper and the comparator until the time stamp is set.

A problem not considered until now has been pointed out by this simulation: The falling edge of the signal might cut the signal before it has reached the voltage V_{cal} that is supposed to correspond to the set value of the DAC parameter `Vcal`. This leads to the difference between θ_{abs} (by definition the set `Vcal`) and θ (in the simulations the pulse height that has effectively to be reached) in figure 5.10. This difference is in the simulation obviously not negligible. However, this difference results from a simulation with assumptions and parameter settings that are not confirmed experimentally. Nevertheless this point is worth to be investigated further, as an experimental confirmation would question the role of `Vcal` as a good parameter to determine effectively reached pulse heights. The results of the measurements presented in this study are not affected by this problematics, as the threshold has been *defined* as the lowest set `Vcal` value, such that the comparator triggers. Only when simulations or calibrations are done one has to pay attention to different threshold definitions.

6 Conclusions and Outlook

Measurements of $\Delta\theta$ as a function of the threshold θ, of the analog voltage I_{ana} and of the temperature have been presented in this study for different ROCs and pixels. While previously a positive slope of $\Delta\theta(\theta)$ was expected, the experiments show a negative slope over nearly the whole measurable range of thresholds, only for some ROCs a positive slope is found for very low I_{ana} and θ. $\Delta\theta$ has been parameterized as a function of θ and I_{ana}. The large error of the expectation value of $\Delta\theta(\theta, I_{ana})$ originates from the large ROC to ROC variation. While $\Delta\theta(\theta)$ can be determined with low errors and a good reproducibility for single ROCs, the offset and the dependency on I_{ana} vary a lot among ROCs.

Possible causes of dependencies of $\Delta\theta$ have been examined in two toy simulations: Once with crude assumptions to proof, that the previous simple model can not produce a negative slope of $\Delta\theta(\theta)$. Looking for other explanations, it was found, that the comparator could play a key role concerning $\Delta\theta$. If a `Vcal`-dependent delay caused by the comparator is introduced, the main measured effects can be reproduced by the model. However, it has not been examined in this study, if the comparator is indeed the cause for the negative slope. This should be examined further: The shape of the calibration signal could be measured directly before and after the comparator, or it could be determined circuitous by deduced parameters via `psi46expert`. Both measurements are not trivial to accomplish. Another approach would be to simulate the signal over the whole readout chain in more detail.

The relevance of this study depends on the threshold applied finally for data taking in CMS. If the threshold is high (roughly over 15 000 electrons) and I_{ana} is high too (above 24 mA), $\Delta\theta$ tends to zero and there is no need to differentiate between absolute and in-time thresholds. This is not the case for low thresholds and low I_{ana}, which is the desirable range from the physics and cooling sight, respectively. The difference between absolute and in-time thresholds can be as large as a few thousands electrons and can be therefore of the same order of magnitude as the threshold itself. If measurements are done in this range, it is highly recommended to consider the difference between in-time and absolute threshold. Which threshold has to be considered depends on the concrete situation. If one is interested for instance in pixel occupancy studies, θ_{abs} should be considered, as all signals that reach θ_{abs} — no matter, when they occur and if they will be read out — are saved in the buffer in the periphery of the double column and can contribute to buffer overflow leading to temporarily blind double columns. If on the other hand one wants to reconstruct tracks, θ_{int} has to be accounted for, as signals between θ_{abs} and θ_{int} are not allocated to the correct bunch crossing.

7 Acknowledgements

I would like to thank first my supervisor Urs Langenegger, who stimulated me a lot and was able to transmit his enthusiasm for pixel detectors on me. He did a great job and supported me whenever I was stuck with simple programming questions as well as with problems of understanding. He always had time and was willing to explain, but also letting enough freedom to let me find solutions by myself.

This work would also not have been possible without the help of Andrey Starodumov and Danek Kotlinski. They introduced me in the experimental setup at PSI and provided the most important inputs for measurements.

Further more I would like to thank Wolfram Erdmann for his support with the simulation and understanding of the results, and Roland Horisberger, from whom I learned a lot about the general principles of the pixel detector.

Special thanks go to Frank Meier, who looked through carefully this report and proposed improvements.

Finally I would like to thank all the people not individually mentioned from CERN and all the pixel group at PSI, who gave me the possibility to do this work and contributed to a great working atmosphere. It was a pleasure to work with you!

A Additional Figures from the Analysis of Measurements with Single and Triple WBC

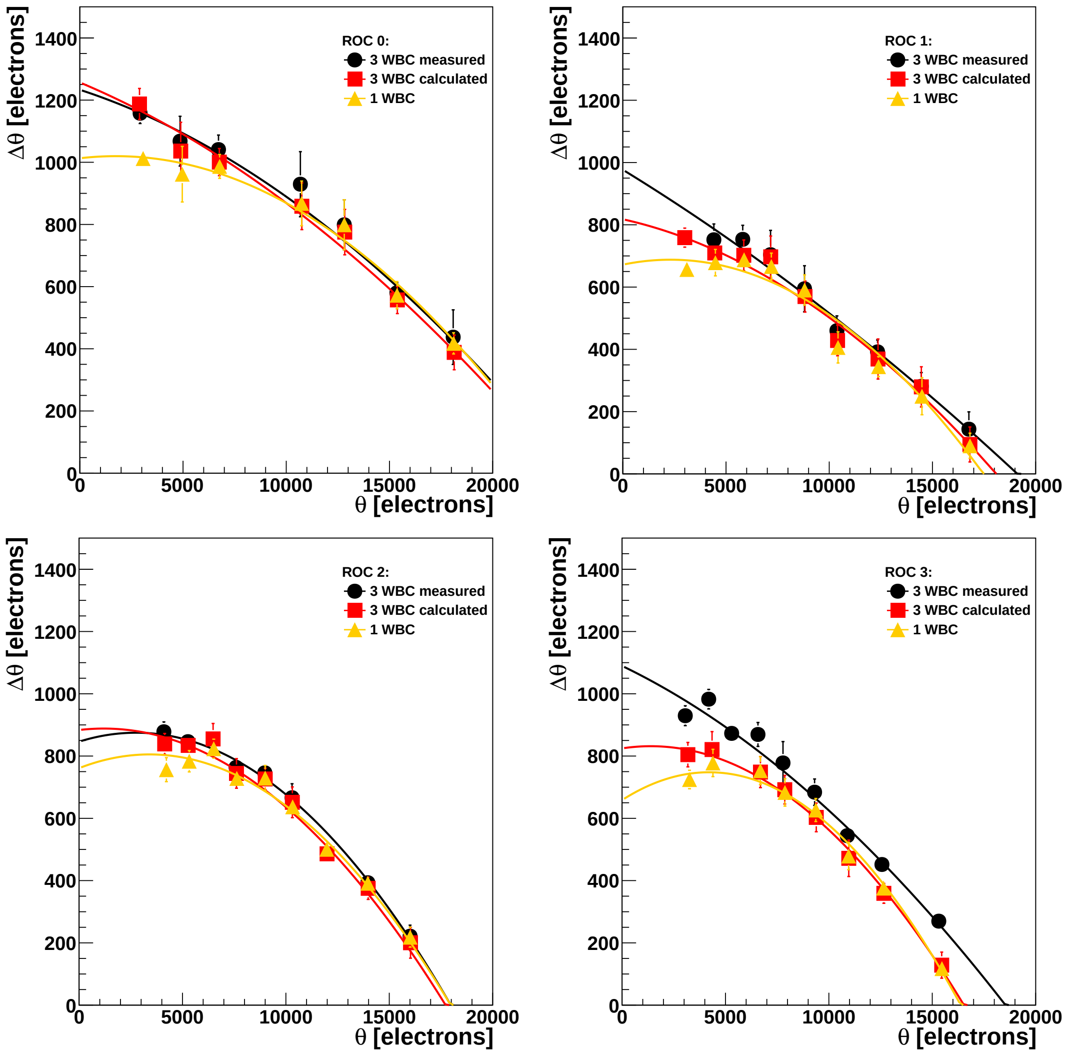

Figure A.1: $\Delta\theta^{3\mathtt{WBC}}_{\mathrm{meas}}$, $\Delta\theta^{1\mathtt{WBC}}_{\mathrm{meas}}$ and $\Delta\theta^{3\mathtt{WBC}}_{\mathrm{calc}}$ as a function of θ for the ROCs $0\ldots3$.

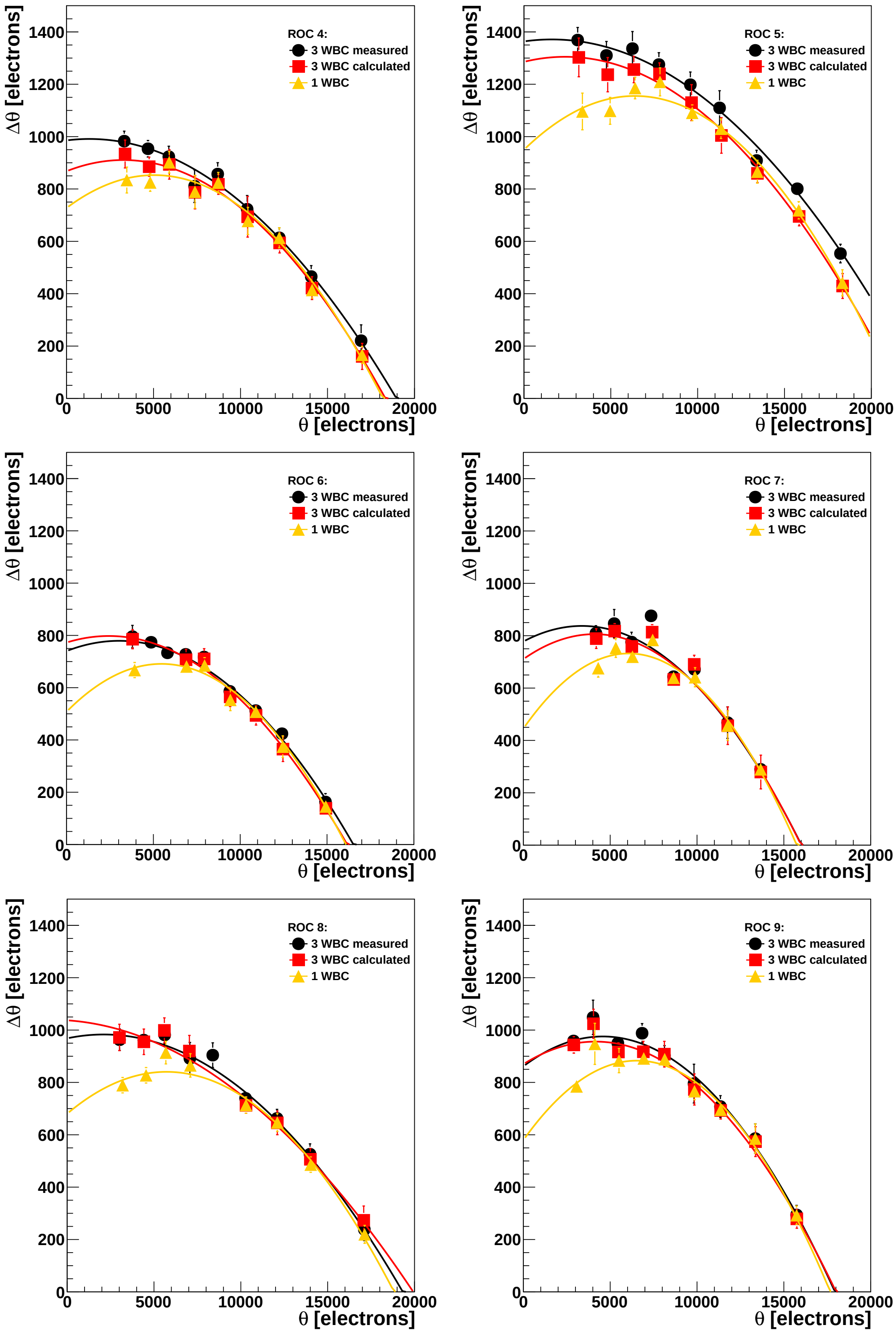

Figure A.2: $\Delta\theta^{\mathtt{3WBC}}_{\mathrm{meas}}$, $\Delta\theta^{\mathtt{1WBC}}_{\mathrm{meas}}$ and $\Delta\theta^{\mathtt{3WBC}}_{\mathrm{calc}}$ as a function of θ for the ROCs $4\ldots9$.

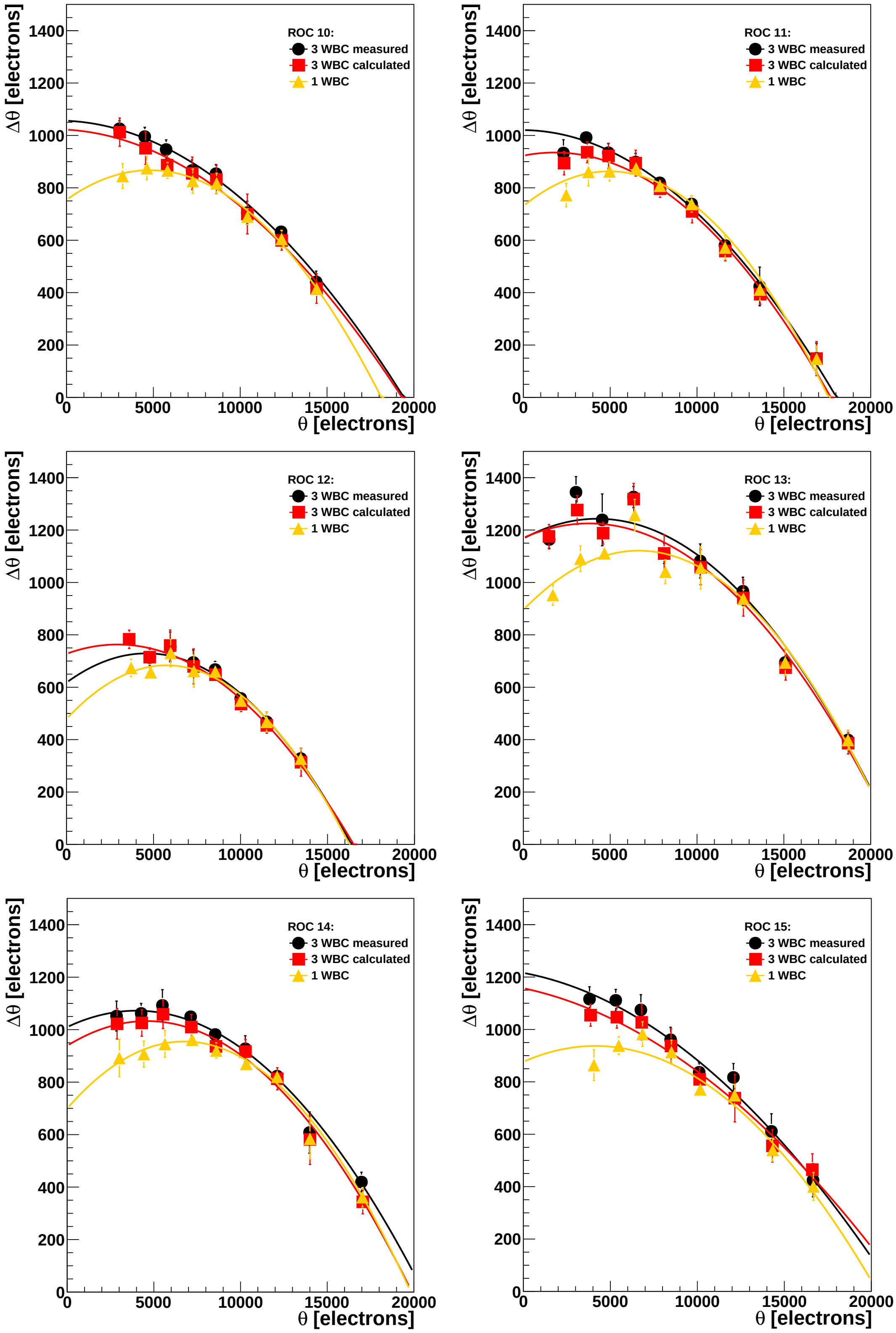

Figure A.3: $\Delta\theta^{\mathtt{3WBC}}_{\mathrm{meas}}$, $\Delta\theta^{\mathtt{1WBC}}_{\mathrm{meas}}$ and $\Delta\theta^{\mathtt{3WBC}}_{\mathrm{calc}}$ **as a function of** θ **for the ROCs** $10\ldots15$.

B Additional Figures from the Reproducibility Check

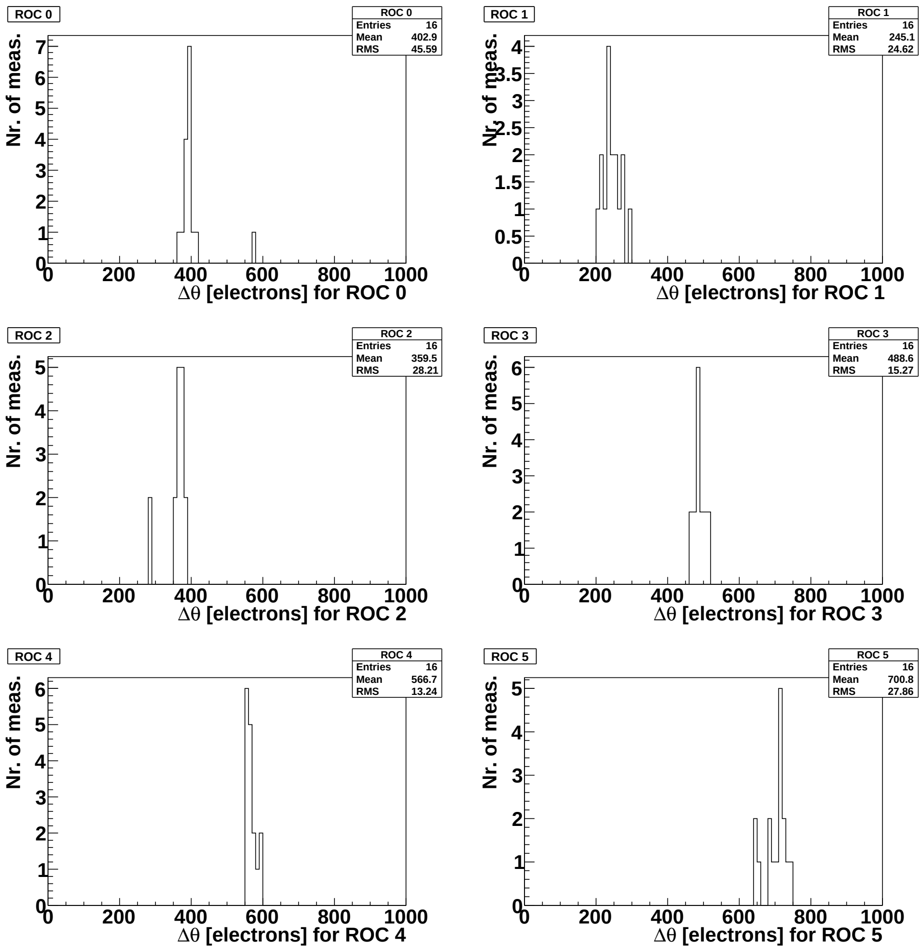

Figure B.1: Distribution of $\Delta\theta$ from 16 measurements for the ROCs $0\dots5$.

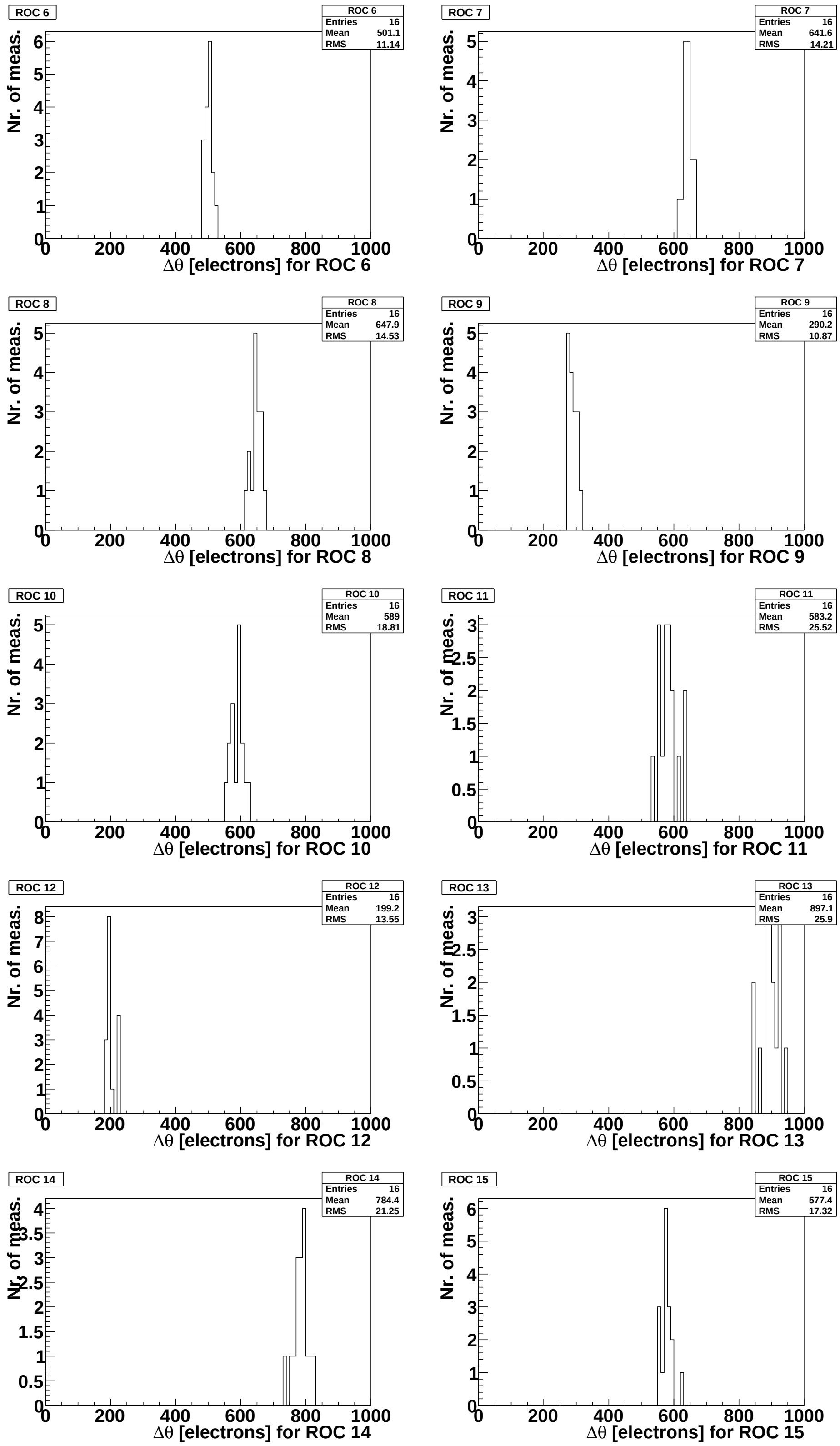

Figure B.2: Distribution of $\Delta\theta$ from 16 measurements for the ROCs $6 \dots 15$.

C Additional Figures from the Analysis of Measurements at $T = 17\,°\mathrm{C}$

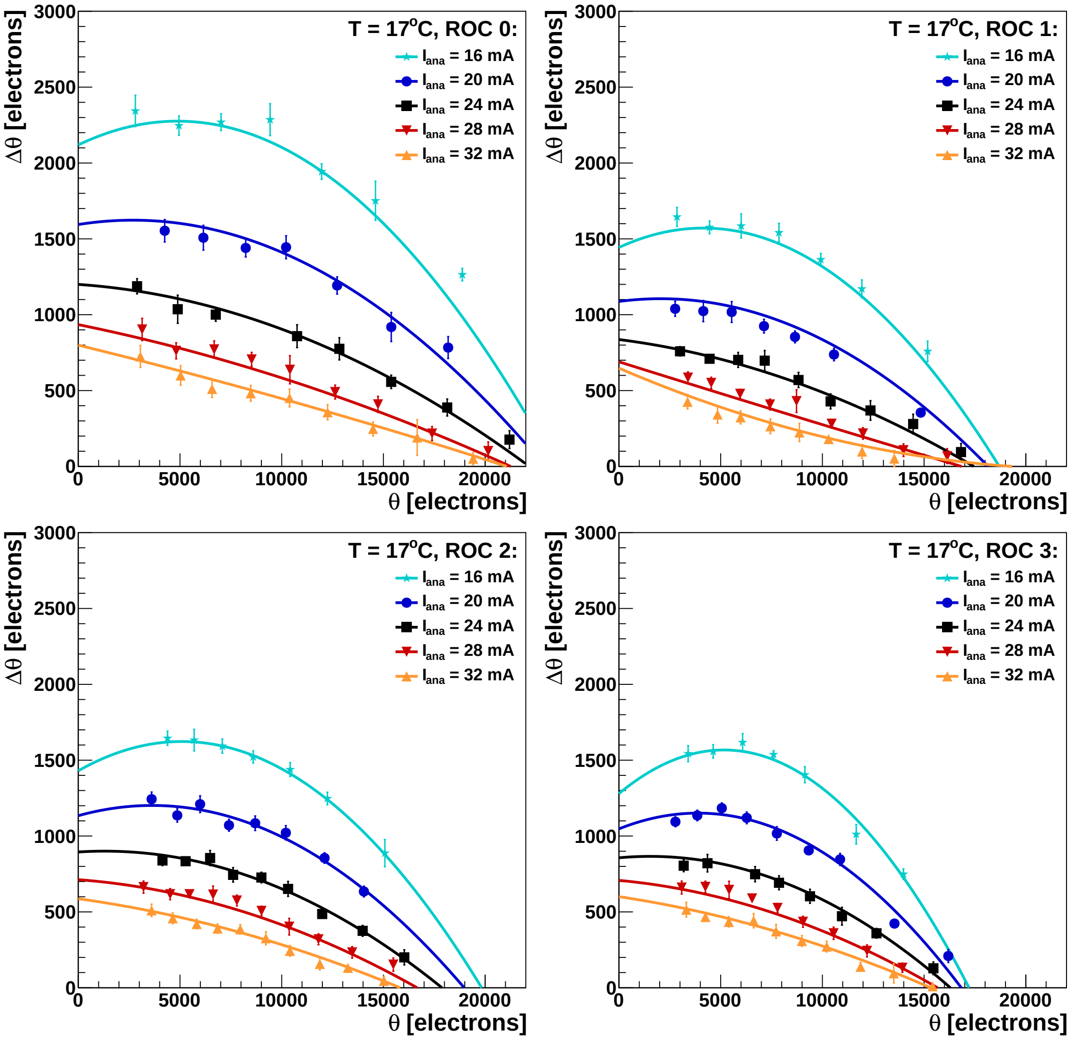

Figure C.1: $\Delta\theta$ as a function of θ and I_{ana} at $T = 17°$C for the ROCs $0 \ldots 3$. The lines are a two-dimensional polynomial fit of 2^{nd} degree.

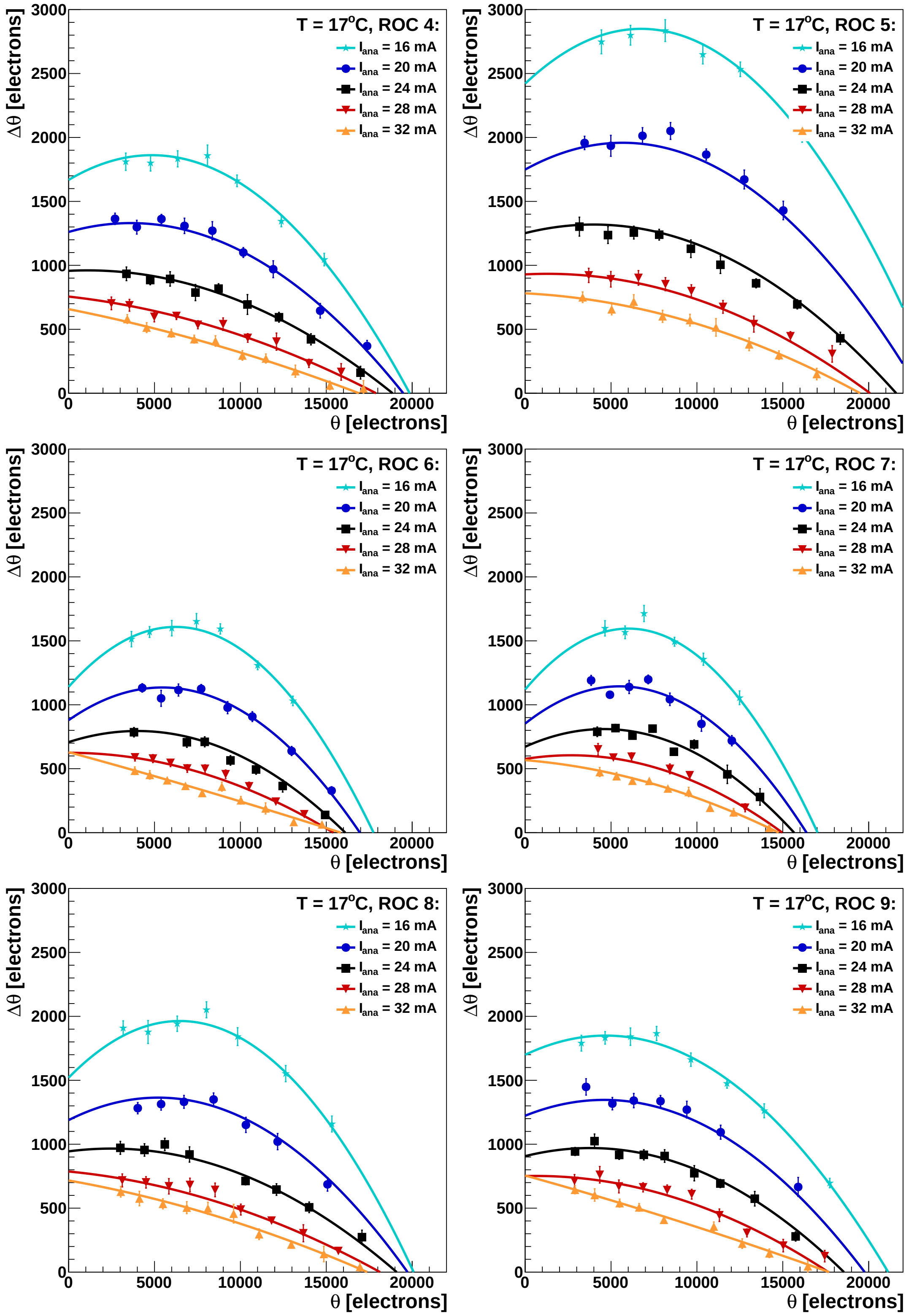

Figure C.2: $\Delta\theta$ as a function of θ and I_{ana} at $T = 17°\mathrm{C}$ for the ROCs $4 \ldots 9$. The lines are a two-dimensional polynomial fit of 2nd degree.

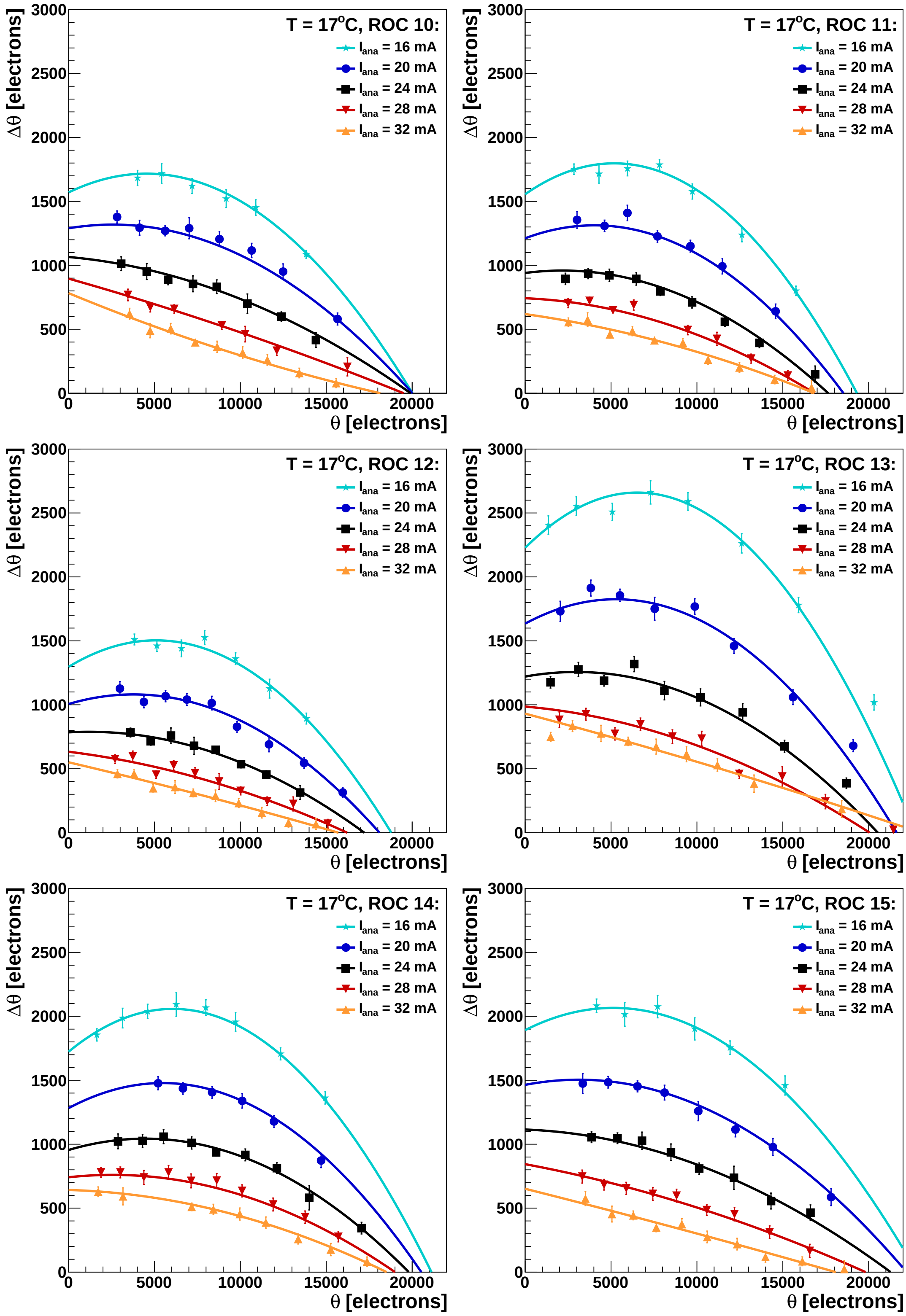

Figure C.3: $\Delta\theta$ as a function of θ and I_{ana} for the ROCs $10 \ldots 15$ at $T = 17°\mathrm{C}$. The lines are a two-dimensional polynomial fit of 2^{nd} degree.

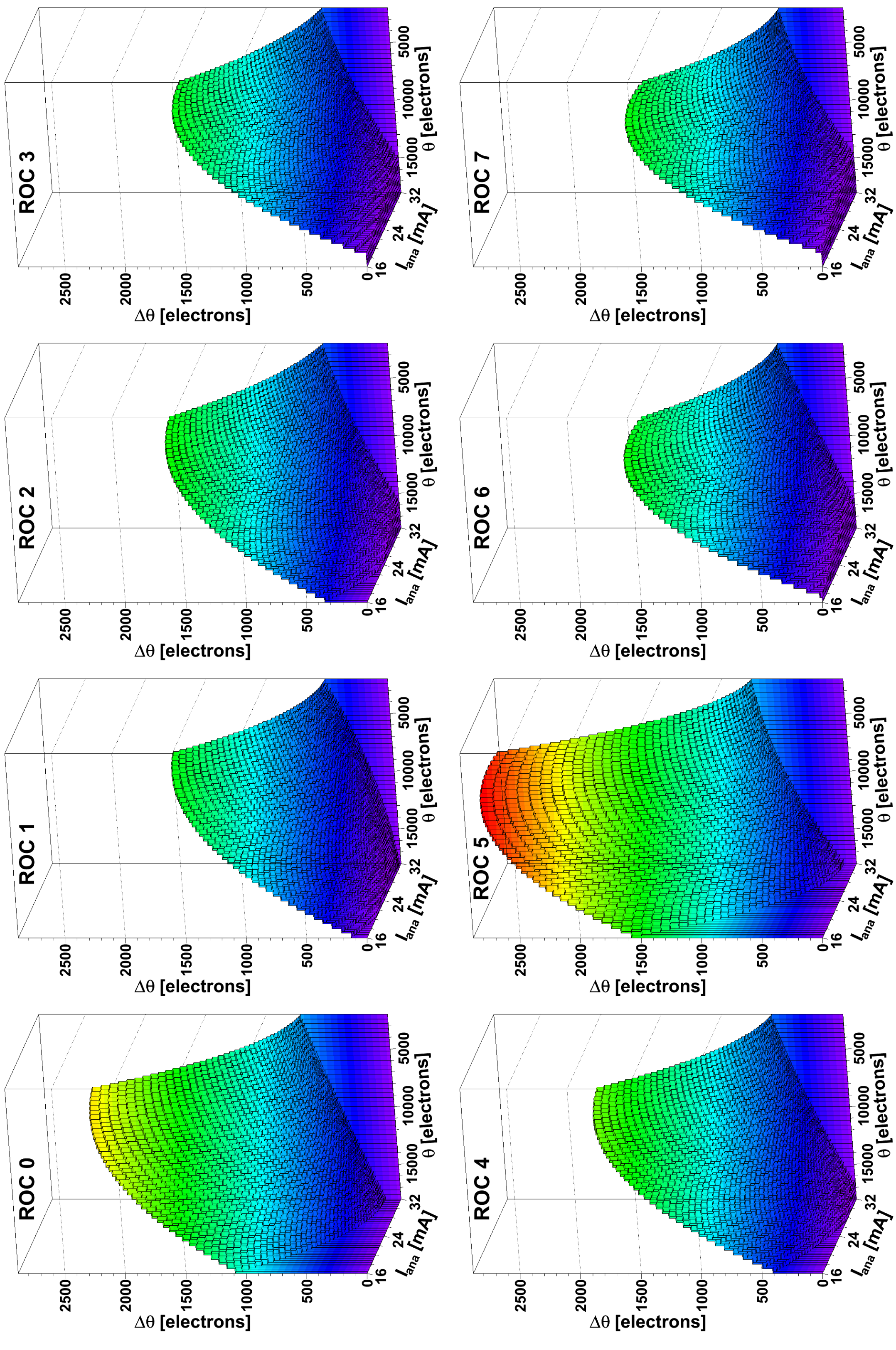

Figure C.4: Two-dimensional fit of $\Delta\theta(\theta,\, I_{ana})$ for the ROCs $0 \ldots 7$ at $T = 17°\mathrm{C}$. Equations (4.1) to (4.4) provide the two-dimensional fit function of these graphs.

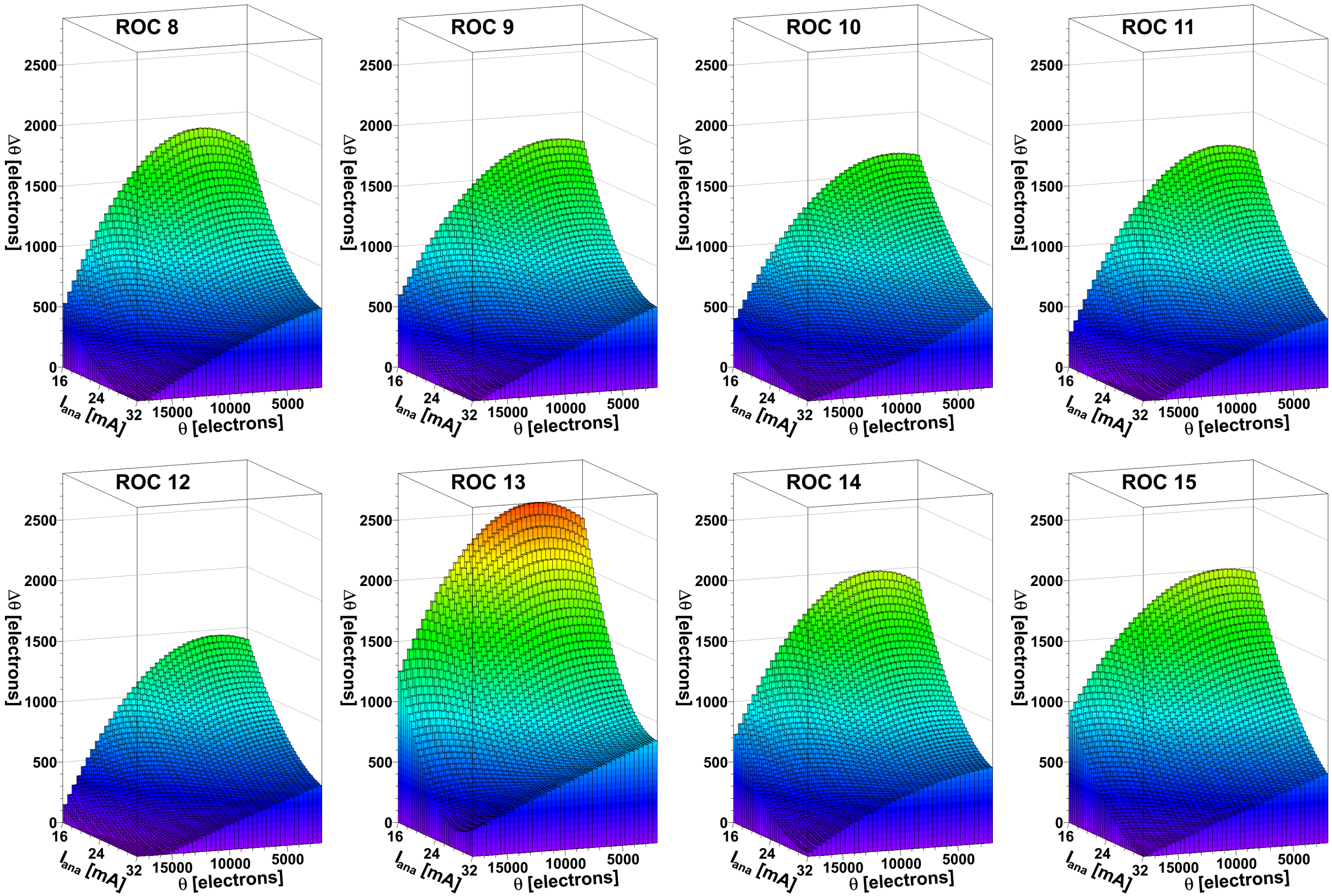

Figure C.5: Two-dimensional fit of $\Delta\theta(\theta,\, I_{ana})$ for the ROCs $8 \ldots 15$ at $T = 17°C$. Equations (4.1) to (4.4) provide the two-dimensional fit function of these graphs.

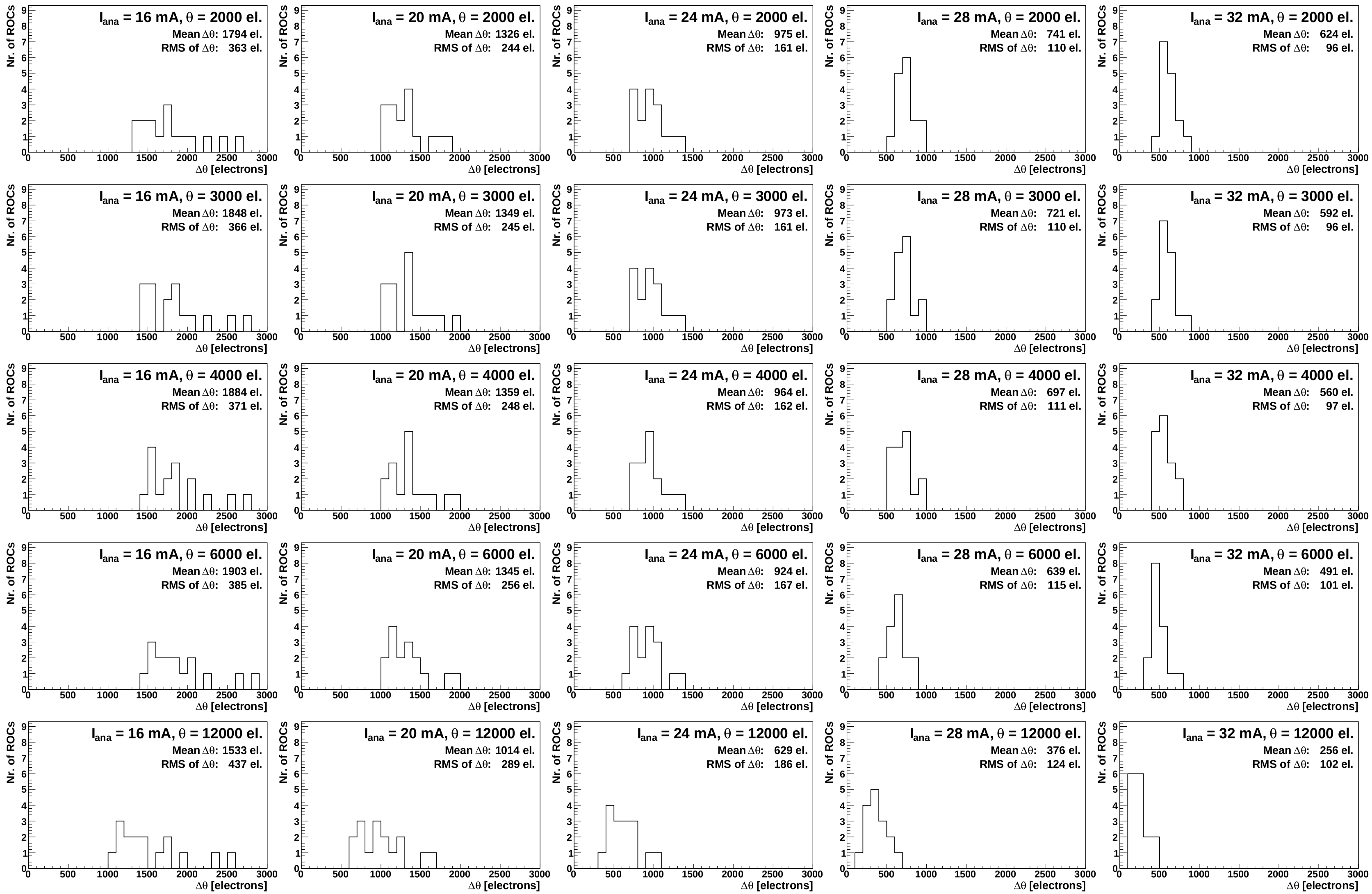

Figure C.6: Distribution of $\Delta\theta(\theta,\ I_{ana})$ among ROCs at $T = 17°\mathrm{C}$.
The fitted functions $\Delta\theta(\theta, I_{ana})$ have been evaluated ROC-wise at $\theta = 2\,000, 3\,000, 4\,000, 6\,000$ and $12\,000$ electrons and at $I_{ana} = 16, 20, 24, 28$ and 32 mA. The resulting $\Delta\theta$ has been filled into the histograms shown here.

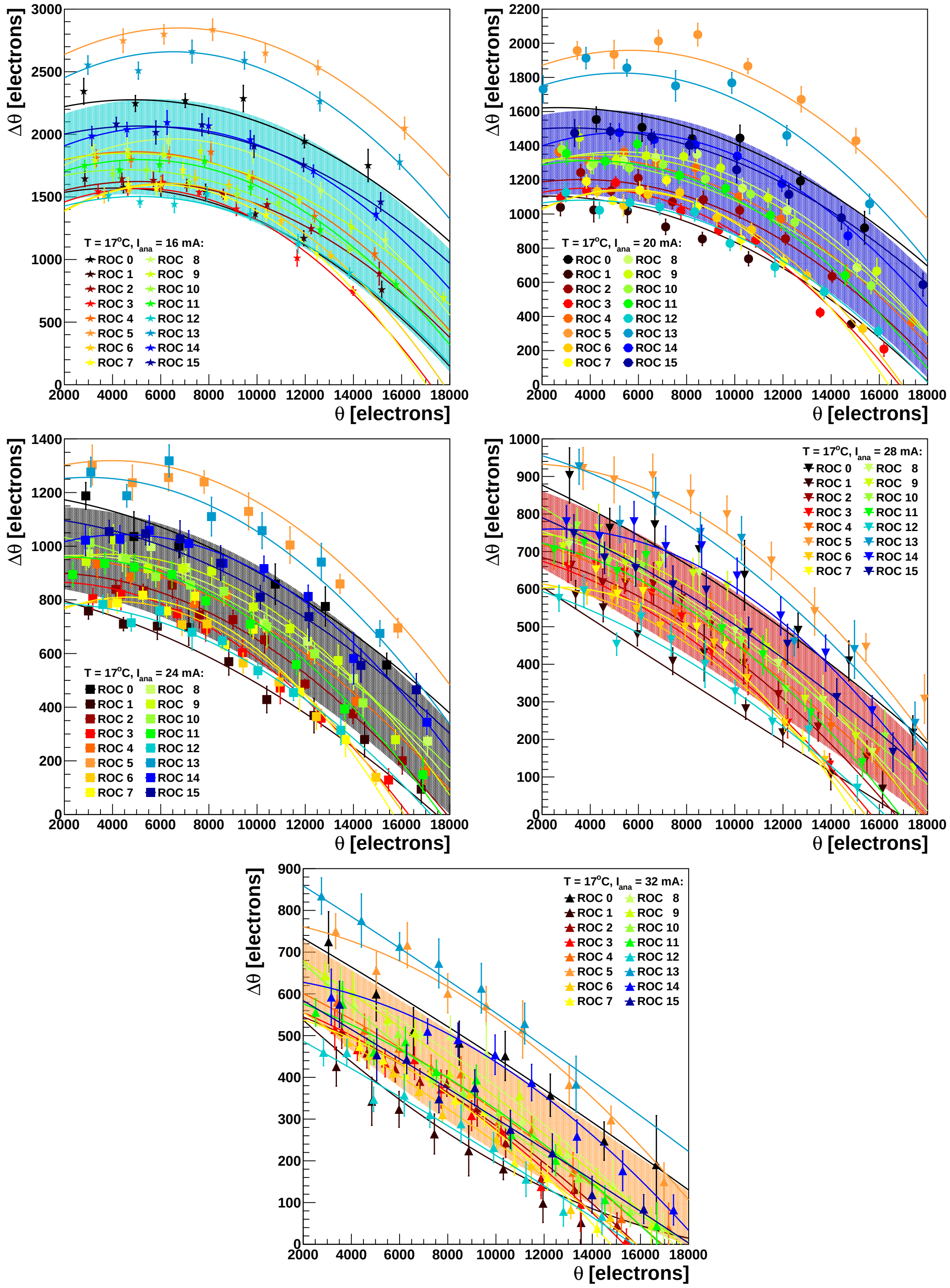

Figure C.7: $\Delta\theta(\theta)$ for $I_{ana} = 16, 20, 24, 28$ and 32 mA at $T = 17°\mathrm{C}$.
The lines are the two-dimensional polynomial fits of 2nd degree, ROC-wise applied to the measured points shown already in the figures on pages 76 to 78. The underlaying areas are the ROC to ROC distribution calculated with the parameterization of table 4.1.

D Additional Figures from the Analysis of Measurements at $T = -10\,°\mathrm{C}$

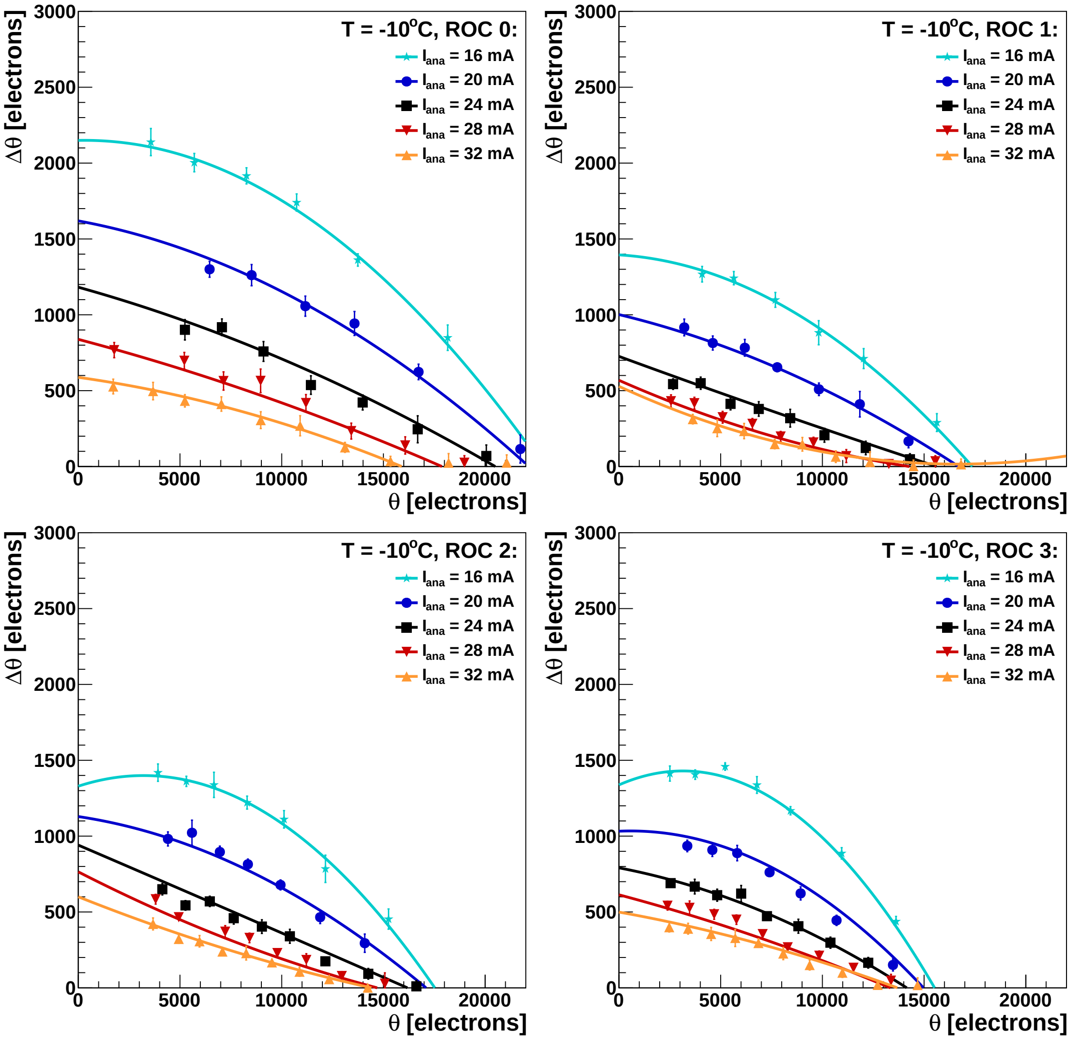

Figure D.1: $\Delta\theta$ as a function of θ and I_{ana} for the ROCs $0 \ldots 3$ at $T = -10°$C. The lines are a two-dimensional polynomial fit of 2^{nd} degree.

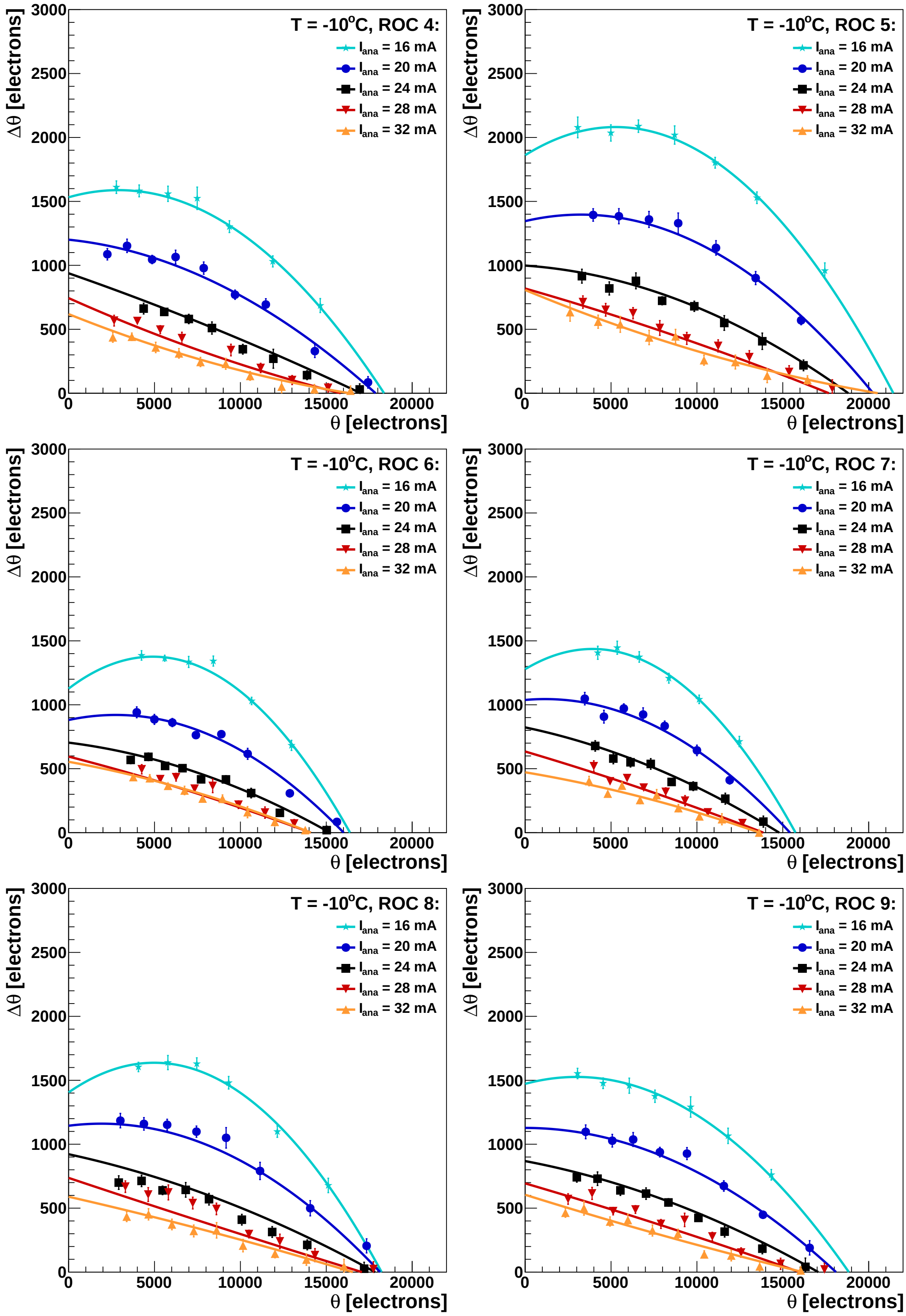

Figure D.2: $\Delta\theta$ as a function of θ and I_{ana} for the ROCs $4 \ldots 9$ at $T = -10°\mathrm{C}$. The lines are a two-dimensional polynomial fit of 2nd degree.

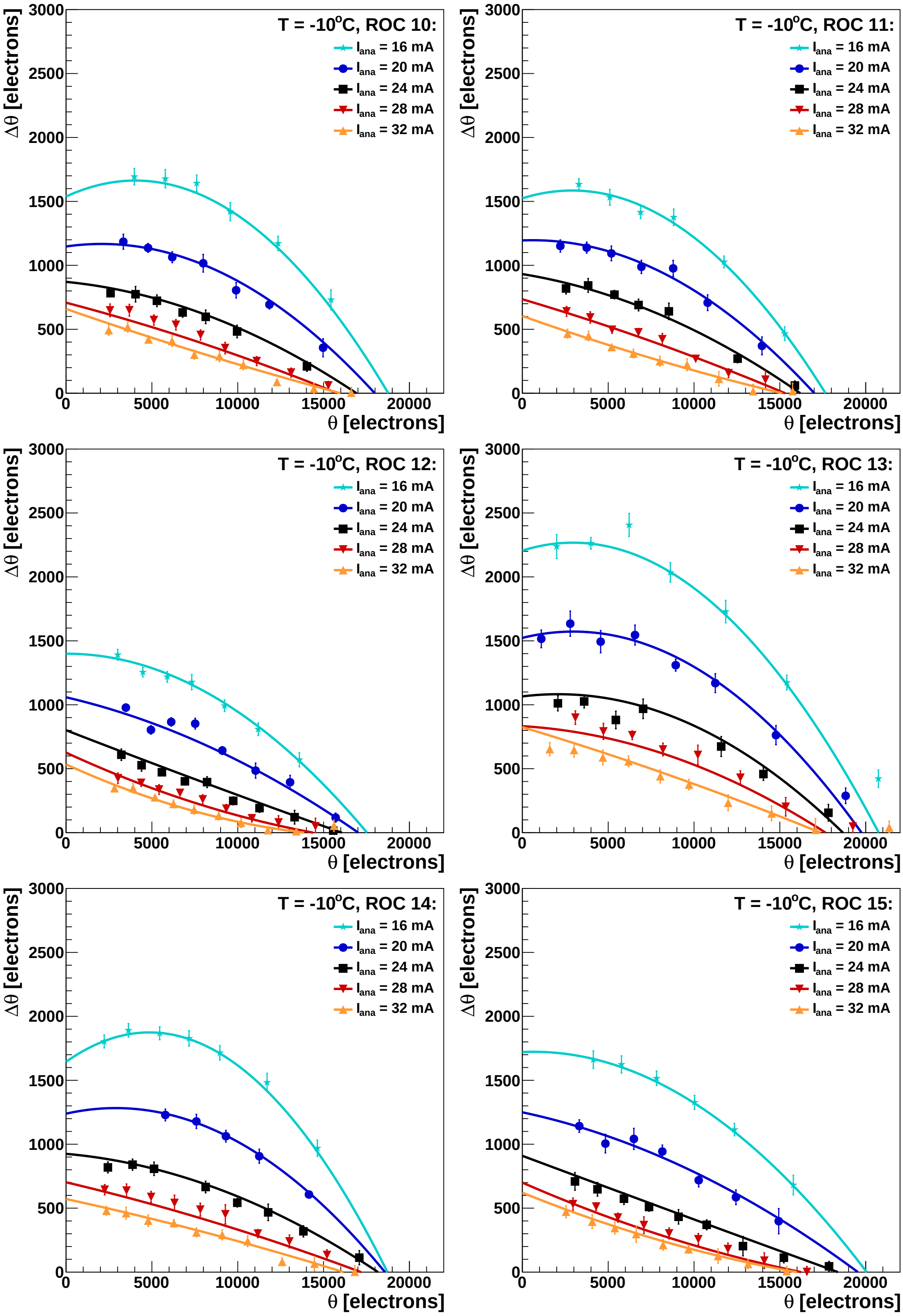

Figure D.3: $\Delta\theta$ as a function of θ and I_{ana} for the ROCs $10\ldots15$ at $T = -10°\mathrm{C}$. The lines are a two-dimensional polynomial fit of 2nd degree.

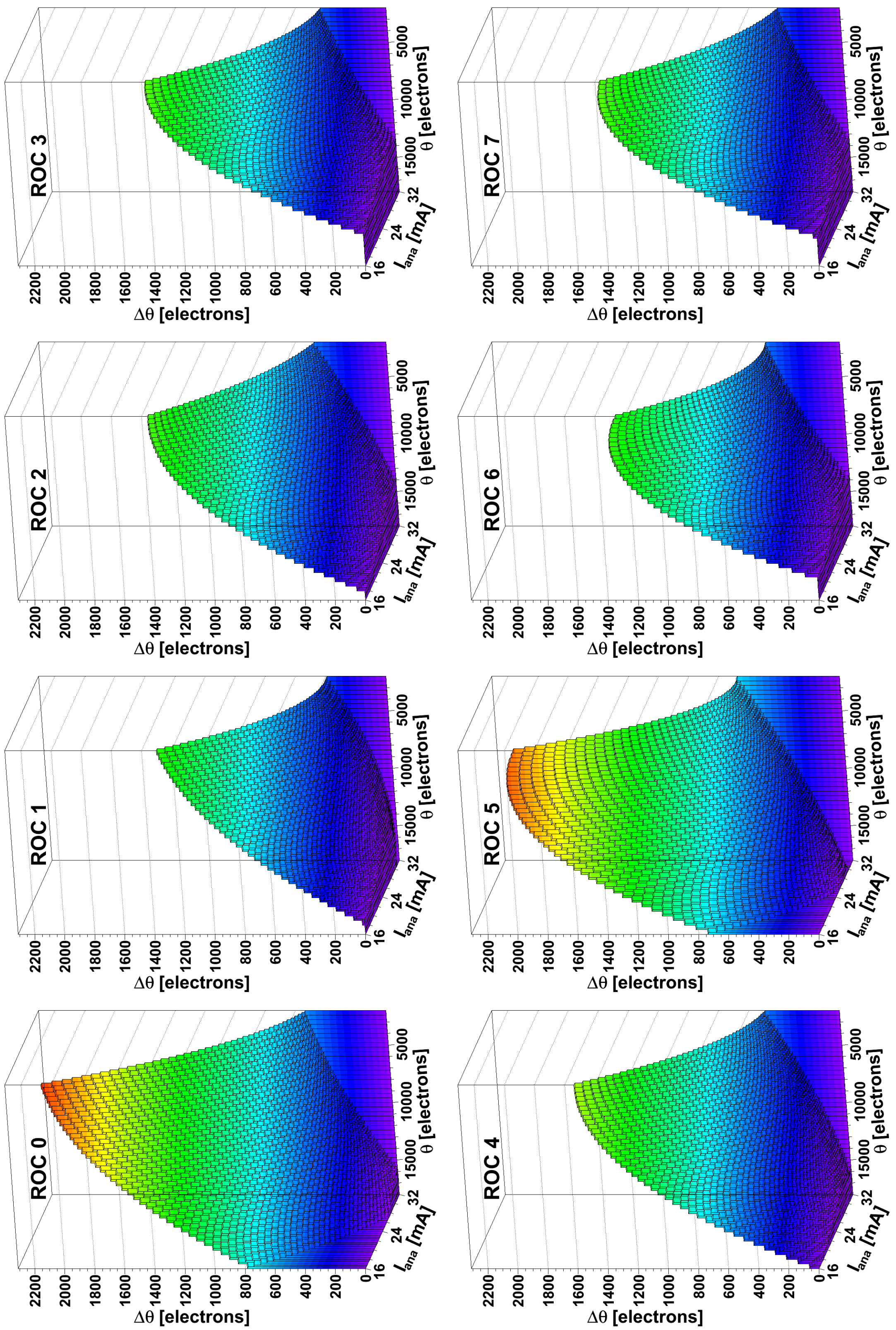

Figure D.4: Two-dimensional fit of $\Delta\theta(\theta, I_{ana})$ for the ROCs $0 \ldots 7$ at $T = -10°\mathrm{C}$. Equations (4.1) to (4.4) provide the two-dimensional fit function of these graphs.

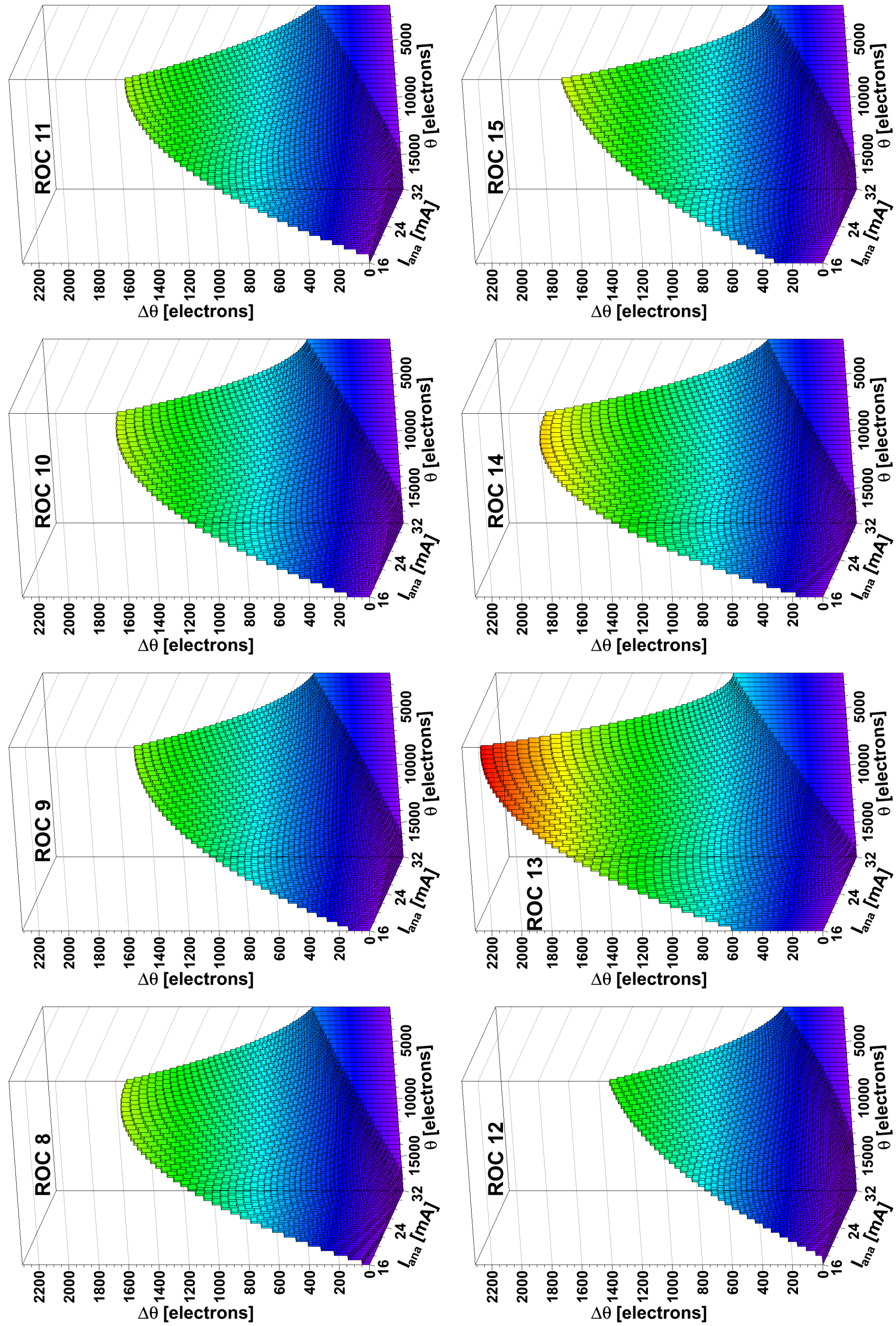

Figure D.5: Two-dimensional fit of $\Delta\theta(\theta, I_{ana})$ for the ROCs 8 . . . 15 at $T = -10°\mathrm{C}$. Equations (4.1) to (4.4) provide the two-dimensional fit function of these graphs.

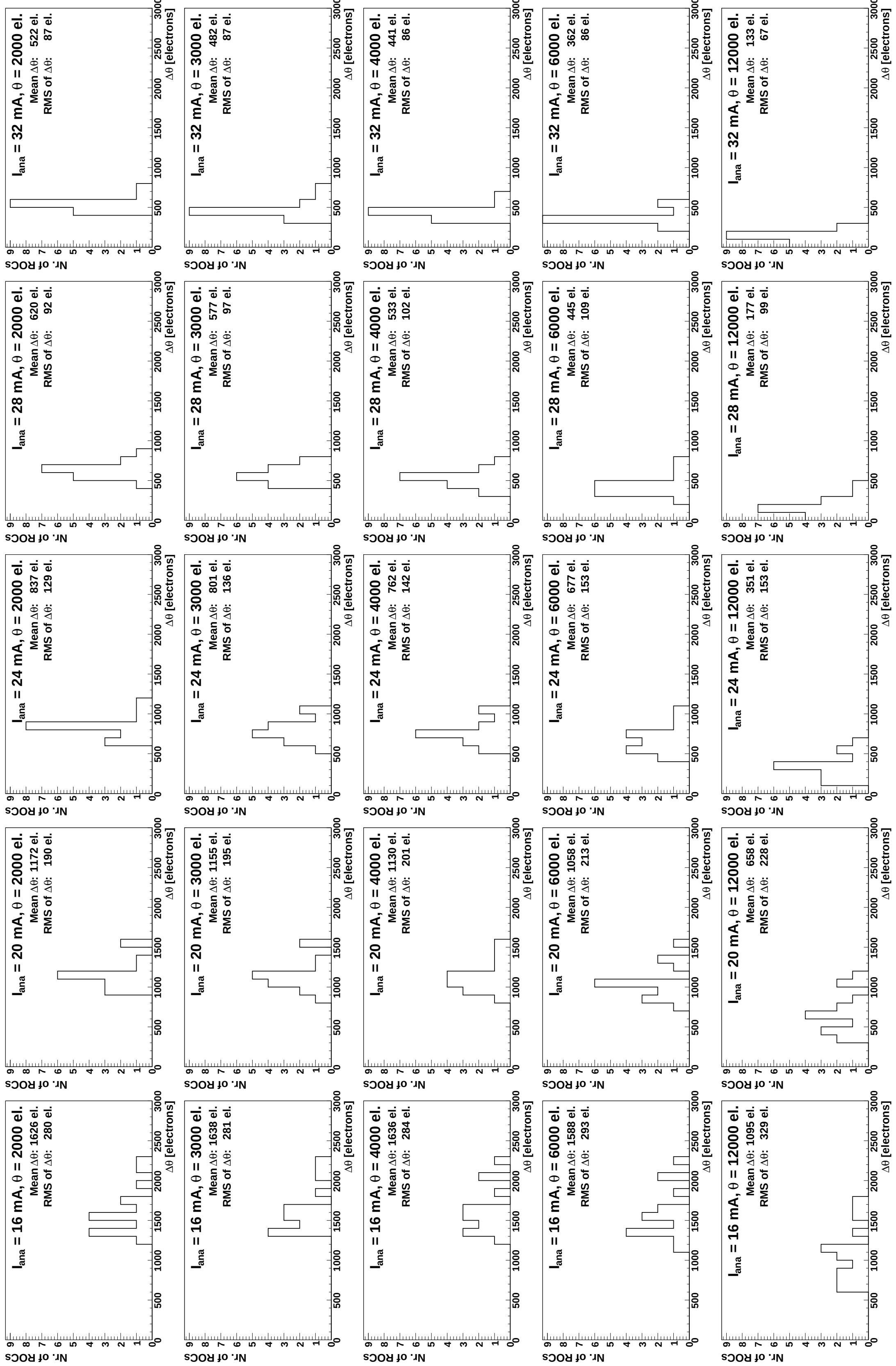

Figure D.6: Distribution of $\Delta\theta(\theta,\, I_{ana})$ among ROCs at $T = -10°\mathrm{C}$.
The fitted functions $\Delta\theta(\theta, I_{ana})$ have been evaluated ROC-wise at $\theta = 2\,000, 3\,000, 4\,000, 6\,000$ and $12\,000$ electrons and at $I_{ana} = 16, 20, 24, 28$ and 32 mA. The resulting $\Delta\theta$ has been filled into the histograms shown here.

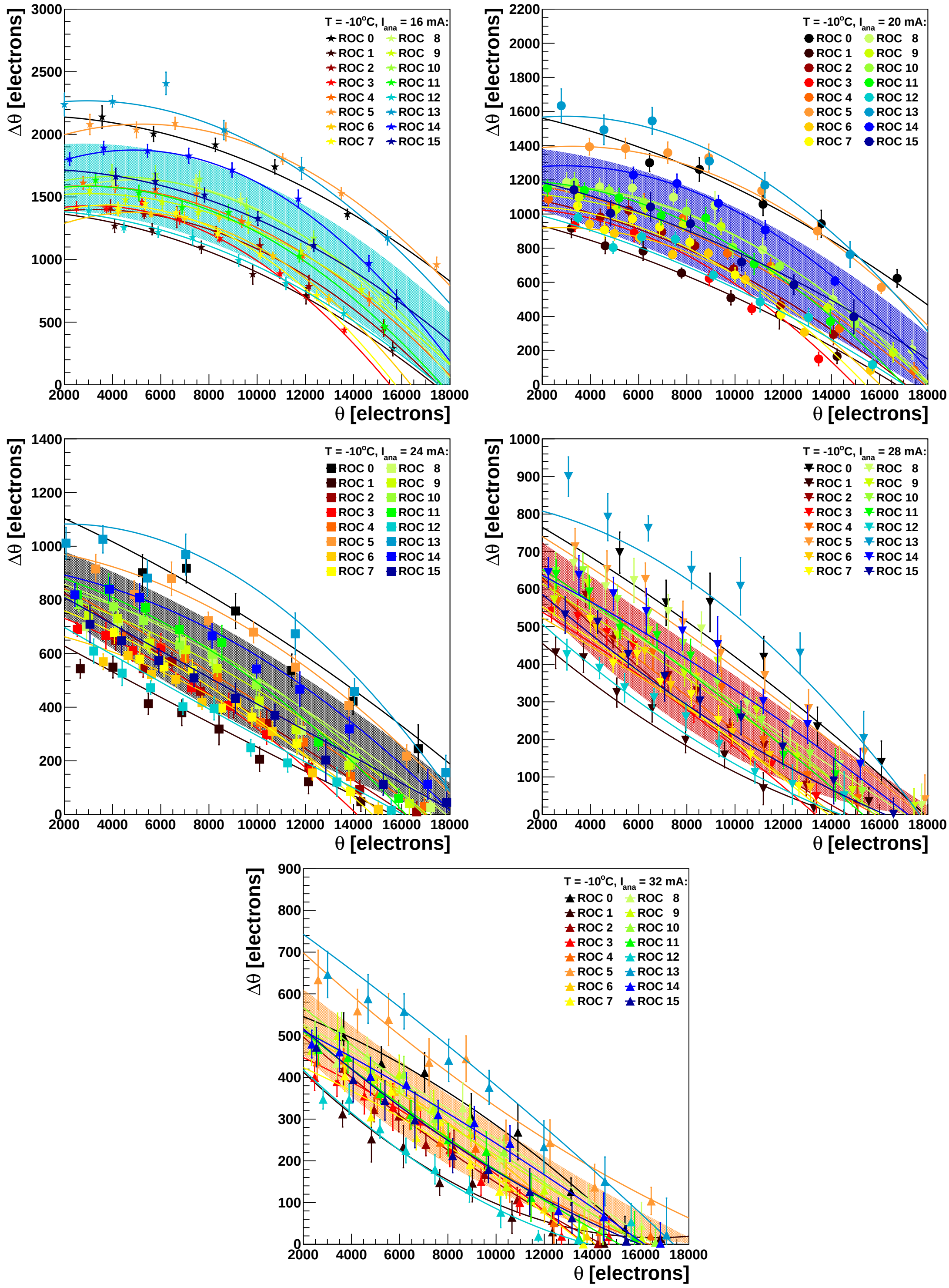

Figure D.7: $\Delta\theta(\theta)$ for $I_{ana} = 16, 20, 24, 28$ and 32 mA at $T = -10°\mathrm{C}$.
The lines are the two-dimensional polynomial fits of 2^{nd} degree, ROC-wise applied to the measured points shown already in the figures on pages 83 to 85. The underlaying areas are the ROC to ROC distribution calculated with the parameterization of table 4.2.

E Acronym List

ALICE	A Large Ion Collider Experiment 9
AOH	Analog Optical Hybrid 22
APD	Avelanche Photo Diode 14
ATLAS	A Toroidal LHC ApparatuS 8
BC	Bunch Crossing 8
BPix	Barrel Pixel detector 12
`CalDel`	DAC parameter: Calibration Delay 24
CalDelay	Calibration Delay regulated by `CalDel` 24
$\mathtt{CalDel}_{\mathtt{LA}}$	`CalDel` value of the lower amplitude of the HR scan 29
$\mathtt{CalDel}^{\mathtt{r}}_{\mathtt{LA}}$	$\mathtt{CalDel}_{\mathtt{LA}}$ rounded to an integer 32
$\mathtt{CalDel}_{\mathtt{LL}}$	`CalDel` value of the lower limit of the LR scan 34
$\mathtt{CalDel}_{\mathtt{UA}}$	`CalDel` value of the upper amplitude of the HR scan 30
$\mathtt{CalDel}_{\mathtt{UL}}$	`CalDel` value of the upper limit of the LR scan 34
CASTOR	Centauro And Strange Object Research 17
CERN	Conseil Européenne pour la Rechèrche Nucleaire 8
χ^2	Mean error square of a fit 35
CMS	Compact Muon Solenoid 8
CompDelay	Delay of the calibration signal caused by the comparator 61
$CompDelay_{\theta}$	Threshold dependent part of *CompDelay* 61
$CompDelay_{\mathtt{Vcal}}$	`Vcal` dependent part of *CompDelay* 62
CSC	Cathode Strip Chamber 17
`CtrlReg`	`Vcal` range regulator 23
DAC	Digital Analog Converter 18
DAQ	Data AcQuisition system 22
$\Delta\mathtt{CalDel}_{\mathtt{LR}}$	$\mathtt{CalDel}_{\mathtt{UA}} - \mathtt{CalDel}_{\mathtt{LA}}$ 34
$\Delta\mathtt{CalDel}_{\mathtt{HR}}$	$\mathtt{CalDel}_{\mathtt{UL}} - \mathtt{CalDel}_{\mathtt{LL}}$ 34
DCOL	Double COLumn 19
$\Delta\theta$	$\theta_{int} - \theta_{abs}$ 25
DOH	Digital Optical Hybrid 22
Dee	Half endcap of ECAL 8
DT	Drift Tube 16
E	Number of electrons measured in X-ray calibration 39
ECAL	Electromagnetic CALorimeter 13
FEC	Front End Controller 22
FED	Front End Driver 22
FPix	Forward Pixel detector 12
GUI	Graphic User Interface 27
HB	Hadron calorimeter Barrel 15

HCAL	Hadron CALorimeter	15
HDI	High Density Interconnect	19
HE	Hadron calorimeter Endcap	15
HF	Forward Hadron calorimeter	15
HO	Outer Hadron calorimeter	15
HPD	Hybrid Photo Diode	15
HR	`Vcal` High Range (corresponds to $V_{cal} = 0 \ldots 1800\,\mathrm{mV}$)	23
I_{ana}	Analog current	23
λ_I	Interaction length	15
L1	1$^{\mathrm{st}}$ Level trigger	22
LEP	Large Electron Positron collider	8
LHC	Large Hadron Collider	8
LHCb	Large Hadron Collider beauty	9
LINAC	LINear ACcelerator	8
LR	`Vcal` Low Range (corresponds to $V_{cal} = 0 \ldots 280\,\mathrm{mV}$)	23
m	Slope of the linear function for the calibration `Vcal` $\leftrightarrow$ electrons	39
MB	Muon Barrel detector	15
ME	Muon Endcap detector	15
NDF	Number of Degrees of Freedom	35
PMT	Photo Multiplier Tube	17
PS	Proton Synchrotron	8
p_T	Transverse momentum	16
PSI	Paul Scherrer Institute	27
psi46v2.1	Read out chip for the pixel detector	19
`psi46expert`	Data taking code used for the measurements of this work	27
q	Offset of the linear function for the calibration `Vcal` $\leftrightarrow$ electrons	39
RMS	Root Mean Square	32
PUC	Pixel Unit Cell	19
ROC	Read Out Chip	19
`root`	Analysis framework based on `C++`	27
RPC	Resistive Plate Chamber	16
SCurve	Fit algorithm to determine the value of 50 % readout probability	31
SL	Super Layer	16
SPS	Super Proton Synchrotron	8
θ	Threshold	23
θ_{abs}	Absolute threshold	25
$\theta_{\mathtt{CalDel}}$	Threshold determined from `Vcal` values at distinct `CalDel`	32
θ_{int}	In-time threshold	25
τ	Simulation parameter: time constant of amplifiers	56
τ_c	Simulation parameter: time constant of the comparator	63
τ_f	Simulation parameter: time constant of the falling edge	63
t_0	Simulation parameter: time between the start of the signal and its arrival at the comparator	56
t_f	Simulation parameter: time between the rising and falling of the calibration signal	63
TBM	Token Bit Manager	19

F root-Tree with the Main Results

The measured data and their analysis by `threshold.C` provide more information than what has been presented in this study. Therefore, the most important data have been stored in two `root` files: `thresholdrawdata.root` contains the raw data and `threshold.root` the parameters set and the results of the analysis. They are presented in more detail in the following two sections.

F.1 Content of `thresholdrawdata.root`

The HR and LR scans (readout probability as a function of `CalDel` and `Vcal`) are stored as TH2F histograms with specific measurement numbers visible in the name and title together with the indication HR/LR. The histograms of measurement 1293 are shown in figures F.1 as examples.

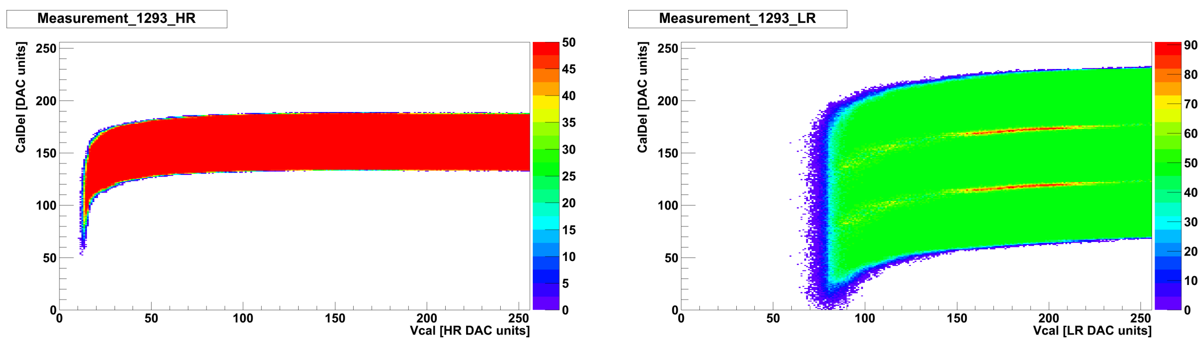

(a) (b)

Figure F.1: HR (a) and LR (b) histograms of the measurement 1293.

Although they are based on the same raw data, measurements of a single `WBC` and of 3 numerically shifted `WBC`s are stored as two different measurements. Measurement 1292 is for instance the single `WBC` case of measurement 1293. Only measurements that satisfy the criteria described in section 3.3 are stored. Therefore, not for all single (triple) `WBC` measurement is stored the corresponding triple (single) `WBC` measurement, as one of them might not satisfy the quality criteria. The stored triple `WBC` measurements are those presented in the sections 3.7, 3.8, 4.1, 4.2 and 4.3.

F.2 Content of `threshold.root`

The file `threshold.root` contains the `root`-tree 'thresholdmeasurements' with the results of the analysis for each measurement, for which the raw data are stored in `thresholdrawdata.root`. The parameters set and the results of a measurement are organized in leaves of the tree. They are shortly described in table F.1.

Table F.1: Leaves of the `root`-tree "thresholdmeasurements" of the file `threshold.root`
Format 'D': double, 'I': integer. Leaves in *italic* are only internally used by `threshold.C`.

Leave/Format	Range	Description
CalDelDiff_HR_CalDelDAC/D	$[40, 70]$	ΔCalDel$_{\texttt{HR}}$ in `CalDel` DAC units
CalDelDiff_LR_CalDelDAC/D	$[40, 70]$	ΔCalDel$_{\texttt{LR}}$ in `CalDel` DAC units
Column/I	$[0, 51]$	Column of the pixel within a ROC
***Fileloopnr*/I**	$[3, 213]$	Loop counter of *RawdatafileHR* and *RawdatafileLR*
Iana_mA/I	$[16, 32]$	Analog current I_{ana} in milli Ampère
Measurementnr/I	$[0, 10\,590]$	Measurement specific number for the identification of the corresponding raw data in the file `thresholdrawdata.root`
***RawdatafileHR*/I**	$[73, 477]$	Number of the original HR data file
***RawdatafileLR*/I**	$[72, 476]$	Number of the original LR data file
ROC/I	$[0, 16]$	ROC number of module M0090
Row/I	$[0, 79]$	Row of the pixel within a ROC
Settingfilenr/I	$[72, 453]$	The folder 'settings_m<Settingfilenr>' contains amongst others the files with DAC parameter settings not written to a leave of this tree
SingleTripleWBC/I	$\{0, 1\}$	0: θ_{abs} from single `WBC` measurement 1: θ_{abs} from triple `WBC` measurement (numerically shifted)
Temperature/I	$\{-10, 17\}$	Temperature in the cooling box in °C
ThrAbs_electrons/D	$\mathbb{R}^+$	θ_{abs} in electrons
ThrAbs_VcalDAC/D	$[0, 256)$	θ_{abs} in `Vcal` LR DAC units
ThrAbserr_electrons/D	$\mathbb{R}^+$	Error of θ_{abs} in electrons
ThrAbserr_VcalDAC/D	$[0, 256)$	Error of θ_{abs} in `Vcal` LR DAC units
ThrDiff_electrons/D	$\mathbb{R}^+$	$\Delta\theta$ in electrons
ThrDiff_VcalDAC/D	$[0, 256)$	$\Delta\theta$ in `Vcal` LR DAC units
ThrDifferr_electrons/D	$\mathbb{R}^+$	Error of $\Delta\theta$ in electrons
ThrDifferr_VcalDAC/D	$[0, 256)$	Error of $\Delta\theta$ in `Vcal` LR DAC units
ThrInt_electrons/D	$\mathbb{R}^+$	θ_{int} in electrons
ThrInt_VcalDAC/D	$[0, 256)$	θ_{int} in `Vcal` LR DAC units
ThrInterr_electrons/D	$\mathbb{R}^+$	Error of θ_{int} in electrons.
ThrInterr_VcalDAC/D	$[0, 256)$	Error of θ_{int} in `Vcal` LR DAC units
TimePerDAC_HRnsperDAC/D	$(0.35, 0.63)$	Time in nano seconds corresponding to 1 `CalDel` DAC unit from the HR scan
TimePerDAC_LRnsperDAC/D	$(0.35, 0.63)$	Time in nano seconds corresponding to 1 `CalDel` DAC unit from the HR scan
Vcthr_electrons/D	$\mathbb{R}^+$	`Vcthr` in electrons
Vcthr_VcalDAC/D	$[0, 255)$	`Vcthr` in `Vcal` LR DAC units
Vcthr_VcthrDAC/I	$[0, 255]$	`Vcthr` in `Vcthr` DAC units
Vcthrerr_electrons/D	$\mathbb{R}^+$	Error of `Vcthr` in electrons
Vcthrerr_VcalDAC/D	$[0, 255)$	Error of `Vcthr` in `Vcal` LR DAC units
WBC/I	$[99, 100]$	WBC value of the measurement

Bibliography

[1] L. Evans *et al.*, LHC Machine, JINST **3** (2008) S08001.

[2] http://mediaarchive.cern.ch/MediaArchive, 2008-12-22 10.15.

[3] S.Chatrchyan *et al.*, The CMS Collaboration, The CMS Experiment at the CERN LHC, JINST **3** (2008) S08004.

[4] G. Aad *et al.*, The ATLAS Collaboration, The ATLAS Experiment at the CERN Large Hadron Collider, JINST **3** (2008) S08003.

[5] A. Augusto Alves Jr. *et al.*, The LHCb Collaboration, The LHCb Detector at LHC, JINST **3** (2008) S08005.

[6] K. Aamodt *et al.*, The ALICE Collaboration, The ALICE Experiment at the CERN LHC, JINST **3** (2008) S08002.

[7] G. Anelli *et al.*, The TOTEM Collaboration, The TOTEM Experiment at the CERN Large Hadron Collider, JINST **3** (2008) S08007.

[8] `https://cms-project-cmsinfo.web.cern.ch/cms-project-cmsinfo`, 2008-12-22 13.33.

[9] Y. Allkofer *et al.*, Design and performance of the silicon sensors for the CMS barrel pixel detector, NIM **584** (2008) 25.

[10] K. Gabathuler, PSI46 Pixel Chip - External Specification, PSI (2005).

[11] `http://cms.web.psi.ch/figures_and_presentations`, 2009-02-08 17.42.

[12] `http://www.ba.infn.it/~zito`, 2008-02-08 17.39.

[13] S. Dambach *et al.*, Qualification of the CMS Barrel Pixel Detector Modules, JINS (Preprint).

[14] D. Kotlinski *et al.*, The Control and Readout Systems of the CMS Pixel Barrel Detector, NIM A **565** (2006) 73.

[15] P. Trüb, CMS Pixel Module Qualification and Monte-Carlo Study of $H \to \tau^+\tau^- \to l^+l^-\not{E}_T$, Dissertation No.17985 at ETH Zurich (2008).

[16] M. Waser, Online Trimming of the CMS Pixel-Detector and Testing of the -X-Side of the Pixel-Detector, Diploma Work at ETH Zurich (2008).

[17] ROOT: An Object Oriented Data Analysis Framework, `http://root.cern.ch`.

[18] W. Erdmann, Private communication.